AG-CU BIMETALLIC NANOPARTICLE SYNTHESIS AND PROPERTIES

by

Ziye Xiong

B.S. in Polymer Science, Hubei University of Technology, 2011

M.S. in Materials Science and Engineering, University of Pittsburgh, 2013

Submitted to the Graduate Faculty of

the Swanson School of Engineering in partial fulfillment

of the requirements for the degree of

Doctor of Philosophy

University of Pittsburgh

2017

UNIVERSITY OF PITTSBURGH

SWANSON SCHOOL OF ENGINEERING

This dissertation was presented

by

Ziye Xiong

It was defended on

May 16th 2017

and approved by

Ian Nettleship, Ph.D., Associate Professor,

Department of Mechanical Engineering and Materials Science

Jung-Kun Lee, Ph.D., Associate Professor,

Department of Mechanical Engineering and Materials Science

Guofeng Wang, Ph.D., Assistant Professor,

Department of Mechanical Engineering and Materials

Paul Leu, Ph.D., Assistant Professor,

Department of Industrial Engineering

Dissertation Director: Ian Nettleship, Ph.D., Associate Professor,

Department of Mechanical Engineering and Materials Science

AG-CU BIMETALLIC NANOPARTICLE SYNTHESIS AND PROPERTIES

Ziye Xiong, PhD

University of Pittsburgh, 2017

Silver(Ag)-Copper(Cu) bimetallic nanoparticles (NPs) were synthesized by chemical reduction with the assistance of a microwave reactor. Considering the difference in redox potential of Ag(I) and Cu(II), the effect of heating method was compared using 'one-pot' and 'two-pot' synthesis of Ag-Cu shell-core and Ag-Cu core-shell nanoparticles. One-pot synthesis naturally results in Ag-Cu core-shell nanoparticles since silver has the higher redox potential than copper. In the two-pot synthesis of Ag-Cu core-shell nanoparticles, the effect of the heating conditions was compared. At the highest reaction temperature (175 °C), the galvanic reaction by which silver reduction occurred through the oxidation copper metal, was suppressed and higher Cu/Ag phase ratios could be achieved.

Nanoparticles properties were examined in the following areas: (i) nanoparticle solubility and antibacterial effects, (ii) sintering behavior and electrical conductivity of nanoparticle films. Enhanced antibacterial effects were observed for mixtures of Ag and Cu nanoparticles against planktonic *M.smegmatis* silver resistant mutants as well as the wild type when compared to the antibacterial effects of pure Ag or Cu NPs alone. However, solubility tests in deionized water, showed that very low Ag ion concentrations resulted when copper was present either in bimetallic nanoparticles or in mixtures of Ag and Cu NPs. This was attributed to a galvanic effect that suppressed the oxidation of silver.

The deposition of nanoparticles on surfaces was studied in terms of the ability of the deposited nanoparticles to inhibit the growth the biofilm. Printed silver nanoparticle dots deposited on microfilters exhibited significant antibacterial effect in inhibiting the growth of biofilm over the whole micro filter surface. Increasing the areal coverage of the dots or their

size decreased the number and the size of bacterial colonies. Finally, the sintering behavior of Ag-Cu shell core nanoparticles proved superior to that of Cu nanoparticles and to mixture of silver and copper nanoparticles. This resulted in higher electrical conductivity in the nanoparticle films sintered at lower temperature. This is thought to be due to the higher fraction of Ag-Ag particle contacts.

TABLE OF CONTENTS

LIST OF TABLES

LIST OF FIGURES

1.0 INTRODUCTION

In this study, nanoparticles of silver and copper where synthesized and the efficacy of the pure nanoparticle and nanoparticle mixtures on antibacterial properties were evaluated. In addition, bimetallic silver/copper core-shell and shell-core structures were synthesized with microwave assistance. Bimetallic nanoparticles composed of two different metal elements are known to exhibit novel electronic, optical, catalytic or photocatalytic properties when compared to monometallic nanoparticles [19].The core-shell structures have exhibited interesting hybrid properties, which has resulted in increased attention over the last decade [19]. For example, bimetallic nanoparticles have been applied in the field of electrical devices, since they have shown greater electrical conductivity than pure metal nanoparticles [19–21]. Their optical properties are also different from those of the pure nanoparticles, since their microstructure results in a different hybrid optical index [22]. For example, Au-CuO core shell nanoparticles result in a tunable surface plasmon effect, which could be used on devices for photonic, electronic, and optoelectronic applications [23].For example, the visible range absorption could be used as agents for optical imaging [24] and also applied in solar cells [25]. By controlling the nanostructure of bimetallic nanoparticles, the optical index of the particles will be different from the pure metal particles,there would be a turnable surface plasmon resonance detected and the range of the extinction can be enhanced [24].

In the field of catalysis, Pd-Pt core shell particles have shown an enhanced catalytic effect in oxygen reduction compared to that of pure Pt nanoparticle [26]. In the background chapter, the synthesis of Ag, Cu and bimetallic NPs will be introduced and discussed.

One of the aims of this research is to study the synthesis of Ag-Cu bimetallic nanoparticle by chemical reduction with the assistance of microwaves. These metals have very different reduction potentials and therefore mixed metal nanoparticles are quite difficult to synthesize.

However control of the reaction sequence and reaction temperature, can be used to exert some control and different nanoparticle microstructures and compositions have resulted [27]. The synthesis method used in this work is described in Chapter 5 and characterization details is in Chapter 6. In this work, emphasis was placed on the use of a microwave reactor in one-pot and two-pot synthesis to control the reduction of copper in particular. The effect of the resulting nanoparticles on optical absorption in the visible spectrum was examined.

Silver nanoparticles are known to act as a powerful antibacterial mostly by being a durable source of silver ions in oxidizing environments [7]. However, there has been relatively little attention paid to nanoparticle of other heavy metal antibacterials. This is particularly important since the increasing use of silver nanoparticles in our human environment may result in silver resistant bacteria populations [16]. In this case it will be important to have other heavy metal antibacterials that are effective against silver resistant bacteria. Copper is a potential alternative and antibacterial efficacy of copper nanoparticles has been investigated even though it is more likely to oxidize in aqueous environments [28]. If copper is effective against silver resistant bacteria it is logical to consider mixtures of copper and silver nanoparticles since it is less likely that bacteria will be able to develop resistance to two different antibacterial mechanisms. In this study the antibacterial efficacy of copper-silver nanoparticles were tested against M.smegmatis silver resistant mutants as well as wild type to determine the effect of mixed nanoparticle populations. The solubility of Ag, Cu, Ag-Cu bimetallic and mixture of Ag and Cu NPs in aqueous solution was also studied in support of this goal since galvanic effects may occur for two metallic nanoparticles with different reduction potentials. Finally, the effect of patterning of silver nanoparticles on biofilm formation was studied. At present there is no way of controlling the spatial development of bacteria colonies and their merger into surface biofilms on filters. The usual solution is to use relatively large surface concentrations to avoid fouling of filters. However, the patterning of nanoparticle dots may offer a mean of preventing or delaying the fouling of filters with much smaller amounts of nanoparticles.

The sintering behavior of Ag-Cu bimetallic nanoparticles, especially Ag shell Cu core nanoparticles is of increasing interest [21, 29]. If it is possible to replace silver nanoparticles with nanoparticles of less expensive metals in the processing metal interconnects, the cost

of using patterned nanoparticle interconnects could be substantially reduced, especially if they can be sintered in air. Unfortunately, alternative copper nanoparticles do not sinter at the same low temperatures (150 °C to 200°C) as silver nanoparticles and copper tends to oxidize thus lowering electrical conductivity of the nanoparticle films. Copper core-silver shell particles have been proposed as a possible solution since the mass of silver replaced by the copper cores would preserve high electrical conductivity and reduce the material cost and the silver shell would prevent the oxidation of the copper core if sintered in air. To investigate the sintering behavior of copper-silver nanoparticles, the Cu-Ag core-shell and shell-core nanoparticles processed in this study were formed into films. After sintering at low temperature the electrical conductivities of the films were compared with those of films made with copper nanoparticles. Enhanced sintering would also be of interest to the antibacterial studies on biofilm formation in future studies. Low temperature sintering treatments, facilitated by the silver shells, could be used to bond the nanoparticles to the filters and reduce the leaching of antibacterial nanoparticles through microfilters into the filtrate liquid.

2.0 BACKGROUND

2.1 NANOPARTICLE SYNTHESIS

2.1.1 Pure Nanoparticle Synthesis

Pure noble metal nanoparticles such as Au, Ag, Cu etc have been synthesized using physical methods and chemical reduction. Physical methods include pyrolysis [30]. The biggest challenges for such physical methods are nanoparticle agglomeration and coalesce. This usually leaded to a relatively wide size distribution. Chemical reduction use metallic salt precursors a in liquid solvents. Metallic ions react with a reducing agent in the presence of capping agent and metallic particles nucleate. The nanoparticles then continue to grow by Ostwald ripening to reduce the surface energy [31].

Ag NPs

Colloidal metallic particles are usually synthesized by the chemical reduction method. Generally, a metallic salt is dissolved in an appropriate solvent in the presence of surfactants, forming a metallic core surrounded by a ligand shell [30]. Reducing agents such as $NaBH_4$, N_2H_4, ascorbic acid [14, 29], or ethylene glycol(EG) [29] are then added. NaBH4 was first used by Creighton et al [32] and commonly is used for Ag NPs synthesis in aqueous solution. NaBH4 is a strong reducing agent and can result in particles sizes ranging over 1 to 50 nm [32]. In this reaction, many small nucleates can be formed very fast in reaction with such a strong reducing agent. The reaction equation is listed below 2.1:

$$AgNO_3 + NaBH_4 \longrightarrow Ag + 1/2H_2 + 1/2B_2H_6 + NaNO_3 \tag{2.1}$$

Since the reaction is very fast and unstable, and hydrogen is released from the solution, the mixing speed must be well controlled to avoid an explode when a large amount is being synthesized. Also, $NaBH_4$ is very toxic. To replace the toxic reducing agent, ascorbic acid has been considered [33]. Ascorbic acid is a relatively weak reducing agent compared to NaBH4. Therefore, larger Ag NPs are produced under the same reaction conditions when compared to stronger reducing agents. The weaker reducing agent result in a low nucleation rate [34]. The reported Ag NPs synthesized by ascorbic acid are in the size range 20 to 100 nm [35] and 36-82 nm in the presence of PVP [36]. The reaction with ascorbic acid is shown below in equation 2.2.

$$2Ag^{+} + C_6H_8O_6 \longrightarrow 2Ag^{0} + C_6H_6O_6 + 2H^{+} \tag{2.2}$$

Polyol synthesis was originally developed by Fievet et al as a chemical reducing method to synthesize colloidal nanoparticles [37–40]. Examples of the application of this technique include: Ag, Au,Cu, Co,Ni, Pd Pt and even some alloy nanoparticles such as CoNi, and FeNi nanoparticles [37–40]. In the polyol reaction, the metal precursor is reduced by a polyol, i.e. ethylene glycol (EG) or polyethylene glycol (PEG). PVP is commonly added as stabilizer to prevent agglomeration. The mechanism of the reaction between $AgNO_3$ and EG is presented in equation 2.3 and 2.4. Once the silver ions concentration reach supersaturation, Ag nucleate and grow into nanoparticles in the size range 20 nm to 80 nm as time increases [41].

$$2HOCH_2CH_2OH \longrightarrow 2CH_3CHO + 2H_2O \tag{2.3}$$

$$2Ag^{+} + 2CH_3CHO \longrightarrow 2Ag^{0} + CH_3O - OCCH_3 + 2H^{+} \tag{2.4}$$

A small amount of inorganic salt (NaCl or NaHS) added to the reaction has been found to control the shape of the Ag nanoparticle [41, 42]. For example, adding a trace amount of sodium sulfide (Na_2S) or sodium hydrosulfide (NaHS) to the conventional polyol synthesis, greatly reduces the reaction times. As the reaction time is controlled, monodispersed silver nanocubes of 25–45 nm in edge length can be rapidly and routinely produced at relatively large scale [42]. High yields of single crystal (truncated cubes and tetrahedrons) silver

nanoparticles can also be synthesized by adding chloride (NaCl or KCl) to a standard polyol synthesis.

Wiley and co-workers [42] proposed that during the polyol synthesis reaction, the presence of air (O_2) over the reaction solution could lead to dissolution of the silver particles initially formed. The reduction of Ag ion competes with Ag dissolution by oxygen in the very early stage of particle formation. If the initial Ag nuclei morphology is single crystal, it will continue to grow. However, if the nucleus is a twinned crystal, it would provide active sites for oxidative dissolution and the crystallite would disappear. The addition of salts is thought to provide coordinating anionic ligands to the silver sol and could accelerate oxidative dissolution of twinned silver [43].

In this research, all three chemical reducing methods were applied. Ag NPs were reduced with $NaBH_4$, ascorbic acid and ethylene glycol respectively for different experimental purposes, which were described and characterized in the chapter 5 and charter 6.

Cu NPs

Synthesis of Cu NPs is more challenging than that of Ag NPs. Due to coppers oxidative tendency, the resultant particles could be Cu_2O, $Cu(OH)_2$ and even CuO NPs. Similar to Ag NPs synthesis, the chemical reducing agents used for Cu NPs synthesis include: $NaBH_4$, ascorbic acid and ethylene glycol. $NaBH_4$ is the most commonly used reducing agent for the synthesis. The reported sizes are in the range 30 nm to 80 nm [29] It is notable in the liu et al's study [44] that for low concentrations of $NaBH_4$, the final product contains Cu_2O, $Cu(OH)_2$ and Cu NPs. Only when large amounts of $NaBH_4$ was used were the oxidized byproducts avoided.

Ascorbic acid is a nontoxic alternative reducing agent that also used for Cu NPs synthesis. Much finer Cu NPs (2 to 20 nm) are produced in the presence of surfactants [45]. Ascorbic acid has also been reported to protect Cu from oxidation [46]. Ethylene glycol is another possible reducing agent, stabilizer and solvent. The Cu nanoparticle produced from the reaction of Cu acetate and EG gave pure Cu phase by XRD analysis [29, 47]. EG has the ability to prevent Cu NPs from oxidation and aggregation.

2.1.2 Dispersing Agent Effect

Dispersing agents also known as capping agent are commonly used in the synthesis to prevent nanoparticle aggregation. The aggregation is mainly caused by high surface energy and thermodynamic instability of the NPs surfaces. The dispersant lowers the surface tension in the suspension and disperses the particles. It also covers the surface and prevents excessive reaction between chemicals and nanoparticle surface.

Polymers such as polyvinylpyrrolidone (PVP), polyvinyl alcohol (PVA) or Sodium dodecyl sulfate (SDS), have been most commonly used in synthesizing Ag NPs [29]. PVP plays an important role in controlling the size of nanoparticles [48]. Zhang et al [48] found that PVP absorbed on the Ag nanoparticles and act as a barrier and inhibited inter-diffusion between the particles. Chou and Ren [49] proposed that increasing PVP concentration would produce finer Ag particles (7∼20 nm). However, too much PVP would slow down the reduction rate of Ag ions [49]. In this research, PVP was used in most of the synthesis reactions.

2.1.3 Bimetallic Nanoparticles Synthesis

For the metallic salt reduction process, the metal species with the highest redox potential generally precipitates first, forming a core on which the second component is deposited in the case of alloy nanoparticle [27, 50]. In this research, nanoparticles including Ag NPs, Cu NPs and Ag-Cu alloy nanoparticles were synthesized with chemical reduction methods. Also green synthesis, dispersion agents (PVP) and reducing agents (EG) were chosen to make the synthesis process and the nanoparticles themselves more environmental friendly.

The segregation of silver and copper metal during Ag-Cu nanoparticle formation is another interest in this research since heterogeneous spatial distribution of the metal elements caused by surface segregation, for example, could influence the rate at which the metals in the alloy nanoparticles are oxidized and released into solution. Since Cu nanoparticles could be used, in several applications, as a substitute for very expensive noble metals such as silver, recent years have seen interest in Ag-Cu core-shell particles. Very small core-shell nanoparticles consisting of polyicosahedra with a Cu core embedded in an Ag shell of the most stable size 34 and 40 (atom number) have been studied by DFT calculations [1, 2].

Figure:2.1 gives an example of two stable core shell polyicosahedral structure of $Ag_{27}Cu_7$ and $Ag_{27}Cu_{13}$ by DFT simulations [1, 2] in very small nanoparticles where Ag forms a shell. These simulation results indicate that silver atoms tend to segregate to the surface in Ag-Cu alloy nanoparticles.

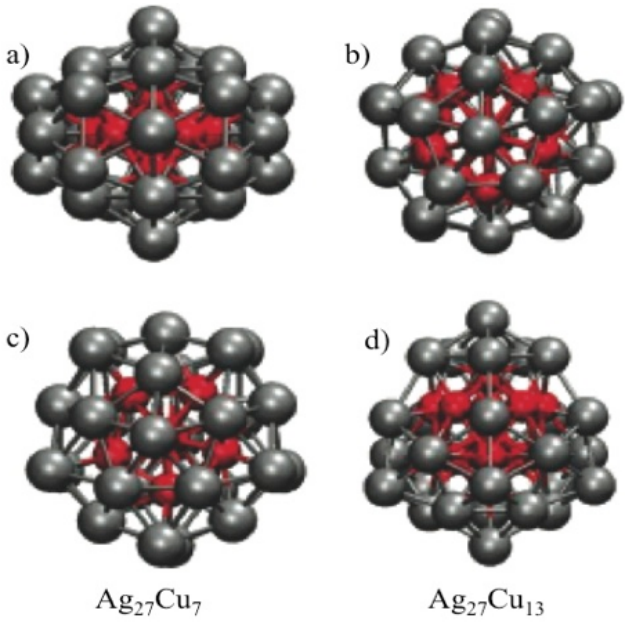

Figure 2.1: Two stable core shell polyicosahedral structure of $Ag_{27}Cu_7$ a)c) and $Ag_{27}Cu_{13}$ b)d) by DFT simulations [1, 2]. Black balls represent the silver atoms and red balls are copper atoms.

The tendency of Ag segregation originates from the interplay of atom size mismatch, combining bond order and bond length. The surface energy of Ag atom is lower than Cu atoms, which also indicates that the silver should tend to segregate outwards forming a shell. The segregation also relates to the atom sizes, Cu atom size is smaller than Ag. Usually, surface atoms contract when they are connecting with smaller atoms. In order to reduce the internal strain of a Ag/Cu cluster, the shorter bonds of Cu should grow internally, while Ag have longer bonds covering the Cu core. Thus, internal strain is reduced and the structure is more stable [30].

Consideration of the Ag-Cu phase diagram shows that one should expect a miscibility gap under equilibrium conditions as shown in Figure: 2.2. With a positive solid phase mixing enthalpy ($\Delta Hmix > 0$), Ag and Cu atoms tend to separate, and the most stable state is a mixture of two phases. One phase being almost pure copper and the other being almost pure silver.

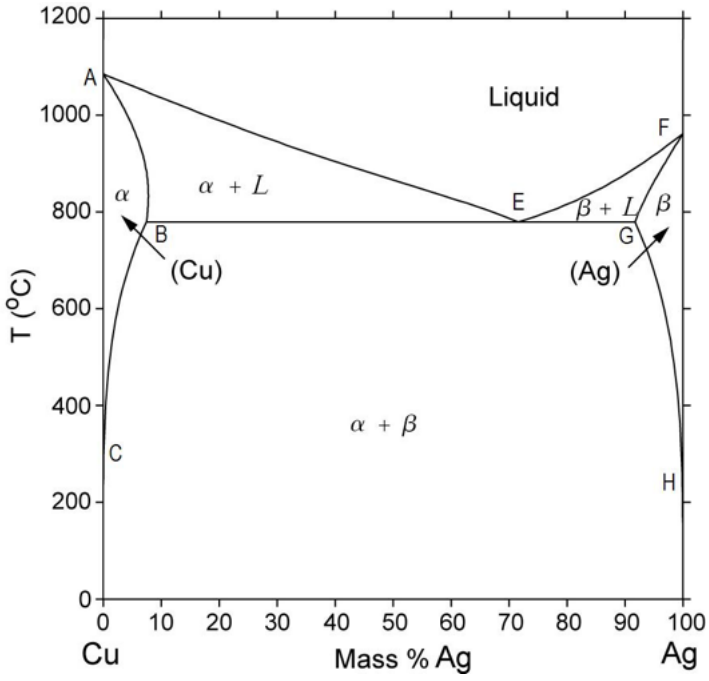

Figure 2.2: Ag/Cu phase diagram

Ag(core)Cu(shell) clusters have been generated experimentally by radiolysis of solutions containing copper and silver sulfate [51]. In recent years other research groups [3, 52–54], have applied chemical reduction methods to synthesize Ag/Cu. Their results did not give very strong evidence of core-shell structures in Ag-Cu nanoparticles. On the contrary, Jiang et al found both silver and copper 111 lattice planes in a particle (Figure 2.3) as one would expect from the phase diagram [3]. Fig.2.3(b) is a high resolution TEM picture of Ag/Cu alloy particle corresponding the Cu lattice planes. Fig.2.3(c) shows evidence of planes corresponding to the lattice value of Ag. It should be noted that these particles are much larger than the clusters modeled by DFT.

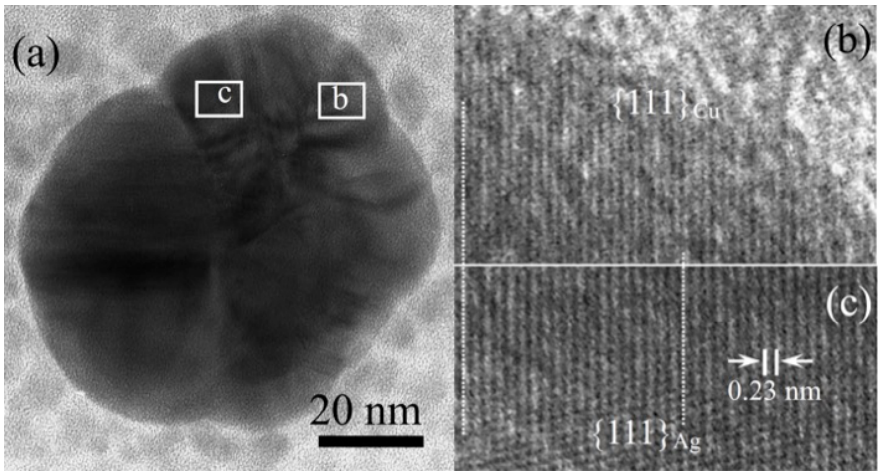

Figure 2.3: High resolution TEM picture of Ag/Cu alloy nanoparticles [3]

In the other research [27], ethylene glycol (EG) is used as a reducing agent and stabilizer. More complicated silver Ag/Cu alloy structures were produced according to different reaction conditions including reaction time and molar ratio of [Ag]/[Cu]. By varying the ratio of [Ag]/[Cu] molar ratios between 1 and 2 or by using short reaction times below 5 minutes, Ag rich Ag/Cu alloy particles were formed. This is not surprising since silver has a lower oxidation potential than copper. On the other hand, at low [Ag]/[Cu] molar ratios of 0.25 and 0.5 or at long reaction time above 15 min, Cu shells overgrew Ag/Cu cores and new Ag/Cu alloy core Cu shell nanoparticles, denoted as Ag/Cu@Cu, were produced [27]. The authors showed that the synthesis of bimetallic or the core-shell structures alloy nanoparticle are sensitive to reaction conditions. When reaction time increased, it was more likely to form a core shell structure. Therefore, the segregation in these relatively large Ag-Cu nanoparticles was determined by kinetics of the reduction reaction.

2.1.4 Microwave Effects on NPs Synthesis

Microwave irradiation is known to produce internal heating in polar liquids and increases the temperature of the whole volume of liquid uniformly. MW synthesis of NPs tends to be rapid and highly reproducible if uniform heating is achieved by suitable control of MW

output power, temperature and pressure [55]. In addition, NPs shapes have been controlled by applying different conditions during MW assisted synthesis to yield prismatic, cubic, hexagonal and spherical nanostructures of noble metals such as Ag, Au, Pt and Pd [56]. MW assisted synthesis can also be ecofriendly, avoiding the use of toxic chemicals. In contrast, oil bath heating is a conductive heating method using an external heat source. This is relatively inefficient due to the dependence on convection currents and thermal conductivity of the reaction media. Usually, the temperature of the reaction vessel is higher than the reaction medium, leading to non-uniform temperature profiles in the liquid and incomplete reactions [57]. With the assistance of MW reactor, the reduction rates of Cu NPs and Ag core Cu shell nanoparticles are greatly enhanced in this research.

2.2 EXPERIMENTAL TECHNIQUES FOR BIMETALLIC NANOPARTICLE CHARACTERIZATION

Since the proportion of metal elements, the mixing of elements and the oxidation of the metals may be sensitive to the synthesis technique it is necessary to have appropriate and complementary experimental techniques to characterize metal alloy nanoparticles. A combination of TEM, EDX, SAED, STEM, XRD, and UV-vis spectroscopy, can effectively characterize the proposed multimetal nanoparticles.

It is important to know the composition of the surface of the nanoparticles in order to evaluate the oxidative properties and sintering behavior of an alloy nanoparticle that would affect antibacterial properties [58]. X-ray photoelectron spectroscopy (XPS) can be used to study the surface of nanoparticles. This is accomplished by irradiating a sample of nanoparticles with monoenergetic soft x-rays and analyzing the energy of the electrons emitted. The emitted electrons have kinetic energies given by equation 2.5.

$$KE = hv + \Phi_s \tag{2.5}$$

where hv is the energy if the photon, KE is the binding energy of the atomic orbital from which the electron originates, and Φ_s is the spectrometer work function. The binding energy

may be regarded as the ionization energy of the atom for particular shell involved [59]. XPS measures the kinetic energy and analyzes the number of electrons that escape from the top 0 to 10 nm of a material. In order to know the surface composition of the Ag-Cu alloy, XPS can be applied to detect the possible oxidation shell of the nanoparticle and thereby characterize the elemental composition of the surface. XPS spectra are quantified in terms of peak intensities and peak positions. The peak intensities measure how much of certain type of atom is at the surface, while the peak positions indicate the elemental and chemical composition, an example was presented in Fig.2.4. By properly fitting the possible element peaks and analyzing the peak intensity and area with XPS fitting software, the percentage atomic concentration can be calculated [60, 61].

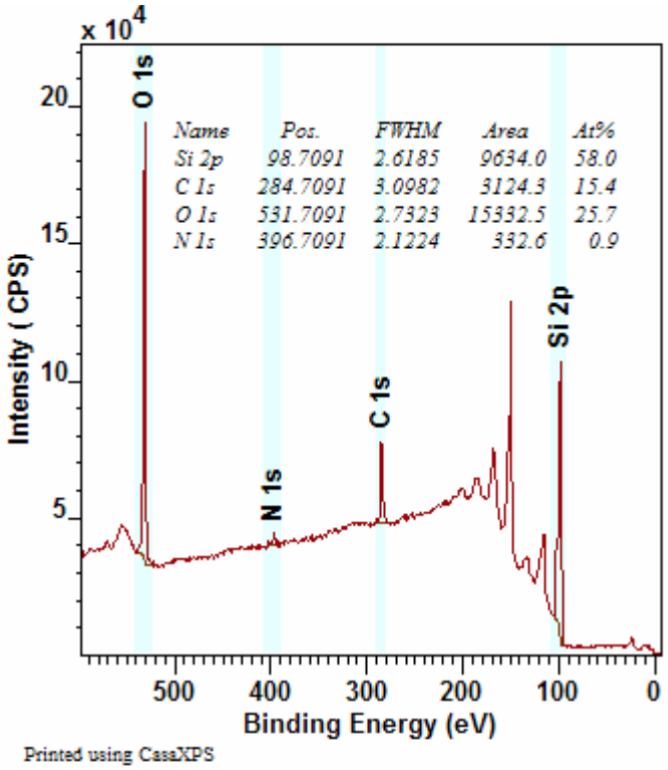

Figure 2.4: An example of XPS analysis chemical composition and percentage atomic concentration with Casa XPS software.

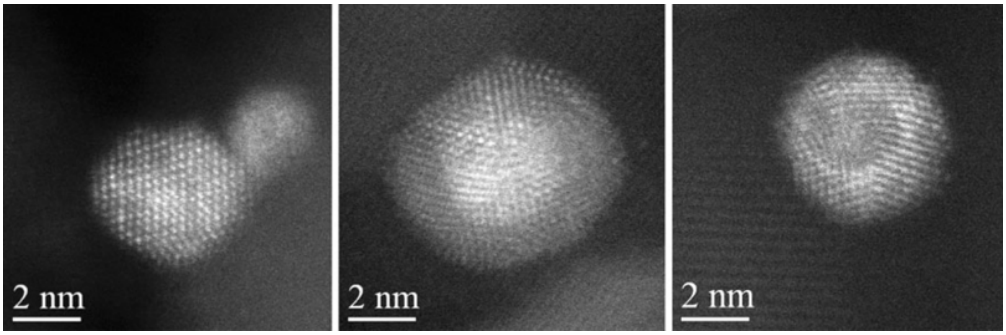

Figure 2.5: STEM-HAADF images showing (left) a AuPd homogeneous alloy particles, (middle) a AuPd nanoparticle with a gold core and a palladium shell, and (right) a AuPd nanoparticle with a palladium core and a gold shell [4]

.

Standard transmission electron microscopy characterization techniques including bright filed imaging, selected area diffraction and dark field imaging are routinely applied to determine the morphology and phase distribution in nanoparticles. In addition energy dispersive spectroscopy can be used to identify chemical elements and their spatial distribution, the later by STEM scanning transmission electron microscopy and chemical mapping. When the nanoparticles become very small it is often difficult to accurately determine the spatial distribution phases and elements due to the spot size of the electron beam. Then more sophisticated techniques are required such as HAADF or "Z-contrast" (HAADF image contrast is proportional to Z, where Z is the atomic number) which reveals the internal structure of the nanoparticle, based on the different electron scattering powers of different elements, thus revealing chemical information. This method is particularly useful for studying bimetallic nanoparticles where the constituent elements have similar lattice spacing, but have quite different atomic numbers. Figure 2.5 gives an example of the coreshell morphologies discerned due to the inherent Z-contrast of Au and Pd in high angle annular dark field (HAADF) STEM images. Au (Z = 79), has a higher atomic number than Pt (Z = 46), and exhibits higher brightness than Pt. Figure 2.5 shows three conditions of AuPd alloy nanoparticles. The STEM-HAADF image on the left is an AuPd homogeneous alloy particle where the

brighter Au atoms and gray Pd atoms are homogeneously distributed. In the middle of Figure 2.5 is an AuPd nanoparticle with a gold core and a palladium shell because of a bright interior region and a gray annular region. Figure 2.5 (right) is an AuPd nanoparticle with a palladium core and a gold shell, where Pd atoms is mainly distributed in the interior region and Au atoms in the annular region [4].

This technique could be applied to copper and silver alloy nanoparticle [5]. However, the experimental procedures of HAADF–STEM should be well adjusted by increasing the collection angle through decreasing the camera length to restore a contrast linked to the positions of silver and copper atoms [5]. Figure 2.6 is an image example of the bimetallic Cu-Ag nanoparticles by pulsed laser deposition at MPQ-CNRS laboratory. With a large difference of atomic number between Cu (Z=26) and Ag (Z=47), the lattice contrast could be attributed to the segregation of Cu and Ag inside the nanoparticle. In Figure 2.6, the bright region of a particle is silver and the gray region of a particle is the copper component.

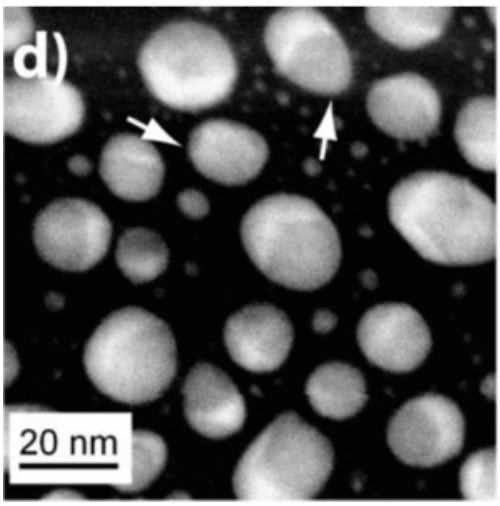

Figure 2.6: HAADF image contrast of a Ag-Cu bimetallic alloy nanoparticle [5].

2.3 PROPERTIES AND APPLICATIONS OF METAL NANOPARTICLES

2.3.1 Nanoparticle Antibacterial Effects and Ion Release

Water is essential human life. There is plenty of water globally but potable water is not evenly distributed and is difficult to transport in some areas. It has been reported that over one billion people in the world do not have access to safe water and more than two billion suffer from inadequate sanitation. Also, the water used by poor populations is often contaminated, spreading waterborne diseases that kill people or leave them unable to work for long periods. The United Nations Development Programme (UNDP) estimates that nearly half of all people in developing countries at any one time are suffering from an illness caused by unclean water or poor sanitation [62].

Bacterial infections are also important in the first world, but tend to be an issue for the food supply rather than drinking water [63]. Hospital acquired infections are also an important concern [64]. In addition, 2/100,000 of the population get infections by mycobacteria species such as tuberculosis and leprosy which are not waterborne and Non-tuberculous mycobacteria (NTM) such as M. avium which can be a waterborne opportunistic pathagen. The incidence of mycobacteria infection is again rising in the immunocompromised and immunosupressived patients, especially those with AIDS [65]. NTM is also known to be one factor responsible for cervical lymphadenitis in children [66].

Antibacterial agents have been applied in medical and public health fields such as water disinfection, medicine, and food packaging. Among the antibacterial agents, organic compounds have some disadvantages, including toxicity to human body, contamination of the environment [67] and increasing antibiotic resistance [68]. Therefore, there has been renewed interest in inorganic disinfectants such as heavy metals [8, 68] particularly the nanoparticles form, due to their potential for durable surface protection. Additionally, some metal nanoparticles can locally kill bacteria without damaging the surrounding tissue [69], when used in wound healing and other in-vivo applications.

2.3.2 Mycobacteria

Environmental mycobacteria normally inhabit a broad range of natural microenvironments, including natural water, aerosols, animals and humans. They can be isolated from biofilms, aerosols, dusts and even human cigarette [66]. Mycobacterium is a genus of actinobacteria, including some famous pathogens such as M.tuberculosis and M. leprae, which cause tuberculosis and leprosy respectively. There are other species of environmental mycobacteria called non-tuberculous mycobacteria (NTM), including M. avium, M. marinum and M.Smegmatis. The biofilms of the NTM exist in nearly every water distribution system [70]. The mycobacterium avium complex (MAC) contains opportunistic pathogens that also lead to infections in patients with compromised immune system. M.avium causes infections in humans primarily through water sources. Indeed, it has found that the DNA-based fingerprint of M.avium isolated from AIDS patients was identical to the isolates taken from their drinking water [64]. The primary infection routes appear to be oral and aerosol [66]. When AIDS patients were exposed to high flow rates of water from showerheads and taps it increased the risk of infection [71]. NTM also shares a large fraction of genes with M. tuberculosis [72]. Another important species of mycobacteria is M. marinum, which is non-pathogenic, but can lead to skin infection in people who have high exposure to fish. It shares proximately 85% of genes with TB, and 99.8% genetically similar to M.ulcerans [72]. M. smegmatis, which is commonly used in planktonic mycobacteria experiments and biofilm research because it is non-pathogenic and a fast grower, shares 78% of its genes with water borne bacteria such as M.avium [73] . The preparation for the rapidly growing M.smegmatis only requires two to three days while the slowly growing pathogenic mycobacterial species requires longer periods of time. It can take two to eight weeks for some of the slow growers to develop colonies [63].

Mycobacterial cells are rod shaped, between 1 to 10 μm long and 0.2 to 0.6μm in width. They have a thicker cell wall than other species of bacteria, which is waxy and hydrophobic. The cell wall of mycobacteria provides added protection for this genus because it has a thin peptidoglycan-based cell wall and a cytoplasmic outer membrane [63]. The fluidity and hydrophobicity of the cell surface is determined by mycollic acids, which contribute to the low permeability of mycobacteria. It also enables the mycobacteria to survive and grow over a

wide range of pH and temperature. Almost all mycobacteria can grow in media at acidic pH values between 5 to 6.5 and little growth are found when the environmental pH increases above 7.5. Also, mycobacteria are able to modify the composition of their membrane lipids to help them survive and grow in a large range of temperature from 10 to 45 °C [66]. This explains why M.avium and M. xenopi have been found in hot water systems.

Mycobacteria can resist a large variety of antibiotics and disinfectants. This is partly due to the impermeability and hydrophobicity of the cell wall. The lower efficacy of antibacterial against mycobacteria can be explained by the following mechanisms. First, the transport protein related to the membrane mediates the efflux of antibiotics from mycobacterial cells. Also genetically, the presence of innate genes produce enzyme such as b-lactamases, which could generate tetracycline resistance [68]. The susceptibility to chlorine has been measured as extremely resistant. The resistance to chloramine, chlorine dioxide and ozone in M. avium is extremely high and so the disinfectants used for water sterilization are not that effective [74], especially when the biofilm is formed in a distribution water system [64].

2.3.3 Susceptibility of Mycobacteria to Metals

Like other bacteria, mycobacteria are susceptible to transition metals like silver, copper and zinc[9]. Most of the transition metals have incompletely filled d orbitals, which enables their cations to form complex compounds. The complex compounds play the main role in the toxicity of heavy metals to bacteria. In order to have a toxic effect, most heavy metals or metal ions have to penetrate the cell wall [68]. In hospital warm water systems copper and silver ions have been used as disinfects to kill mycobacteria [75]. However, when legionellae and mycobacterial biofilms are formed, it is hard to effectively kill the bacteria and eventually the antibacterials lose their effectiveness. The resistance of mycobacteria to silver can be selected by frequently treatment with silver ion which naturally selects a sub population which contains mutations that confers resistance to silver [76]. The silver resistant character of the mutation strain is encoded on plasmid-mobile genetic elements facilitating the spread of the mutants [77].

There are three possible mechanisms for enhanced heavy metal ion resistance. First, metal ions are expelled by efflux driven by chemiosmotic gradient across the cytoplasmic membrane of bacteria [68]. Second, cations can from complex compound with thiol-containing molecules. Third, metal ions are reduced to a less toxic oxidation state. Usually, the reduction products formed with heavy-metal ions are insoluble or even more toxic than the precursors from which they are formed, and this leads the cells to detoxifying by efflux. Most of the mechanisms for detoxication in cells are through efflux because it cost less bioenergy, except in low concentration of heavy metals when complexation would be a more efficient way of detoxification [68].

2.3.4 Biofilms

In most natural ecosystems, bacteria prefer growth at interfaces as biofilms. Bacterial biofilms are microcolonies developed by bacteria attaching to an organic or inorganic surface. The organized communities of microbial cells exhibit adherence, and encapsulation in a self-produced protective extracellular matrix. Although biofilm formation has been recognized for over 100 years, the importance of the biofilm state to antibacterial action has only been widely appreciated in recent decades [6, 78]

2.3.5 Stages of Life Cycle and Structure

There are five stages in the life cycle of bacteria in Fig.2.7: Firstly, individual planktonic cells attach to the surface and undergo genetic changes and lose the flagella. Secondly, extracellular polymeric substance is produced and attachment becomes irreversible. Then, the biofilm grows into colonies and then a continuous, multilevel cooperative community in the 3 and 4 stages. Finally, individual cells grow flagella, detach and disperse from the biofilm, to colonize other surfaces [6]. In the first stage, sessile bacteria find a stable juxtaposition with cells of the same and other species to form microcolonies [79]. In the first stage, sessile bacteria find a stable juxtaposition with cells of the same and other species to form microcolonies [79]. In the colonization stage, the bacteria produce a slimy matrix of extracellular polymeric substance(EPS) which provide a desirable growth environment for more bacteria.

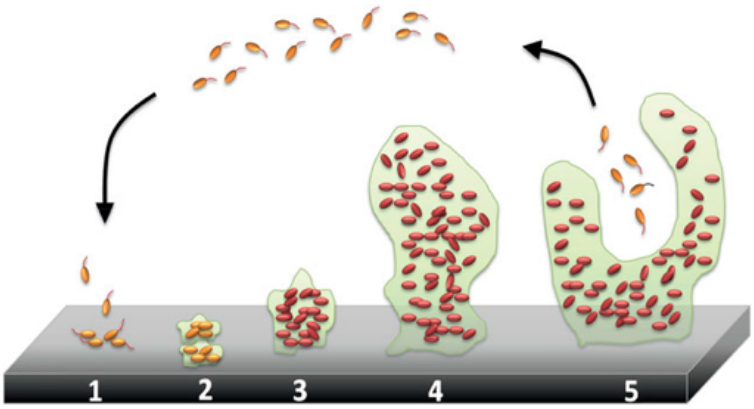

Figure 2.7: Schematic diagram demonstration of biofilm development and progression [6]

EPS is a mixture of high molecular weight polysaccharides and proteins. The heterogeneous biofilm architecture is more efficient and beneficial than a random mixture of floating microbial cells. Also, biofilm formation provides protections from environmental such as UV and acid exposure, metal toxicity, dehydration, salinity and antibiotics [78].

In the detachment phase, the individual bacteria are released or sloughed off from pieces of biofilm to colonize elsewhere. There are three mechanisms in this stage: swarming dispersal, clumping dispersal and surface dispersal. For swarming dispersal, motile cells are released from the biofilm and swim out by the convective flow current leaving a hollow mound. For clumping disposal, aggregates glide or shed from the biofilm. Thirdly, whole biofilms can move across surfaces through shear-mediated transport, which is called surface dispersal. The needs for flow in all these mechanisms explains the flexibility and tenacity of biofilms to environmental shear stresses [78].

2.3.6 Biofilms in Wild and Human Environment

Since individual bacteria cells are vulnerable, they prefer to form biofilm to survive in the environment. Biofilms have been detected amongst ancient prokaryotes according to their fossil records, which indicate that biofilms developed an adaptation to severe conditions experienced in primitive earth environments such as extreme temperature, pH and exposure

to UV light [6].Biofilms are found in many environments from fast-moving waters, hot spring and wetland systems. They can form on hard rock and minerals as well as on the surfaces of plant roots and animal intestinal systems [78, 80].Biofilms also play an important role in influencing the natural system and human environment in ways that are both beneficial and harmful. For example, biofilms can help wetlands filter toxin. The most common biofilms that we encounter daily are on our teeth, they are collectively called plaque and consist of multiple bacterial species. Dental biofilms are subjected to harsh environmental conditions in the oral cavity such as pH changes and exposure to detergents when we brush our teeth [81]. Despite this bacteria can still colonize the tooth surfaces leading to undesirable effects like discoloration and cavities, although such colonies are usually harmless and can help protect the teeth from direct exposure to dangerous pathogens [82].

In some circumstances biofilms can cause severe infections. For example, biofilms can grow on medical devices and thereby enter wounds and cause infections. Medical devices such as intravenous catheters, joints prostheses, endotracheal tubes and heart valves, are significant medical tools necessary to save peoples lives. Unsurprisingly, it has been found that bacteria dwell in these devices and increases the risk of infection. Biofilm formation on medical implants can even cause the failure of transplantation. Bacteria can also colonize the skin and have been found in wounds and implant sites [6]. When a biomaterial is implanted into human body, a phenomenon called "race for the surface " occurs on the implant [83]. It is described as a race between microbial adhesion and biofilm growth on one hand and tissue integration on the other. If the bacteria attach to the surface first, the implant will be rapidly covered by biofilm and tissue cell functions will be impeded causing inflammation. Unfortunately, bacteria are frequently introduced on an implant surface during the surgery, and so colonization of bacteria may start before tissue integration can occur [83].

Biofilms can also form in our human environment such as in air condition units and showerheads, spreading diseases and potential pathogens that cause health concerns [71]. Feazela et al [71] examined dozens of showerhead biofilms and detected quite large amounts of pathogenic M. avium in microbial communities. This also partly explained why mycobacteria infections can occur when biofilms do not originate within the body because bacteria can be easily aerosolized and inhaled or ingested.

2.3.7 Biofilm Resistance Properties

Biofilm cells are at least 500 times more resistant to antibacterial agents than the same species in the planktonic state [79]. When the biofilms have grown past the attachment and colonization stages, they become robust and pervasive. Three mechanisms would explain the enhanced resistance of biofilms to antibacterial agents. The first protection is the low permeability of the extracellular polymeric substance (EPS). Before bactericides reach the individual bacteria cells within the biofilms, they can be neutralized by binding with the EPS. EPS also protects biofilms from UV light exposure and dehydration. The second mechanism is physiological resistance, which comes from the protection by the stationary phase or dormant zones with in the biofilms [84]. The stationary phases occur when the death rate and growth rate of cells are equal due to the depletion of essential nutrition. Even though antibiotics can penetrate the EPS, they require some degree of cellular activity to disrupt the microbial process. Thus, the effectiveness of antibiotics is restricted if the cells remain dormant. The third mechanism of protection could be the existence of subpopulations of resistant phenotypes in the biofilms [83].

Directly after attachment but before colonization, biofilm may be more vulnerable when the constituent microbes most resemble planktonic bacteria, and so might be more efficiently controlled by antibacterials. Therefore its necessary to understand the susceptibility of microbial cells within the biofilms to toxicity of metals in the planktonic stage or the early stages of colonization when the bacteria are most vunerable [85]. Many metal ions can penetrate the biofilms and exert toxicity on biological system, in which multiple biological pathways can occur simultaneously. First, metal ions can replace one another at the binding site of a biomolecule, the substitutive ligand binding disables the biological function of the molecule. Then, redox reactions with cellular thiols groups (R-SH) and the Fenton-type reactions from transition metals can produce toxic reaction oxygen species (ROS). Also, transport of metal ions can compete with and inhibit membrane transport processes. Finally, siphoning electrons from the respiratory chains can reduce protons on the cell membranes [85]. Surfaces that have been treated with antibiotics may resist attachment and colonization of biofilms. There are some commercial products that are treated with silver ion or silver

nanoparticles such as socks [86], washing machines [87] and silver treated ceramic water filters, the latter have been proven to reduce planktonic bacteria in effluent waters [88].

2.3.8 Silver, Copper and Zinc Antibacterial Properties

The antimicrobial properties of silver and copper have been known since ancient times [89], it is said that nobles used silverwares and bronze wares to hold and process food, partly for the purpose of sterilization. Nowadays, silver ions and silver nanoparticle are widely applied in medical devices including catheters, burn wound dressings and dental materials [90]. Silver exhibits an oligodynamic effect, which is the ability to inactive bacteria in very small concentration. Silver is a broad spectrum antimicrobial and can be applied to a wide range of bacteria with little negative health impacts on humans compared to the transition metals. Typically, silver ions, like most metal ions, must enter the cell and damage the cell membranes.

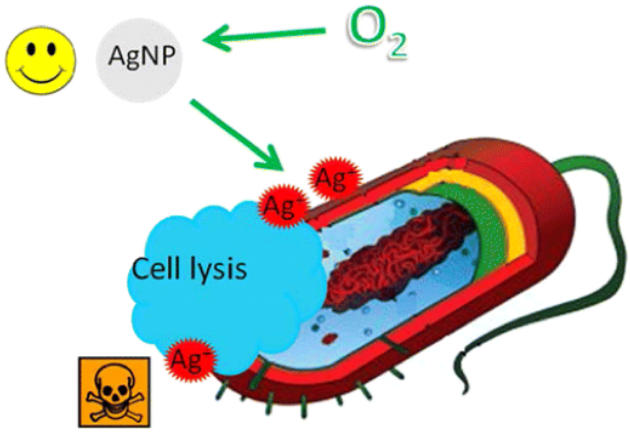

Figure 2.8: Schematic of Ag NPs, Ag ions, and cell interactions. Ag NPs may serve as a vehicle to deliver Ag^+ more effectively [7]

The silver nanoparticle antibacterial mechanism is thought to be essentially that of the silver ion. Firstly, in an oxidizing environment silver nanoparticles release silver ions into the fluid, which inhibit a respiratory enzyme and generate reactive oxygen species [7]. The

process is illustrated in Fig.2.8. Secondly, there is tendency of silver ions to bind with sulfur or phosphors groups on the proteins and DNA in cells. Silver ions can also disrupt the membrane morphology, increase the permeability of the membrane and eventually inactivate the bacteria [91].

Copper also shows great antimicrobial performance. In 1983, it was reported that using brass and bronze on doorknobs helped prevent the spread of microbes in hospitals [8]. The electrochemical potential of Cu^{2+}/Cu^{+} makes it easy to interact with radicals derived from molecular oxygen. Copper toxicity is mainly from its radical character, particularly the production of hydroperoxide radicals, and its interaction with the cell membrane [68]. However, recent research found that the antibacterial action of copper nanoparticle was not only through the route of Cu ions released from the NPs, but also through forming complexes between NPs and cellular medium organics [90].

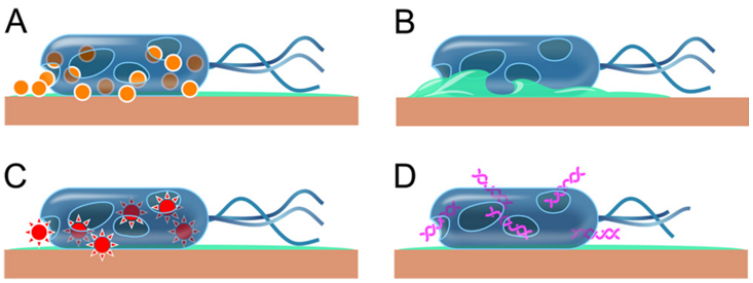

Figure 2.9: Schematic diagram of the tentative events in contact killing. (A) Copper contact the cell surface (B) The cell membrane ruptures, leading to loss of membrane potential and cytoplasmic content. (C) Copper ions induce ROS cause further damage. (D) DNA becomes degraded [8].

A number of mechanisms for Cu toxicity have been suggested. First, reactive hydroxyl radicals can be generated in a Fenton-type reaction. The hydroxyl radical can cause oxidation of proteins and lipids and degrade cellular molecules. Secondly, copper ions can lead to depletion of sulfhydryl in the proteins [8]. Thirdly, the replacement of other metal ions at important binding sites on the protein can cause the death of the cells. Finally it is possible that silver and other metal nanoparticles could act by direct contact which is thought to

act by the following steps shown in Figure 2.9: (i) successive membrane damage, (ii) copper influx into the cells, (iii) oxidative damage, (iv) cell death, and DNA degradation.

Our previous work showed that under prolonged exposure to Ag^+ and Ag NPs could lead to silver resistance [16]. However, the silver resistant mutants were found to be more sensitive to copper and so Cu NPs is a focus in this research due to its toxicity to bacteria, especially to the silver resistant mutants.

Zinc is less toxic to bacteria than copper. ZnO is generally recognized as relatively safe by U.S. food Food and Drug Administration. Recent studies have shown that ZnO nanoparticles have selective toxicity to bacteria such as E.coli, but exhibit very limited effect on human cells [92]. Zinc oxide (ZnO) nanoparticle has been widely applied in food package, antibacterial ointment, and surface coating on medical devices due to its antibacterial activity. Even at low concentration, ZnO nanoparticle can induce morphological changes and produce ROS(H_2O_2), causing membrane leakages, and increasing the oxidative stress gene expression in bacteria [93]. Finally, the exposure leads the death of the cells.

2.3.9 Nanoscale Effects

Nanoparticles (NPs) are usually defined as particles with at least one dimension between 1 and 100 nm. The bactericidal effect of metal nanoparticles has been attributed to their small size and high surface to volume ratio, which allows them to quickly release ions by oxidation, interact closely with microbial membranes and also penetrate the cell wall. The high surface to volume ratio increases their reactive ability per unit weight of material, requiring less material for a given application. Compared to the bulk metal, nanoparticles exhibit enhanced chemical and electrical properties [94]. They also show confinement effects including shape-catalytic property, which can affect the selectivity and toxicity [91]. Therefore, the antimicrobial activity of nanoparticles is not only dependent on the size [95] , but also to a certain extent on the shape of the particles [91]. The antimicrobial mechanisms could be more complex because the function of metal nanoparticles may not be to merely release metal ions in solutions [96]. It is clear that metal nanoparticles can be immobilized and coated on to surfaces of medical devices, filters and implants to prevent possible infections.

2.3.10 Disadvantages of Nanoparticles

Although nanoparticle antibiotics show advantages including material saving, higher efficiency and selectivity to shorten antimicrobial treatment time, there are still several drawbacks of nanotechnology for clinical use.

Firstly, when nanoparticles are syntheisized from broad spectrum antibiotics and used to target particular organisms, they can also influence non-target organisms. The non-target species such as environmental plants, animals or humans might be adversely exposed to the NPs for an uncertain time period. For example, it has been found that prolonged exposure to soluble silver-containing compounds may produce an irreversible pigmentation of the skin. In addition, there are some more sever toxic effects of silver including irritation and changes in blood cell count [67]. But in general, AgNPs are a non-toxic antibiotic and reported to be of minimal risk to human health at controlled concentrations [67]. Generally, human cells can easily resist AgNPs due to their complexity, in particular they have a nuclear membrane that protects the DNA from damage. In terms of copper nanoparticles, exposure to large doses of CuNPs by inhalation or ingestion have been shown to induce inflammatory responses in the lungs of mice [97]. It has been also been reported that copper nanoparticles have higher cytotoxicity and CuO nanoparticles can cause DNA damage and oxidative lesions compared with other metal oxide nanoparticles such as ZnO, TiO_2 and carbon nanotubes [98]. Exceeding dissolved copper ion limits in drinking water can also cause adverse health effects, including vomiting, diarrhea, stomach cramps, and nausea. It has also been associated with liver damage and kidney disease. The U. S. Environmental Protection Agency (EPA) established rules for controlling copper levels in public water supplies. Steps should be taken to reduce exposure if this level of 1.3(mg/L) is exceeded [99].

However, the potential toxicity of different doses of Cu NPs to human health still need further clinical research and elucidation due to the lack of relative research data [67]. In terms of the environment, a study reported that AgNPs, CuO and ZnO nanoparticles all showed adverse effects on aquatic species such as algae and fish that was concentration dependent [100]. The quantification of the toxicity of nanoparticles requires further study. Nanoparticles exhibit size and shape specific properties that limit the use of currently avail-

able in-vitro assays in a universal way, for there is no standardized definition for NP doses in mass, number or surface area [67]. Also, new characterization techniques will be required to reveal the nanoparticle toxic actions at the molecular and genomic level. Finally the cost of antibacterial nanoparticles is also a limiting factor due to the need for advanced processing techniques and high purity precursors.

2.4 DEPOSITION OF NANOPARTICLES

Once metal nanoparticles have been synthesized they must be deposited and retained on surfaces to realize the required electrical properties of nanoparticle interconnects or the antibacterial strategies that prevent biofilm growth. Techniques used to deposit nanoparticles will now be reviewed.

2.4.1 Mechanisms Of Self-Assembly

Solute self-organization during the evaporation of a colloidal droplet is a common phenomenon through non-covalent interactions including: hydrogen bonding, Van der Waals forces, electrostatic forces and interactions among solvents and solutes. For example, the well-known coffee ring effect describes the pattern formation leading to a coffee ring stain [10]. Particles in a drying droplet are driven to the edge and form a perimeter ring by outward flows. Pattern formation in a drying sessile droplet is a relatively simple and repeatable experiment to carry out but the final patterns depend sensitively on the interplay of complex physical mechanisms. As Deegan has described, capillary flow can develop a contact-line deposit by forcing the suspended particles in the solution to the edge of a drying drop forming a peripheral ring. In contrast to capillary flow, Marangoni flow, an inward radial flow caused by convective heat transfer, recirculates the particles along the droplet surface and draws them to the center of the drop, which finally forms an axisymmetric pattern. Deposition patterns are also influenced by contact line depinning and particle concentration effects [101].

Interactions among solute(s), solvent and substrate also play a role in the drying system in addition to the flows just described. A variety of experimental systems combining a variety of solvents and solutes have been studied by researchers interested in sessile drop evaporation and particle self-organization. Particles including polystyrene nanospheres and microspheres [9, 102], gold nanoparticles [103], and carbon nanotubes [104] in aqueous solutions have been investigated. The influence of chemical properties and interactions of the nanomaterials affect their wettability and surface charge which, under controlled circumstances, allow spontaneous formation of self-assembled patterns [102, 104]. For example, silica microspheres in a water-based ink on a hydrophobic substrate aggregate at the peripheral region with a microsphere poor central region in Fig.2.10.

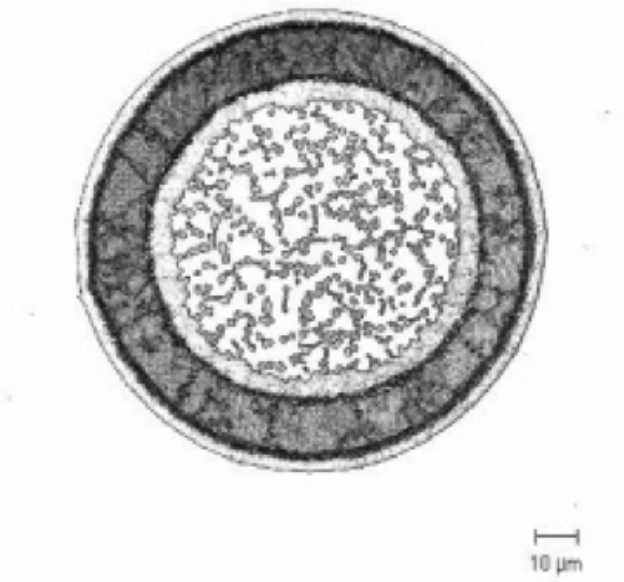

Figure 2.10: Silica microspheres [9]

2.4.2 Evaporation Induced Self-Assembly

The phenomenon of droplet evaporation has been studied for many years. As early as 1805, Thomas Young introduced the concept of contact angles between the boundaries of three phases (solid, liquid, and vapor) and proposed an equation (Youngs equation) to explain the

equilibrium between the three phases. Much more recently pattern formation from evaporating sessile droplets has become an attractive topic due to its applications in various fields (i.e. printing, coating, and medical diagnostics) [105–107].

Suspended particles in fluids are generally driven to the perimeter of evaporating droplets and accumulate in a peripheral ring due to the coffee ring effect. Pattern formation in evaporating droplets can be influenced by wetting properties, fluid dynamics, phase transitions, sedimentation, heat transfer, and the physiochemical properties of the solution.

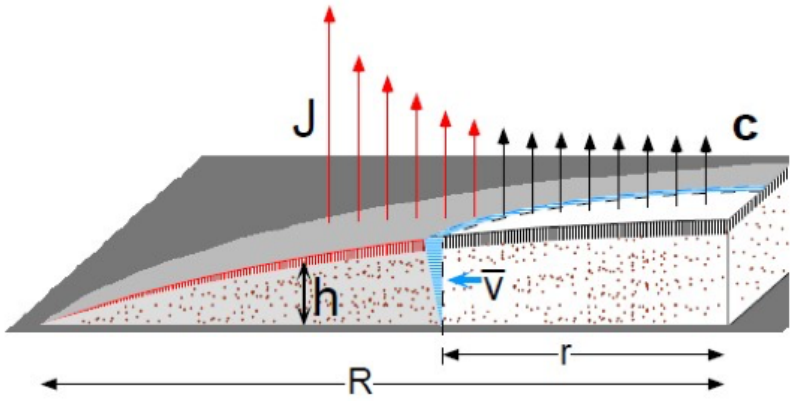

Figure 2.11: Schematic of outward flow of a dying droplet and evaporative flux (J) [10]

The coffee ring form is a general pattern first described quantitatively by Deegan et al [10] in Fig.2.11. They showed that capillary flow induced by evaporation drives the suspended particles in a droplet to the pinned periphery of the droplet where they aggregate to form a rim. If the contact line is pinned, the contact angle of the drop decreases during the evaporation of solvent. A non-uniform flux (J) is induced as the droplet shrinks in Fig.2.11, which increases from the central region to the perimeter as the contact angle decreases. By tracking particles of polystyrene microspheres in water, a relationship between the depth-averaged velocity v(r) and mass of the ring M (R,t) was determined in their research, which can be applied in predicting the morphology of a ring of a drying droplet. Regardless of the chemical properties of the solute and the substrate, deposition induced by capillary flow could be controlled and predicted. In this picture a prerequisite for the ring formation is

pinning of the droplet at the interphase boundary creating a constraint for particles spreading and accumulating.

Hu and Larson examined the effects of Marangoni stresses on the microflow in evaporating sessile droplets [108]. Induced by the latent heat of evaporation, Marangoni flow is a circulatory flow reversing particles back to the central region, counteracting capillary flow. Suppression of Marangoni flows is required in the formation of rings. Hu and Larson also described that a pinned sessile drop is a quasi-steady state found to increase the evaporation rate [109]. They calculated the evaporative velocity fields by finite element methods with Marangoni-stress boundaries for different contact angles. Surface tension gradients generated by latent heat in the solute affect the deposition patterns on the substrate. They concluded that a positive Marangoni number at a large contact angle can lead to an inward radial flow while a negative Marangoni number at a small contact angle produces to an outward flow.

Several techniques have been introduced to control the pattern formation. The techniques include evaporative flux, contact line depinning [10], and particle-substrate interaction [110]. A numerical model has been proposed by Bhardwaj et al [101] combining fluid dynamics, heat transfer and particle transport to simulate the formation of deposits during the evaporation of a nanoliter colloidal solution. Different flow patterns caused by the competition of Marangoni loops and radial flow are shown to determine the deposit shape to be either a ring-like pattern or a homogeneous bump [101].

2.4.3 Inkjet Printing Fabrication

Thin film fabrication methods include vapor deposition, spin coating, ink-jet printing, vertical colloidal deposition, and doctor blade process, etc [111, 112].

Doctor blade (or tape casting) is one of the widely used techniques to producing thin films on large area surface. Prepared nano-fluids and nanoparticle pastes are placed on a clean substrate (glass or plastics). Scotch tapes may be used to guide the doctor-blade for desired pattern and thickness. The wet film thicknesses ranges from 10 to 500 μm. The final dry thickness of the coated film, d, can be calculated from an empirical relationship in equation 2.6. [113].

$$d = \frac{1}{2} * g\frac{c}{\rho} \tag{2.6}$$

where g is the gap distance between the blade and the substrate, c is the concentration of the solid material in the ink in cm^{-3} and, ρ is the density of the material in the final film in cm^{-3} [113]. In making the films for resistivity measurement in this study, doctor-blade printing was used.

Ink-jet printing systems have been applied to print evenly distributed patterns of colloidal nanoparticles on membranes. Certain patterns [114], circuits [115], or a single uniform layer could be designed and fabricated by ink-jet printing. Designing a printing scripture with desired printing drop numbers can control the printing volume of colloidal particles solutions. There is also a drop shape analysis function shown in Fig.2.12 in some ink-jet printers. The drop analysis can measure each printed drop shape and size. With accumulated numbers of drops, the volume of each deposited spot could be calculated. By knowing the initial concentrations of the particle suspension and prescribing the movement of print head, it is possible to control the deposition patterns, using variables such as the drop sizes and distances between the drops in the patterned array of spots.

Figure 2.12: Drop shape analysis (from microfab co.)

2.4.4 In-situ Nanoformation within the Filters

A new approach for point-of-use water filters is in-situ nanoparticle fabrication that combines nanoparticle formation and deposition on a substrate or within a porous material in Fig.2.13. Dankovich et.al. embedded silver nanoparticle in blotter papers to purify drinking water contaminated with pathogenic bacteria. They first immersed the blotter papers to saturate them with silver nitrate solution to provide the silver ions. Then, after immersing in $NaBH_4$ solution with 1:1 molar ratio, silver nanoparticles were formed within the cellulous structure of the papers [11]. The AgNPs are observed to have a size less than 10 nm and the filters showed promising antimicrobial efficacy against E. coli. This product could be used as a portable filters for emergency drinking water treatment in the areas with scarcity of water resources. Also the in-situ reduction technique chemically bonds the particles to the substrate, therefore, fewer particles are released into the liquid improving silver retention and longevity of the water purifier.

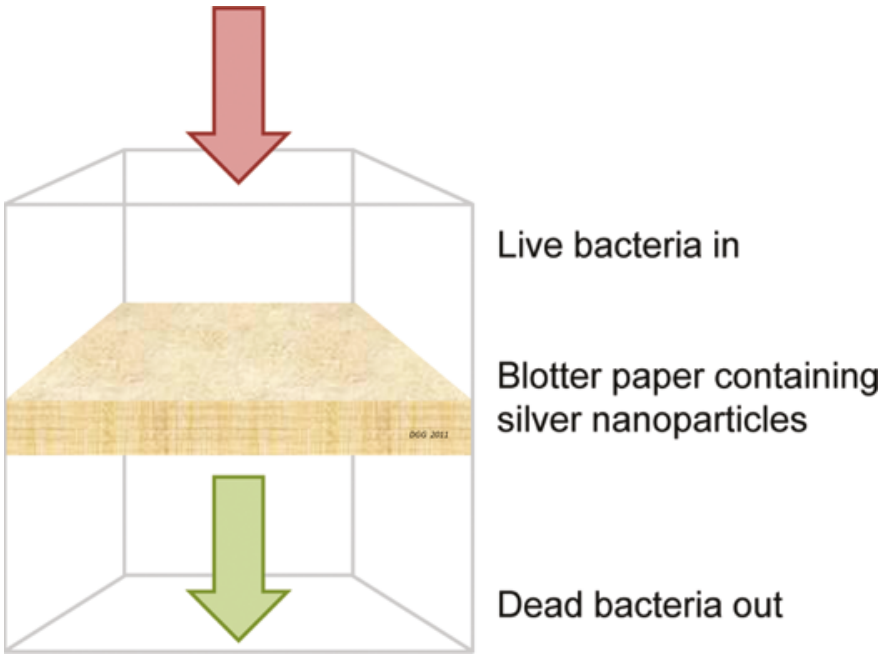

Figure 2.13: Demonstration of water filter [11]

2.5 METAL NANOPARTICLES ION RELEASE

Ionic activity associated with a nanoparticle suspension greatly effects environmental toxicity and particle stability/durability [116]. Metal ions released from NPs in water are considered to be the main function of antibacterial nanoparticles which eventually deactivating the bacteria as discussed in section 2.3 [7]. Due to the nanoscale particle size and large specific surface area, NPs can be dissolved more rapidly than the equivalent bulk material, leading to a higher antibacterial efficacy. However there is comparatively little understanding of ion release from metallic particles in aqueous environments, especially multimetal particles.

2.5.1 Metal Ion Release Mechanisms from NPs

There are several factors affecting the ability of NPs to release ions into water. Dissolution is one critical process that determines NPs ion release. This depends greatly on the properties of aqueous environment including pH, ionic strength, dissolved oxygen and dissolved carbon dioxide (Fig.2.14) [117]. For highly reactive metal NPs, oxidation involving dissolved O_2 and CO_2 could accelerate reactive dissolution of NPs. Oxidation layers are commonly found on Cu NPs [118] .Compared to pure Cu NPs, the CuO NPs show a slightly higher ion releasing rate, since the first step for Cu NPs is to release ion into deionized water is through forming oxidation, and then the oxidized Cu would gradually form $Cu(OH)_2$ and release Cu ions into the aqueous environment [119].

The resultant of release metal ions can form metal complexes in aqueous environments. For example, three forms of silver can coexist in Ag NPs colloids stabilized with gelatin and gum arabic: Ag(0) NPs, free Ag^+ ions including any soluble complexes and surface-absorbed Ag^+ [116].

Dissolution rate also greatly depends on particle size. For example, the size of Ag NPs affects the ion releasing rate [120]. Zhang et al compared ion release from 20, 40, 80 nm citrate coated Ag NP over 10 days when the total Ag concentrations were kept at 0.6 mg/L. The smaller size Ag NPs led to higher ion releasing rate due to the higher surface energy [120]. The release for each case became stable after about 10 days. They also reported

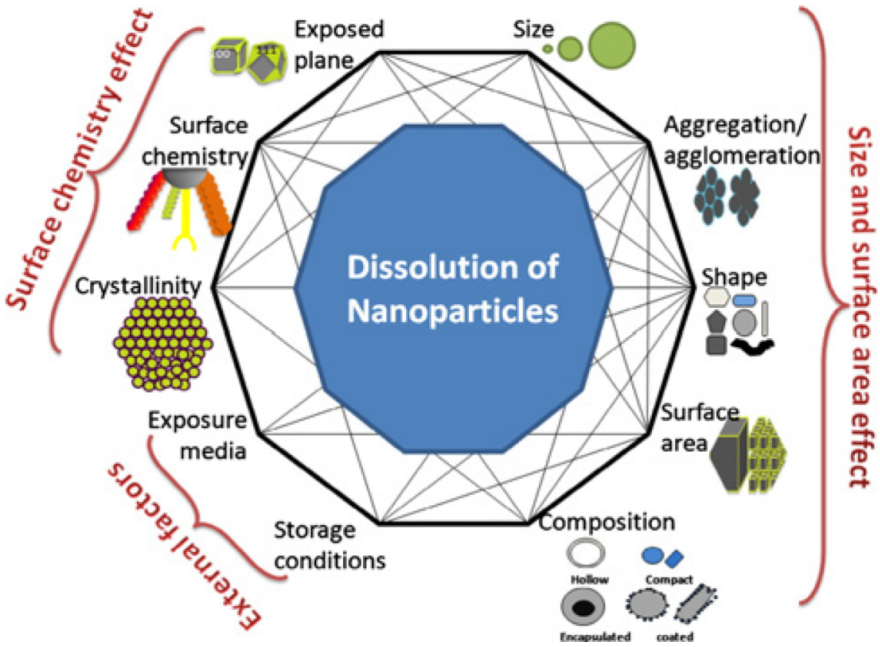

Figure 2.14: Various physicochemical factors affecting dissolution of nanoparticles [12]

that as the Ag NPs concentration reached above 0.6 mg/L, aggregation of Ag NPs would occur rapidly and slow down the oxidation reaction [120].

Larger particles tend to form aggregates over time and eventually sediment. Aggregation and sedimentation can slow down the release rate due to the decrease of the specific surface area. Size effects have also been for CuNPs. 50 nm Cu NPs were found to have higher toxicity in physiological solutions (saline) than larger size Cu NPs (100 nm) since the smaller Cu NPs can release more Cu ions in the same period of time [121].

2.5.2 Analysis of NPs Release Kinetics

Metal NPs dissolution caused by reacting metallic silver with dissolved oxygen is a main ion release process for Ag NPs [116]. Liu et al explained that the Ag ion release can be expressed as a first-order equation in 2.7, where k is the first-order rate constant.

$$-(dm)/(dt) = k * m \tag{2.7}$$

Cu NPs are generally not stable in water. Cu NPs are oxidized rapidly forming Cu^{+} and Cu^{2+} complexes (carbonate/hydroxide forms) and eventually CuO [122]. Moreover, during the incubation in culture media, the rates of Cu ions release can increase with the increased incubation temperature. The dissolution rate of Cu NPs increased very fast in the first 24 h, with a slight increase over the following 72 h [123]. The release of Cu ions from Cu NPs has also been described using first-order kinetics shown in equation 2.8 over a period of 24 hours [124, 125]. This equation was originally used for fitting the silver ion release in Kittler et als research [125], but also fitted for the release of Cu^{2+} from Cu NPs.

$$Y(t) = Y(final)(1 - exp(-kt)) \tag{2.8}$$

where Y(t), is the amount of copper released at time t, Y(final) is the final concentration of copper released [124]. The capping agent is one of the parameters influencing ion release from Ag NPs [126]. Commercial Ag NPs products are usually coated with organic compounds to promote their dispersion, including citrate, cysteine, polyethylene glycol or starch. The capping agents over Ag NPs were found to affect the dissolution rate of Ag NPs [125]. Kittler et al observed that the rate of dissolution and the final degree of dissolution were higher for PVP-stabilized nanoparticles than for citrate-stabilized nanoparticles. It is suspected that the released Ag ions could be reduced by the citrate coating [125].

Cu/Ag bimetallic NPs antibacterial effects have been studied and researches have proved that Cu-Ag NPs have enhanced antibacterial effects against E.coli compared to pure Ag NPs [127]. However, the galvanic effects in mixture of Cu and Ag NPs and the ionization effects in aqueous environment have not been reported for this system. This would be expected when both metallic species are exposed to an aqueous environment at the same time. In the case of Ag-Cu bimetallic NPs would expect enhanced oxidation of copper and suppression of the oxidation of silver which would be expected to be more cathodic. However, galvanic effects have been found between embedded Ag NPs and a Ti substrate [128]. Ag NPs have a positive electrical potential (E(Ag)= 0.7996 eV) while Ti substrate has a negative potential value [129]. The difference of electrical potential drove the galvanic corrosion of the Ti cathode. Ti ions were released into the solution while no measurable Ag leaching was

observed even over 60 days [128]. In this research, Ag/Cu bimetallic nanoparticle ion release was studied for the first time.

2.6 NANOPARTICLE SINTERING AND ELECTRICAL PROPERTIES

Once nanoparticles have been deposited on a surface they must be fixed in position. This can be done by controlling the surface charge on the nanoparticles and the substrate to promote chemisorption [130]. Alternatively, the particles can be sintered to the substrate by post deposition sintering which must be controlled to prevent coarsening and oxidation of the nanoparticles. The process of sintering is arguably more flexible than chemisorption and the requirements will now be discussed.

2.6.1 Driving Force of Sintering

The driving force for densification and coarsening (or grain growth) during sintering is the reduction of the surface free energy of powder compacts. For nanoparticles sintering, the driving forces provided by surface curvature are much higher than that of bulk materials leading to higher rates of bonding between the particles at lower temperatures. In some examples, including silver nanoparticles, neck formation can occur at temperatures as low as 150 °C [131]

The surface free energy of the solid-vapor interface is normally greater than surface free energy of the solid-solid interface and so the solid-vapor interfaces tends to be replaced by solid-solid interface when enough thermal energy is provided to overcome the activation barrier for the diffusional processes of sintering at particle contacts.

The two sphere model used for demonstrating initial stage sintering is presented Fig.2.15. Neck growth increases between two touching particles at elevated temperature. The radius of particles (a) is positive and the radius of the neck (r) is negative leading to negative curvature at the neck and larger concentrations of vacancies under surface of the neck. Thus mass is transported toward the surface of the neck from the planar surface of the grain boundary

by vacancy diffusion and vacancies are annihilated at the grain boundary that are assumed to be a perfect sink.

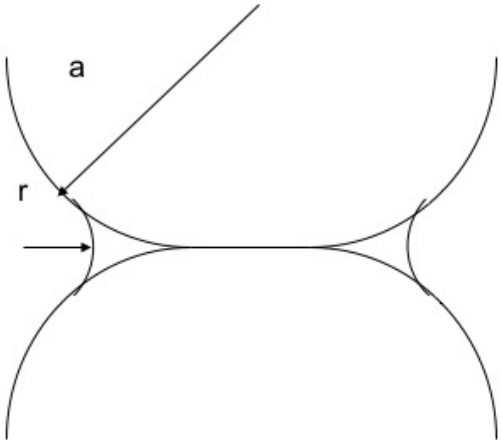

Figure 2.15: Illustration of the two-sphere sintering model geometry. The neck radius is given by r and the particle radius is a.

Mass transport from the grain centers to the concaved surface of the neck can be achieved by several diffusional paths, including grain boundary diffusion and volume diffusion. Conversely, surface diffusion leads to diffusion of atoms from convex particle surfaces to the concaved neck. Therefore surface diffusion is considered to result in coarsening in which the growth of the neck between particles leading to a reduction of the specific surface area of the particles without approach of the particle centers. Volume diffusion and grain boundary diffusion lead to densification, which is defined as neck growth with approach of particle centers. In densification, the grain boundary serves as the source of atoms for diffusional transport, and the neck as the sink or repository for atoms. Both densification and coarsening can lead to the formation of necks. Densification leads to center-to-center approach and shrinkage that eliminates pores. The two sphere model can only be used to explain microstructural changes before adjacent necks come into contact to form grain edges. Therefore idealized microstructural stages are invoked to describe the process of sintering.

2.6.2 Sintering Stages

The process of sintering is divided into three stages, the initial, intermediate, and final stages illustrated in Fig.2.16 In initial stage of sintering Fig.2.16(a), the contact points between particles flatten forming necks without significant densification shrinkage. Initial stage ends with the completion of 10 % densification and the impingement of adjacent necks, Fig 2.16(b).

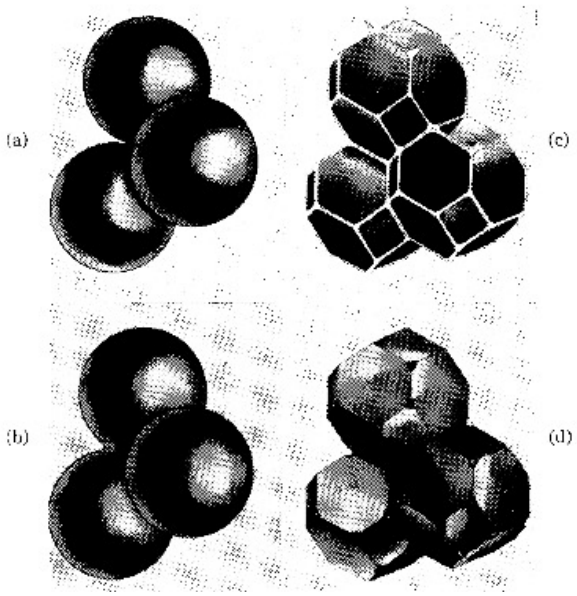

Figure 2.16: (a) Initial stage of sintering; model structure represented by spheres in tangential contact. (b) Near end of initial stage. Spheres have begun to coalesce. The neck growth illustrated is for center-center shrinkage of 4%. (c) Intermediate stage; dark grain has adopted shape of tetrakaidecahedron, enclosing white pore channels at grain edges. (d) Final stage; pores are tetrahedral inclusions at corners where four tetrakaidecahedra meet. [13]

The initial stage of sintering can be achieved in a very short period of time due to the large driving force. The intermediate stage of sintering, is represented in Fig.2.16(c). In this stage, interconnected porous channels are formed along grain edges. The particle assembly shrinks, densifies and coarsening can occur by grain growth. This microstructural representation is used in the modeling of sintering up to a solid volume fraction of 0.92 when pores channels pinch off to form isolated pores. Coarsening and grain growth can also reduce the

surface energy of the system and decreases the driving force. In the final stage, pores become isolated and the solid volume fraction of materials exceeds about 0.92, further densification occurs by shrinkage and elimination of the isolated porosity. In this stage many grain boundaries no longer have pores and grain growth begins to accelerate and increase the diffusion length for further densification. Therefore the densification rate decreases strongly in final stage sintering and remnant porosity is common [132].

2.6.3 Sintering and Electrical Conductivity

Low temperature sintering of non-toxic metal particles such as Ag NPs and Cu NPs have been applied as solder metals and conductive adhesive to replace the traditional Pd based solders for electrical assembly [133,134]. Also as the field of organic electronics has seen tremendous progress over the last years, printed metal electrodes are required for organic files-effect transistor (OFET). It is possible that these electrodes could be printed using nanoparticles and sintered at low temperatures that does not degrade the organic transistors [135,136].

Some physical properties including conductivity, are controlled by the sintering process. Conductivity changes caused by sintering have been related to neck growth. As the neck growth in the first stage of sintering, the conductivity increases without dramatic shrinkage [137]. When the microstructure enters intermediate stage sintering, neck coalesce and grains growth begins and. shrinkage of the films becomes more obvious. If the particles are bonded to a rigid substrate the sintering shrinkage can cause crack formation and the film begins to break up by differential sintering, in response the electrical conductivity decreases [138]. The stress between the film and substrate generated due to coalescence of grain boundaries is reciprocal to the thickness of the film [139]. Therefore, differential sintering and crack formation occurs more easily on thinner films than thicker ones under the same sintering conditions.

2.6.4 Ag and Cu NPs Sintering

Conventional Ag powders are reported to sinter between 700 to 800 °C in air and argon atmosphere. In initial stage, the surface and grain boundary diffusion greatly contributes

to the neck growth [140]. Ag NPs exhibit a much lower sintering temperature than the T_m (961.78 °C) of bulk Ag. Ag NPs (20 nm) are reported can be sintered at as low as 150 °C in the ambient air. It has been reported that Ag NPs can be sintered within the range of 150 to 250 °C on hotplates causing the density and electrical conductivity of Ag films to dramatically increase because of neck growth in the initial stage sintering and the density of powder compacts can reach a solid volume fraction (relative density) of over 75%. Coalescence of the nano Ag particles was observed by sintering at 150 °C [131]. This is very similar to the morphology of an initial stage in the typical sintering process in conventional powder at higher temperature. The reduction in sintering temperature in smaller Ag NPs is attributed to the size effect since the surface driven force is greatly increased as the size of particle decreases.

Sintering of silver nanoparticles combined with patterning techniques such as inject printing could allow new alternative methods for complex circuits designs on flexible substrates [141,142]. The printed nanoparticle film after sintering can form interconnects at low temperature and has been applied to the fabrication of metal-polymer composites with high electrical conductivity [131]. It has been reported that sintered thin films can exhibit high conductivity as well as high cost-efficiency [143].

Conventional Cu powders are in size range 45 to 75 μm and are normally sintered in the temperature range 750 to 1000 °C, which is still lower than its melting temperature 1,085 °C [144]. The sintering time to reach to fully densification depends on the sintering time [144].

Cu NPs are a potential alternative to noble metals interconnects [145]. Cu has a high electrical conductivity and low-cost. However, to achieve this alternative material selection it will be necessary to sinter copper nanoparticles at relatively low temperature compared to those temperatures required for sintering of conventional copper powders. The melting temperature for bulk Cu is 1,085 °C, which is much higher than the sintering temperature of Cu NPs. It has been reported that 65 nm Cu NPs have shown a low bonding temperature of 250 °C due to the formation of necks at particle contacts under reducing atmosphere [21]. The sintering was performed in a furnace under flowing nitrogen (N_2) at 250 °C for 80 min. After sintering, a printed the Cu pattern was finally obtained with electrical conductance [142].

With smaller size, Cu NPs (10 nm) necking was achieved at 150 °C and showed an impressive electrical resistivity of 25.5±8.0 $\mu\Omega$·cm [146].

Capping agents in the NPs ink act as insulating layer between particles [147–149]. It is therefore important to use the lowest sintering temperature above the decomposition temperature of the capping agents. Usually shorter chain capping agents have lower decomposition temperature. Cu NPs coated with short chain carboxylic acid have lower resistivity than that coated with longer chain capping agents when both were sintered at the same temperature (200 °C to 250 °C) [146]. Additionally copper nanoparticles have to be protected from oxidation, even at temperatures at low as 200 °C [150]. This is usually done with a nitrogen atmosphere [142, 146].

2.6.5 Ag Shell Cu Core NPs

Given the enhanced sintering ability and oxidation resistance of silver nanoparticles and the potential for low cost copper nanoparticles it is logical to suggest that Ag shell-Cu core nanoparticles would be desirable for electrical interconnect made from deposited nanoparticles. Ag NPs can be sintered at lower temperature than that of Cu NPs and the silver shell would lead to sintering controlled by neck formation at Ag-Ag contacts. In addition the copper would be protected from the ambient environment if the silver shells are complete so it is expected that such particles could be sintered in air.

There are only a few reports discussing the sintering behavior of Ag shell Cu core NPs in recent in the literature. Cu-Ag core shell NPs were synthesized by galvanic displacement [151] where Ag shell was formed by oxidizing the surface Cu components over Cu NPs synthesized in the first step. Lee et al [151] compared the resistivity of Cu-Ag core shell NP films (13.5 nm) with that of films made of Cu NPs. The results shown that bimetallic NPs films have superior conductivity after sintering at 350 °C in N_2 gas. However, the smaller size of alloy NPs would have high potential for oxidation when exposed to air.Moon et al compared the sintering behavior of mixed Ag,Cu NPs and Cu NPs [21]. The mixture of Cu NPs (65 nm) and smaller Ag NPs (21 nm) were mixed at a molar ratio of 3:1 and predicted to reach the maximum packing density in the bimodal particle system [21]. The mixed

particle films were sintered at 175 °C and showed a high conductivity compared to that of films made with the pure Cu NPs (65 nm) which only became conductive after sintering at 225 °C. Interestingly, there is a report that bimetallic Ag-Cu NPs have better sintering behavior and higher electrical conductivity than that of the same ratio of mixture of Ag and Cu NPs [21, 151]

This inspired one objective of the present research in which the sintering behavior and electrical conductivity of Ag, Cu, Ag and Cu mixture, and Cu@Ag core shell structure were compared under the same sequential annealing temperatures and environment (N_2).

3.0 HYPOTHESIS

Two steps of nanoparticle synthesis methods can be developed to assist in the full reduction of both copper and silver in the preparation of core-shell Ag-Cu nanoparticles with copper shells and silver shells.

This hypothesis will be investigated in following chapters, in which sub-hypotheses are listed below:

1) Microwave radiation will enhance the reduction of Cu in the synthesis of Ag-Cu bimetallic nanoparticles.

2) Ag-Cu shell core nanoparticles have superior sintering behavior can be sintered at lower temperature than the mixture of Ag and Cu NPs.

3) Bimetallic nanoparticle may not release both Ag and Cu ions into aqueous solution due to galvanic effect.

4) The mixture of Ag and Cu nanoparticles can exhibit better antibacterial effect against silver resistant bacteria and wild type in the planktonic state than pure metal nanoparticles.

4.0 OBJECTIVES

The objectives of this research are:

1) To examine the effect of microwave heating compared to oil bath heating on one-pot and two-pot synthesis of Ag-Cu bimetallic nanoparticles.

2) To study sintering behavior of bimetallic NPs and show that Ag-Cu bimetallic core-shell NPs have better sintering and electrical conductivity than that of the similar molar ratio mixed Ag and Cu NPs because of the increased fraction of Ag-Ag necks formed at particle contacts.

3) To monitor the ion releasing rate of nanoparticles into aqueous solution and compare with mixtures of nanoparticles

4) To examine the efficacy of silver and copper antibacterial nanoparticles against mycobacteria.

5.0 METHOD AND MATERIAL

5.1 SYNTHESIS OF NANOPARTICLES

5.1.1 Synthesis of Ag NPs

Silver nanoparticle have been synthesized using a chemical reduction method. Silver nitrite ($AgNO_3$, Sigma-Aldrich company) was reduced in aqueous solution with sodium borohydride ($NaBH_4$, Sigma-Aldrich company), as shown in equation 1, in the presence of polyvinyl pyrrolidone (PVP, Sigma-Aldrich company). $AgNO_3$ and PVP with a weight ratio 1: 1 were dissolved in deionized water. By adding $NaBH_4$ solution dropwise, metallic silver particles were synthesized at 50 °C with vigorous stirring. After 10 to 15 minutes, the silver colloidal solution were centrifuged at 7900 rpm for 15 minutes [152]. A deposited sediment of large aggregates was then removed and the upper layer of the solution was centrifuged for another 15 minutes. Excess PVP in the solution was dissolved by diluting the solution with 5 times the volume of acetone. The AgNPs were then finally dispersed in deionized water for future use. The yellowish suspension was stored for one month without changing color or any obvious sediment. Several techniques including TEM and EDS were applied to characterize the Ag NPs.

5.1.2 Synthesis of Cu NPs

In the synthesis of copper nanoparticle [14], ascorbic acid was used as a reducing agent as well as capping agent. Ascorbic acid, also called vitamin C, is an essential nutrient for humans. Its environmentally friendly compared with other chemical reducing agent, like $NaBH_4$. Therefore, there is less concern regarding the excessive reducing agent in this syn-

thesis. L-ascorbic acid is a highly soluble compound with strong polarity within which the electrons in the double bond, hydroxyl group long pair and the lactone ring carbonyl double bond form a conjugated system. Such structure enables ascorbic acid to reduce Cu^{2+} into Cu(0). The redox equations are demonstrated in Scheme 2 of Fig.5.1.

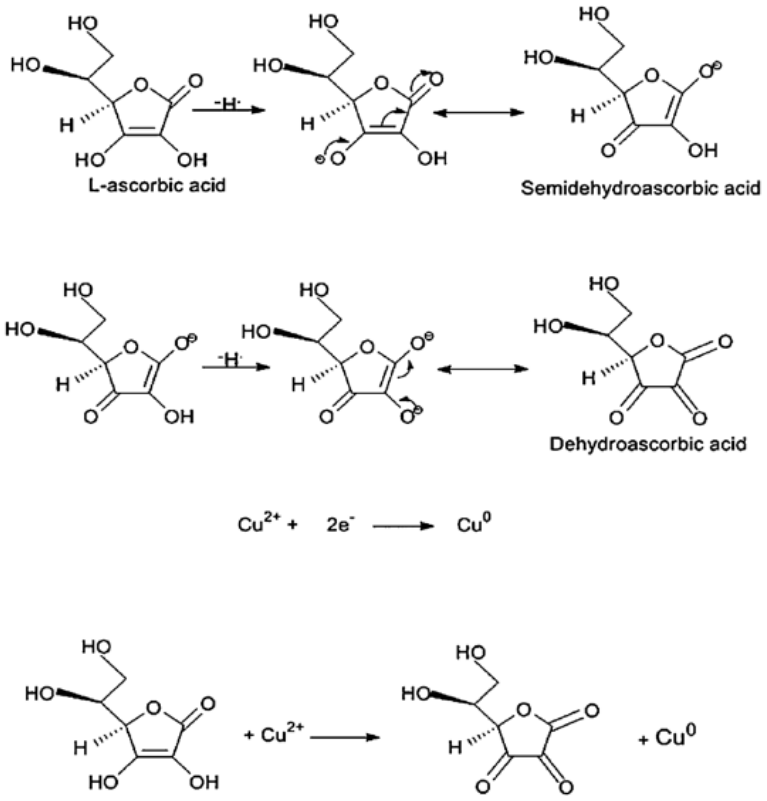

Figure 5.1: Scheme of the reduction reaction equations for the formation of Cu Nanoparticles [14].

Copper acetate solution is mixed with excess ascorbic acid and reacted for 10 hours at 80 °C. The molar ratio of Cu (II) acetate to ascorbic acid was 0.5. After adding the reducing agent, the mixture turned brown and gradually became red after 10 hours. Assuming all the copper ions are reacted with ascorbic acid, the concentration of the copper nanoparticle was calculated to be 0.1 mol/L. The suspension of Cu NPs can be stored for over a month without evidence of sedimentation.

5.2 SYNTHESIS OF BIMETALLIC NANOPARTICLES

5.2.1 One Step Synthesis for Silver Core Copper Shell NPs

Copper (II) formate tetrahydrate ($(HCO_2)_2Cu_4H_2O$, 98%, Alfa Aesar) and silver nitrate (Sigma-Aldrich) were dissolved in ethylene glycol (EG, 99.8%, Sigma-Aldrich) with a molar ratio of 1:1 and 1:3. Polyvinylpyrrolidone (PVP, MW 55,000) capping agent was also dissolved in the EG at a concentration of 0.1g/ml. In the final mixture with molar ratio of 1, the Cu (II) concentration was 20 mM/L and concentration of Ag (I) was 20 mM/L. In the solution with molar ratio of 3, Cu (II) concentration is 40.3mM/L and Ag(I) is 13.4 mM/L. Heating the mixture solution to 175 °C over a period of 20 minutes and dwelling for 1 to 5 minutes in a microwave reactor caused the initially blue solution to turn red. The oil bath heating profile also included a 20 minute ramp to 175°C and a dwell time ranging from 1 to 5 minutes to be as close as possible to the nominal conditions used in the microwave reactor. After the synthesis, the samples were immediately quenched in an ice bath. The resultant particle suspensions were centrifuged at 7900 rpm for 15 minutes, after which the nanoparticles were collected and redispersed in ethanol. Nanoparticles are stored in vacuum container for further characterization.

5.2.2 Two Steps Synthesis for Ag and Cu Bimetallic NPs

Copper(II) precursor and Ag (I) precursor were prepared in the same process as described in section 5.2.1. After the precursors were prepared, the prepration sequence for Ag core-Cu shell and Cu core-Ag shell NPs are introduced in the following sections.

5.2.2.1 Ag core-Cu shell (Ag@Cu) NPs preparation Silver seed precursor was prepared by heating silver nitrate EG solution in oil bath at 120 °C for 2 to 5 minutes. The Ag(I) EG solution turned yellowish indicating the Ag seeds wereare nucleated. The Ag seed precursor was cooled down to room temperature before mixing with Cu(II) EG solution. To synthesis Ag@Cu NPs, the silver seed precursor and Cu (II) EG solution mixture were placed into the MW reactor. The second reaction step was similar to one pot synthesis.

The temperature in the MW program was set to 175 °C with a 20 minute ramp from room temperature and 5 minutes holding time. After the synthesis, the samples were immediately quenched in an ice bath.

5.2.2.2 Two steps synthesis for silver shell copper core NPs Cu (II) EG precursor was heated in the MW at 175 °C for 1 minutes. The bluish solution turned reddish indicating Cu ions were reduced to Cu NPs. The seeded precursor was transported immediately to an oil bath preheated to 175 °C under N_2 gas. Cu@Ag NPs were then synthesized in the second step by adding AgNO3 EG solution drop wise. After 5 minute reaction, the color of NPs liquid turned to light pink.

5.3 CHARACTERIZATION OF NANOPARTICLES

5.3.1 TEM

A small drop of silver nanofluid (2.2 g/l) was placed on a copper grid with graphene supported by lacey carbon (Ted Pella NO:01895) and allowed to dry thoroughly. The sample was then imaged by TEM (JEOL200CX) in bright field. Images were analyzed in Image J to measure particle size.

For Ag-Cu bimetallic nanoparticles samples aAfter the synthesis, the samples were immediately quenched in an ice bath. The resultant particle suspensions were centrifuged at 7900 rpm for 15 minutes, after which the nanoparticles were collected and redispersed in ethanol. 2 μL samples of the nanoparticle suspensions were dropped on a gold TEM grid with carbon film (Ted Pella Co.). The grids were dried overnight in a fume hood and kept in a vacuum container before examining with TEM and EDS (FEI Tecnai G2 F20) to study the composition and nanostructures of the particles. The sizes of NPs were also measured. EDS spot size was about 3 nm. EDS spots were taken from a peripheral, center and another peripheral regions on the representative Ag core Cu shell particles. Ag/Cu atomic ratio from each spots and the whole particle were analyzed. From the Ag/Cu atomic ratio difference in

the particle can evaluate the core shell structure. For imaging Ag shell Cu core NPs, TEM (JEOL, JEM-2100F, 200kV) equipped with STEM-EDS was applied to achieve Ag and Cu element EDS mapping. This model of TEM has a probe size under 0.5 nm to achieve the high image quality. All the images were taken under bright field. Ten particles were chosen for STEM-EDS mapping.

5.3.2 XRD

The phase identity and crystallite size were analyzed by X-ray diffraction. The average size of nanoparticles was also evaluated by XRD. The equation named after Paul Scherrer, relates the average size of nanoparticles to the broadening of a diffraction peak. In Scherrer equation 5.1.

$$\tau = \frac{K\lambda}{\beta \cos\theta} \tag{5.1}$$

where τ is average size of the nanoparticle; K is a dimensionless shape factor, with a value close to unity. The shape factor has a typical value of about 0.9, but varies with the actual shape of the crystallite; λ is the X-ray wavelength; β, the broadening of the peak at scattering angle; θ, is measured at half of the maximum intensity in radians.

Metal nanoparticles crystal phases were analyzed with X-ray diffraction (Empyrean series 2, PANalytical) using a Cobalt target source with iron filter to give cobalt alpha radiation. Colloidal NPs were freeze-dried in vacuum for one day until they were dried enough to be lightly granulated for XRD analysis. Two sets of characteristic peaks were detected from the bimetallic NPs. The full reduction of Cu component in Ag core Cu shell NPs can be confirmed with XRD phase ratio analysis.

5.3.3 Dynamic Light Scattering

Dynamic light scattering (DLS) measurements were used to measure particle sizes of aqueous NPs samples. Number based distributions were selected to characterize the NPs sizes so that it would be consistent with TEM analysis.

Small particles in suspension undergo random thermal motion known as Brownian motion. This random motion is modeled by the Stokes-Einstein equation 5.2. Below the

equation 5.2 is given in the form most often used for particle size analysis [153].Where D_h is the hydrodynamic diameter, D_t is the translational diffusion coefficient, k_b is Boltzmanns constant, T is thermodynamic temperature, η is dynamic viscosity. This function reminded us that the particle size determined by dynamic light scattering was hydrodynamic size. The nanoparticles were coated and separated with PVP which was a hydrophilic polymer. It would explain that the particle size measured by DLS was larger than the size measured by TEM or SEM.

$$D_h = \frac{K_b T}{3\pi\eta D_t} \tag{5.2}$$

5.3.4 XPS

X-ray photoelectron spectrometer (Escalab 250Xi XPS Microprobe) was applied to characterize the elemental composition of Ag-Cu alloy NPs. XPS is a surface-sensitive quantitative spectroscopic technique that measures the binding energy and number of electrons escaping upon irradiating the sample with X-ray. The XPS spectra gives us information on the chemical state and elements that close to the surface of the nanoparticles. Also, combining a sputtering function of the ion gun adjacent to XPS, an oxidation layer of the nanoparticle can be etched away. The possible CuO layer of the alloy nanoparticle could be detected by XPS. Then, the ion gun will be applied to remove the oxidation layer and the alloy nanoparticle can be analyzed by XPS. Through depth profile etching technique, the composition of the film was determined as a function of depth from the surface to certain thickness.

5.3.5 Light Absorption of Fluids

The optical properties of very dilute aqueous nanoparticle fluids were measured using Lambda 35 UV/VIS spectrometer (Perkin Elmer). Characteristic absorption peaks from Ag and Cu nanoparticles can be detected from Ag, Cu and the mixture of Ag and Cu NPs. The bimetallic NPs absorption spectrum shown an enhanced and merged characteristic peaks from both Ag and Cu components.

In addition to experimental measurement of the optical properties, the absorption spectra of the NPs were simulated using a finite-difference time domain (FDTD) numerical analysis

of the electrodynamics to find approximate solution to the Maxwell equations by expanding the field on a regular tensorial grid. In this study, an idealized core-shell volume ratio was calculated using the molar ratio of Ag/Cu from the synthesis and the experimentally measured particle sizes to determine an estimated core/shell thickness. In the simulation, the Ag core size was fixed at 100 nm and the Cu shell thickness was in the range from 3 nm to 15 nm. The simulated adsorption spectra range was set from 300 to 800 nm, which was the same condition used in the experimental measurement.

5.4 ANTIMYCOBACTERIAL EFFICACY OF MULTIMETAL NANOPARTICLES

5.4.1 Susceptibility of Planktonic Mycobacteria to NPs

The bacteria investigated here are M.smegmatis wild type (MC^2155) and silver resistant mutant ($Agr-1$). M. smegmatis was grown in Difco Middlebrook 7H9 broth containing 10% Albumin-Dextrose and 0.05% Tween-80 at 37 °C placed on a shaking table for 48 hours. M.smegmatis were then stored in a freezer at -80°C. Cu NPs were synthesized in the presence of ascorbic acid in the water. The particle size is around 15±5.7 nm. Stock solutions of Cu NPs were prepared and subsequently added to 2 mL 7H10-ADC media to achieve concentrations of 1, 3 and 5 mM. Each concentration of copper enriched media was inoculated with M. smegmatis from a saturated culture (106 CFU/ml). Samples were incubated on a shaker at 37 °C for 48 hours. Samples (10μL) were then plated to count CFU [154].

To measure the CFUs a 100 μL sample of M.smegmatis wild type or Agr-1 were added to 900μL of PBS buffer solution. This culture was subsequently diluted in the same media in a ten-fold dilution series. Three 10μL samples from each tube in the series of dilutions were added to an agar plate with 7H10-ADC growth medium. After incubation at 37 °C for 72 hours bacterial colonies are visible. For the less dilute spots the colonies merge into a large mass of bacteria and cannot be counted. When dilute enough separate colonies can be

counted. CFU is then calculated multiplying the number of separate colonies by the dilution factor of the spot as shown in equation 5.3.

$$CFU = (counted\,colonies) \times (dilution\,factors) \tag{5.3}$$

Plates were photographed to facilitate counting colonies. The experiments were carried out in triplicate and averaged. Growth in the presence of NPs was expressed by calculating survival percentage according to equation 5.4.

$$\%Survival = \frac{experimental\,CFU}{inoculating\,CFU} \times 100 \tag{5.4}$$

Such that a percentage over 100% indicates growth over the number of inoculating bacteria. When cultured without silver or copper or any other toxin bacteria can grow by upwards of 100,000% in 48 hours. Any survival percentage below the growth in the control indicates growth inhibition [154]. When the survival percentage decreases below 100% this is indicative of bacterial killing. Survival percentages were compared for MC^2155 and Ag-r1 to establish whether Ag-r1 can in fact resist the toxic effect of silver and copper more than the wild type.

During the plating, ten-fold dilutions from each sample were grown on 7H10 agar plates and incubated until individual CFUs could be counted. Middlebrook 7H10 nutrient agar (BD, USA) were melted on a hot plate and cooled down to 55°C. 10% albumin dextrose catalase was added in Middlebrook 7H10 nutrient agar (BD, USA) and the agar was dried in a petri dish. M.smegmatis MC2 155 and Agr-1 were grown in the petri dishes containing Difco Middlebrook 7H10 agar containing 10% Albumin-Dextrose at 37°C. The experiments were carried out in triplicate.

Similar experiments were performed on planktonic mycobacteria exposed to AgNPs (∼20 nm). Stock solutions of AgNP were prepared and were subsequently added to 7H10-ADC media to achieve concentrations of 6.25, 12.5, 25, 50, and 100 μM. Stocks of silver resistant mutants and wild type were both diluted to 106 CFU/ml and separately added to half of the tubes containing the culture media. After culturing for 48 hours ten times dilutions were prepared for both the wild type and the silver resistant mutants, 10 μL of each diluted sample was plated on agar plates and incubated until CFUs could be counted.Percent survival was calculated by dividing the CFUs counted from each concentration by the CFU from the

inoculating volume. Values over 100% indicate bacterial growth while below 100% indicates a reduction from the initial bacterial load.

5.4.2 Comparison of Ag-r1 and MC2 155 Response to Silver Exposure and Copper Exposure in Planktonic State

Ag-r1 bacteria were exposed to Ag NPs alongside the unmodified wild type MC^2155 strain to determine if the strains is mutated to confer resistance to silver. Stock cultures of both MC^2155 and Ag-r1 were grown in 7H9 growth media on a shaking table until the optical density was 0.3 to 0.5 as measured on a spectrophotomer (Jenway 6320D), which is around 107 cells/ml.

Stock solutions of Ag NPs(∼20 nm) were prepared and subsequently added to 7H10-ADC media to achieve concentrations of 6.25, 12.5, 25, 50, and 100 μM. In addition, Cu NPs solutions were added to the same media giving concentrations of 0,1, 10, 25,50, 100 times relative to the silver concentrations. The compositions of the mixtures of Ag NPs (∼20 nm) and Cu NPs(∼10 nm) are listed in table 5.1. A positive control condition was set by adding Ag NPs in the media without Cu NPs and a negative control condition was prepared with just 7H10-ADC. For each concentration of the mixtures of Ag NPs and CuNPs a sample was placed in a 15ml sterile test tube in triplicate. From a saturated culture, 10 μl (∼106 CFU/ml) of MC^2155 was added to half of the tubes while the other half was inoculated with an equal volume of Ag-r1. The samples were incubated on a shaker at 37 °C for 48 hours. After the incubation period the growth of bacteria was observed by comparing the optical density for all the samples and the number of colony forming units per milliliter (CFU/ml) to the CFU in the inoculating load.

Optical density was measured on a spectrophotomer (Jenway 6320D) at wavelength 600 nm. When optical density is less than 0.4 absorbance units (AU) it correlates to the cell density in the culture. Samples that had OD greater than 0.4 AU were diluted in a sterile medium that was prepared and incubated along with the experimental cultures. Background OD of bacterial cultures was removed by calibrating the spectrophotometer against a sterile control medium that was prepared alongside the bacterial culture. When dilution was nec-

essary to measure OD the background sample was likewise diluted. OD was measured at the inoculation time and at 48 hours culturing. The OD for MC ^{2}155 and Ag-r1 were plotted against particle concentration (μM). Table 5.1 shows the mixtures concentrations.

Table 5.1: Concentrations of metal nanoparticles for planktonic experiments

Conditions (uM)	1	2	3	4	5
Ag/Cu(1/0)	6.25	12.5	25	50	100
Ag/Cu(1/1)	6.25/6.25	12.5/12.5	25/25	50/50	100/100
Ag/Cu(1/10)	6.25/62.5	12.5/125	25/250	50/500	100/1000
Ag/Cu(1/25)	6.25/156.25	12.5/312.5	25/625	50/1250	100/2500
Ag/Cu(1/50)	6.25/312.5	12.5/625	25/1250	50/2500	100/5000
Ag/Cu(1/100)	6.25/625	12.5/1250	25/2500	50/5000	100/10000

5.5 INKJET PRINTING OF NANOPARTICLE FILMES

5.5.1 Inkjet Printing Deposition of Nanoparticles

A piezoelectric inkjet printing system (Microfab company) in Fig.5.2 was used for the research on nanoparticle deposition. The piezoelectric print head with an (MicroFab MJ-AL-01-60, Plano, Texas) allows for drop-on-demand inkjet printing; whereas, the CCD camera and the strobe light are used for visualization of the drop during flight in order to determine drop stability. The substrates were attached to a programmable xy stage, which allowed for the substrate to translate while the printing nozzle remained fixed. It consists of a high resolution (0.5 μm/pixel) Sensi-Cam QE charged coupled device (CCD) camera (Romulus, Michigan) and a Navitar 12 zoom lens (Rochester, New York), synchronized with a halogen strobe light and the drop ejection to form a high magnification goniometer for side-view observation.

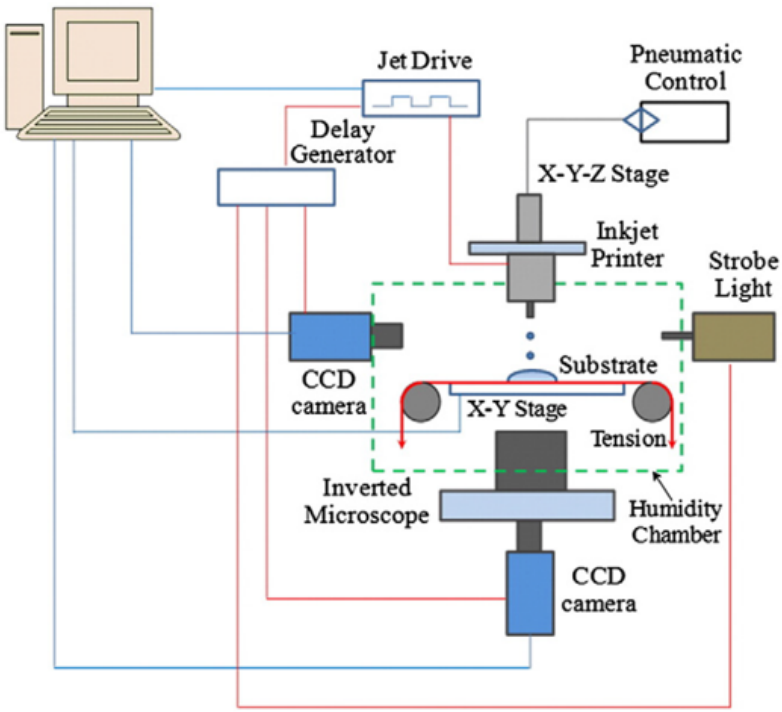

Figure 5.2: Schematic image of a inkjet printing system(microfab)

All inkjet printing experiments were conducted at normal ambient room conditions (i.e. 24°C, atmospheric pressure, and 30% relative humidity with a printing frequency of 500 Hz. A series of hexagonal coordinates of printing spot were designed to meet the requirement of equal distant adjacent NP spots in the pattern. The drop center to center distances are varied from 200μm to 1200μm. The printing system was also programed to print accumulated drops on each spot. A single drop (350 to 400 pL volume size) can be as small as 30 $\sim$ 50μm when dried on to a silicon wafer substrate. As the printing drop numbers increase, the spot diameter can be increased. In this research, drop sizes are designed from 200μm to 1000μm to achieve a series of surface coverage of NPs and optimize the printed volume of NPs suspension.

5.5.2 Preparation of Nanofluids

Each nanofluid was sonicated in an ultrasonic mixer for 10 minutes otherwise, aggregates may occur due to the increase in temperature induced by evaporation. An ice bath was used to help cool down the suspension when necessary.

Both AgNPs and CuNPs nanofluids were relatively stable. They did not aggregate and precipitate within a month. The particles are small enough that they can be maintained in dispersion indefinitely, indeed the small particle size and the low concentration of the nanofluids used in this research resulted in no visible aggregation after several months. At higher concentrations, the dispersion began to turn dark and aggregate after one month.

5.5.3 Deposition Method

The dynamics of droplet formation of liquid in a piezoelectric inkjet printing process relates to driving voltages, dwell times, and back pressures. The inkjet printer head is a piezoelectric device controlled by signal waveforms for DOD (Drop-on-Demond) inkjet printing. A bipolar pulse waveform was applied to the printer head. The workable pulse voltage ranges were also investigated. Between 10 to 25 volts, the droplet were smoothly generated and ejected for aqueous nanoparticle suspensions when the viscosity and surface tension coefficient are relatively low. The range is between 30 to 50 volts for ethylene glycol [15]. Within this workable voltage range, one single droplet for each pulse can be achieved without satellite droplets. High back pressure yielded smaller drop volumes, allowing for possible resolution increases, however at higher back pressures some drops became unstable, producing satellite drops that would affect pattern formation.

Hexagonal arrays were chosen over rectangular arrays because the distance between drops across the diagonal of a rectangle is larger than the distance along the edges, therefore bacteria would grow preferentially in the center of the rectangle. Hexagonal arrays eliminate this issue, as the drops are evenly spaced in all directions. The substrate was polycarbonate membranes (Whatman 7060-1304). Generally, the number of drops applied to a substrate ranged in the tens to hundreds. The area density was controlled by changing the inter-spot spacing in the scripts that control the jetting program.

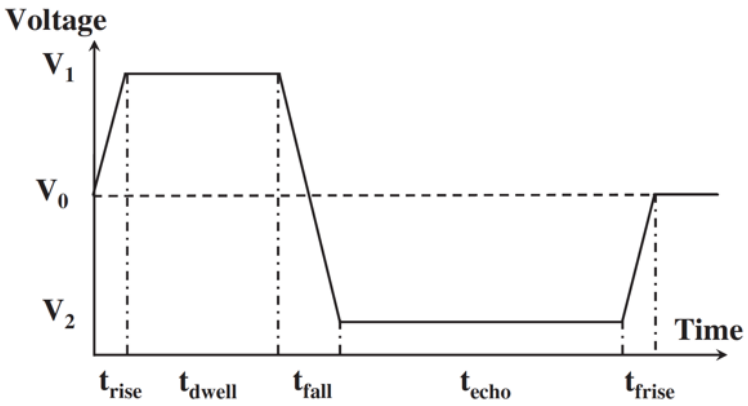

Figure 5.3: A schematic diagram of a typical bipolar pulse waveform [15]

5.5.4 Surface Characterization

Scanning electron microscopy (SEM-JEOL) and digital optical microscope (Keyence VHX-600K) were used to measure the printed spot size and inter spot distance on the membranes.An example of printed membrane is presented in Fig.5.4 Additionally, an optical surface profiler (Veeco/Wyko NT 1100) was applied to measure the over all shape of the spots and characterize spatial distribution of particle deposits in the spot.

The surface coverage of the NPs is an important factor that could affect initial stages of colony formation and inhibit the growth of biofilm. Area coverage of AgNP spots on the membrane surfaces were printed in the range 7.5% to 30 %. The patterned membranes were then inoculated with M.smegmatis (wild type) in the biofilm experiment described in the next section. Imaging and qualitative observation of samples was done using a Keyence digital optical microscope. The samples were then coated with palladium and imaged with SEM. Magnifications from $\times 200$ to $\times 500$ of images were taken to capture the morphological features. The same Ag NPs suspensions were printed using the same scripture on silicon wafers. Spatial morphologies of a printed spot were analyzed by an optical profiler (Veeco/Wyko NT 1100). The volume and size of the dried silver spot could be evaluated by not considering the porous substrate.

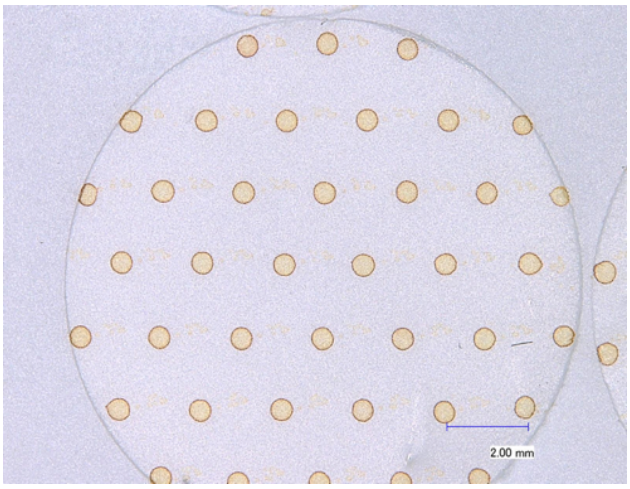

Figure 5.4: Digital microscope image of Ag NPs printed on a membrane

5.5.5 Substrate Wetting Angle

The polycarbonate membranes were autoclaved with standard procedures at 121°C for around 15 to 20 minutes before printing with NP solutions. A hydrophobic substrate was placed under the printing layer in order to change the wettability of the hydrophilic polycarbonate and maintain the drop shape. Contact angle was measured using drop shape analysis (Kruss DSA 100). Contact angles were measured with concentrations of silver nanofluid 1.1g/L and 2.2g/L and copper nanofluid 6.4g/L.

5.6 INHIBITION OF BIOFILM FORMATION BY DEPOSITED NANOPARTICLES

One of the primary goals of this research is to determine the ability of deposited AgNP spots to inhibit biofilm growth. A series of experimental protocols were developed for this purpose.

5.6.1 Surface Protection of Membrane Filters

Nanoparticles were deposited on microporous track etched polycarbonate membranes (Whatman 7060-1304) as previously described. The membranes are 13 mm diameter and have 400 nm pores. Membranes are sterile as purchased and were autoclaved twice before printing and after printing and then stored inside the autoclave bag for biofilm testing. During biofilm testing, membranes were handled and prepared in a sterile hood to prevent environmental contamination. Membranes were printed with Ag NPs suspensions (2.2 or 1.1g/L) using the inkjet printer which allowed the nanofluid to permeate the pores while drying in air. Incorporation of silver nanoparticles was confirmed by SEM (Philips XL-30) and energy dispersive x-ray spectroscopy (EDS).

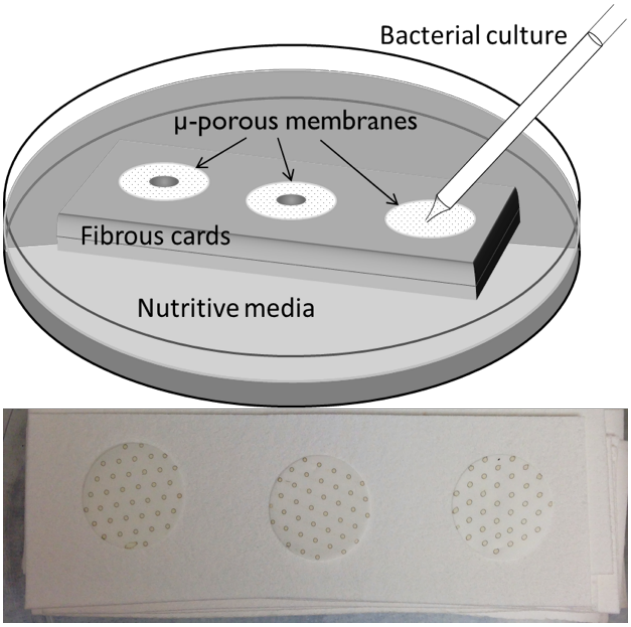

Figure 5.5: Bioreactor of membrane toxicity assay(upper) [16]; printed membranes were placed on fibrous cards(lower).

An assay was developed to culture bacteria on the surface of the membranes. A 15 ml reservoir of nutritive media (7H10-ADC) was added to a petri dish. These sterile fibrous cards were stacked in the media so the topmost card sat above the surface of the media as

depicted in Fig.5.5. Three membranes (either nanoparticle-coated or uncoated) were placed on the card stack in each petri dish. The media, which thoroughly soaked the cards, ensured that the membranes did not become dry and the capillary effect delivered nutrition to bacteria that were inoculated on the surface of the membrane. Approximately 600 μM. smegmatis (10 μL) from a saturated culture were spotted at the center of each membrane. CFUs were counted for the seeded bacteria by plating dilutions from the saturated culture at the same time that the inoculation was performed on the membranes. In these experiments the bacteria are larger than the pores of the polycarbonate membranes so they colonize the surface of the membrane and cannot travel through or colonize in the pores or the media reservoir. A lid was placed over the petri dish and the samples were incubated at 37 °C to allow the mycobacteria to grow.

The membranes and the dishes were then incubated for 24 to 41 hours at 37°C. At the end of incubation the membranes were carefully removed from the cards and fixed in a 5% solution of formaldehyde for 1 hour. The membranes were then removed, dried and prepared for SEM. After being coated with palladium the samples were imaged at a range of magnifications. Most of the imaging was done at 500x so that a large range of colony sizes could be observed.

The images for each sample were processed and analyzed with ImageJ. This software has built in functions to threshold the images to identify bacterial colonies. The Analyze particles function of ImageJ was used to analyze the resulting black and white image to determine the number, size, and morphology of the colonies.

5.7 METAL ION RELEASE FROM NANOPARTICLES

5.7.1 Nanoparticles Suspension Preparation

Ag (∼30 nm), Cu (∼100 nm), Ag core Cu shell (Ag@Cu, ∼120 nm), Cu core Ag shell (Cu@Ag ∼127 nm) and Ag/Cu mixture nanoparticles were suspended in deionized water. Initial Cu NPs aqueous concentration was 85.3 mg/L corresponding to 1.33 mmol. Initial

Ag NPs loading was 46 mg/L corresponding to 0.43 mmol. In the aqueous sample of Ag/Cu mixture NPs, the total loading of Cu and Ag NPs was the same as the total metal loading for pure NPs samples (1.33 mMol Cu NPs and 0.43 mmol Ag NPs). Ag core-Cu shell NPs were synthesized with a Ag/Cu ratio 1:3 and proved to fully reduce for both components in the MW reactor. Therefore, the loading of Ag@Cu NPs was 1.76 mmol which was consistent to the loading for the Ag NP and Cu NP mixtures. For Ag shell-Cu core NPs, due to the re-oxidation of Cu component in the second step of the synthesis, the Ag/Cu phase ratio was 1:2.33 (30/70). This sample loading was 1.45mmol (Cu: 66.24 mg/L and Ag 46 mg/L), which had less Cu component than that of Ag core- Cu shell NPs.

Sterilized plastic tubes (50 ml) were prepared as sample holders, the caps were loosened and left a gap to allow air flow in and out during the measurement period. The samples were stored away from light. Three samples were prepared for each condition and tested with conductive electrode (Thermofisher Orion DuraProbe 4-Electrode Conductivity Cells) and silver ion selective electrode (Cole-Parmer, Silver/Sulfide(Ag^+/S^{2-}) ion selective electrode). The ion release from the nanoparticles was monitored everyday over a week. Several measurements were made at the first day once the sample exposed to air since the freshly made samples were more sensitive.

5.7.2 Ion Selective Electrode Calibration

Silver ion standard solutions were made with $AgNO_3$ in a serial of 0.01, 0,1, 1, 10, 100 ppm. The lowest range of the silver selective electrode was 0.01 ppm. The Ag ion selective electrode was calibrated with the range of 0.01 to 100 ppm. Calibration curve was made daily before each test. A PH/Ion meter (Fisher Scientific accumet AB250 pH/mV/ISE/Temp Meter) was used to record the calibration curve. Total ion concentration was measured by conductive electrode (Thermofisher Orion DuraProbe 4-Electrode Conductivity Cells, 013005 MD). The electrode was by entering the nominal cell constant ($0.475cm^{-1}$) in meter, immersing the conductivity cell in the calibration standard solution (Thermo Orion KCL conductivity standard 0.1 M). When the reading stabilizes, the meter displays the calibration standard value at 25 °C. Once the calibration is accepted, the meter calculates and displays

the actual cell constant. The calibration was performed once a week. The conductivity range is 1μS/cm to 200mS/cm [155]. Total dissolved solid (TDS) unit was parts per million (ppm). Since the electrical conductivity of water is directly related to the concentration of dissolved ionized solids in the water. Ions from the dissolved solids in can be measured using a conventional conductivity meter or TDS meter. The correlation between EC to TDS was set at 0.64 in equation 5.5 [156].

$$TDS(ppm) = 0.64 \times EC(\mu S/cm) \tag{5.5}$$

5.8 SINTERING

5.8.1 Nanoparticle Films Preparation and Sintering

5wt % of NPs ethanol ink were prepared on an 0.5 cm ×0.5 cm glass substrates. The glass substrates were first cleaned with acetone and then ethanol and finally with deionized water in an ultrasonic cleaner. Several layers of NPs were deposited on one substrate until the substrate was opaque by doctor blade. Coffee ring phenomenon was not observed on the final film. Cu, bimetallic and mixed NPs films thicknesses were controlled to 1 to 3 μm Therefore, 10 to 20 layers of NPs (100 to 150 nm) can be sintered on the cleaned glass substrates. After the films fully dried, they were placed in a tube furnace and thermally annealed at 180, 200, 225, 250, 275, 300 °C in the N_2 atmosphere. The temperature ramp rate was set to 5 °C/min and annealing time was 1 hour.

5.8.2 Characterization

The structural characterization of the films was conducted by X-ray diffraction (XRD with Co Ka radiation 0.179 nm, Empyrean series 2, PANalytical). Top view and Cross-sectional view of NPs films before and after annealing at different temperature were analyzed by SEM. The resistivity/ conductivity of a metal film is one property that can characterize its sintering

behavior. Four points probe (Jandel RM2) was used to measure the resistivity of samples, Fig.5.6. The probe consists of four equally spaced tips which pass a current through the outer probes and measure the voltage across the two inner probes. Sheet Resistance assuming a semi-infinite thin sheet in equation 5.6 [ohms/square] [157].

$$R_s = 4.532 \times \frac{V}{I} \tag{5.6}$$

Where V is the voltage in Volts and I is the current in Ohms. Bulk resistivity can be expressed by [Ω/cm] in equation 5.7

$$\rho = R_s \times t = 4.532 \times \frac{V}{I} \times t \tag{5.7}$$

Where t is the thickness of film in cm. Three samples were prepared for each condition. Error bars were made according to the deviations of multiple measurements from all the samples.

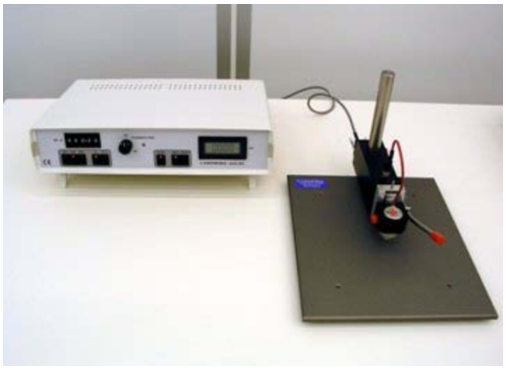

Figure 5.6: Four point probe Jandel RM2 (Bridge technology.co.)

6.0 BIMETALLIC NANOPARTICLE SYNTHESIS AND CHARACTERIZATION

As we introduced in Chapter 2, metallic nanoparticles, especially Ag and Cu, have been widely applied in antibacterial field, including water purification treatment [158], surface coatings [159], products including washing machines [160], and sanitary handles [161]. When nanoparticles are applied to a surface of a device or product such as a ceramic water filter, durability of the nanoparticles coatings are required. To achieve the durable antibacterial nanoparticle films without coarsening the nanoparticles, a low sintering temperature is desired. In our hypothesis, Ag shell Cu core nanoparticles can be sintered at lower temperature and would exhibit antibacterial advantages from both Ag and Cu components.

Although Ag-Cu bimetallic have been in the subject of several studies [27, 52], the effect of the reaction temperature has not been studied in detail. It is hypothesized that the reaction temperature will control the rates of reduction of the silver and the copper ions and therefore the ability to synthesis core shell structures. In this chapter, the synthesis and characterization of Ag, Cu, Ag core Cu shell and Cu core Ag shell nanoparticles are described in detail. The mechanisms for forming bimetallic NPs are also proposed.

6.1 PURE NANOPARTICLE SYNTHESIS AND SIZE COMPARISON

6.1.1 Ag NPs Synthesis and Characterization

The size of Ag NPs synthesized at 140 °C in an oil bath was dependent on reaction time. Ag NO_3 was reduced by ethylene glycol in an oil bath since it was easy to control the reaction

time and particle size by visually observing the color change. The Ag NPs size was 30±7.5 nm after reacting for 20 minutes. As the reaction time increased to 4 hours, the Ag NPs grew to about 77±16 nm (∼80 nm) although the of the size distribution also increased. The larger silver particles grew at the expense of smaller particles which lead to a wider particle distribution by to Ostwald ripening [41]. The Ag NP growth with reaction time is shown in Fig.6.1. The nanofluid was washed three times with ethanol and dispersed with ethanol. Then, the suspension was dropped on a clean glass wafer for air dry in a fume hood.

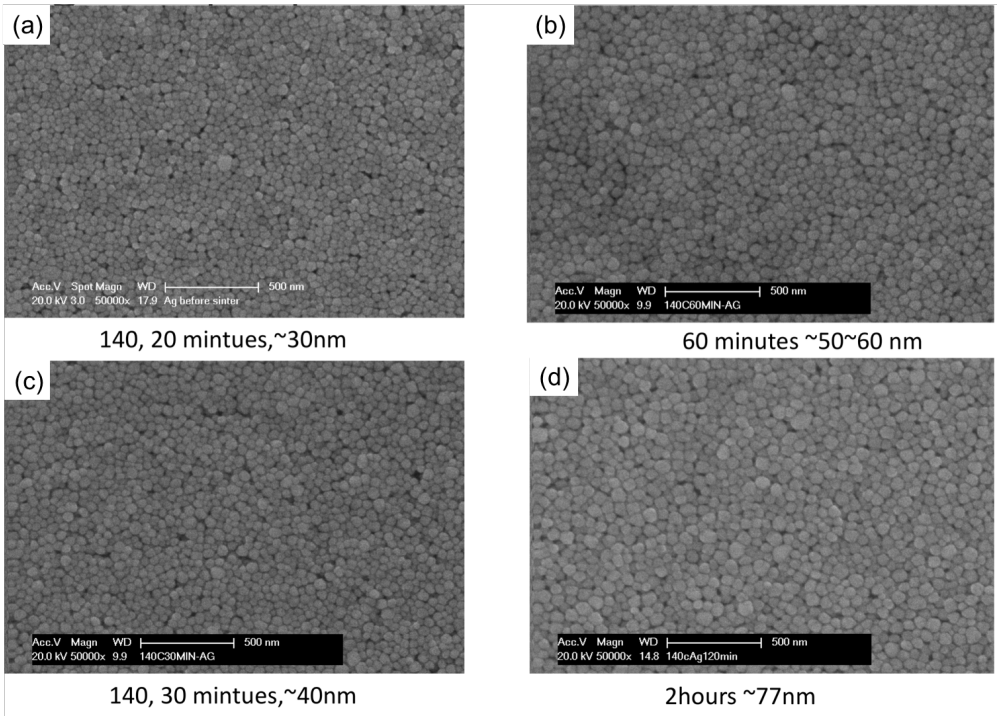

Figure 6.1: SEM images of Ag NPs sizes with various reaction time

6.1.2 Cu NPs Synthesis and Characterization

Cu NPs were synthesized with the polyol method, in which Cu ion reacted with ethylene glycol in the presence of PVP, in the microwave reactor at 175 . By analyzing 50 particles in the SEM image in Fig.6.2, the average particle size was 106±31.5 nm. The average size of particle measured by dynamic light scattering was 92±40 nm in Fig. 6.2(b). The result

was consistent with SEM characterization. The particles were deposited in the same way as the Ag nanofluid and air dried on a class glass slide before imaging.

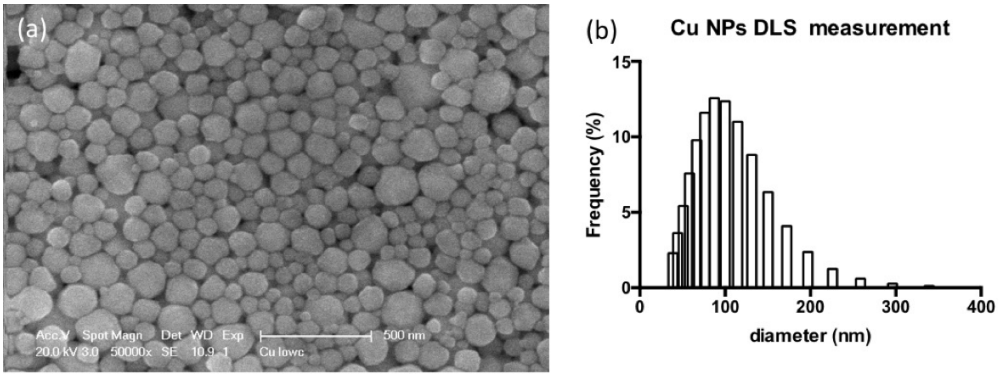

Figure 6.2: (a)Cu NPs in the magnification of ×50000;(b) DLS measurement for Cu NPs

6.2 BIMETALLIC METALLIC NPS SYNTHESIS WITH ONE-POT

Silver (Ag)copper (Cu) bimetallic nanoparticles (NPs) were synthesized by the reduction of silver nitrate and copper (II) acetate monohydrate using ethylene glycol in a microwave (MW) heating system with controlled reaction times ranging from 5 minutes to 30 minutes. The molar ratio Ag/Cu was varied from 1:1 to 1:3. The effect of reaction conditions on the bimetallic NPs structures and compositions were characterized by X-ray photoelectron spectroscopy (XPS), X-ray diffraction (XRD) and transmission electron microscopy (TEM). The average particle size was approximately 150 nm. The surface plasmon resonance (SPR) of Ag-Cu bimetallic NPs was investigated by monitoring the SPR band peak behavior via UV/Vis spectrophotometry. The resonance peak positions and peak widths varied due to the different structures of the bimetallic NPs created under the synthesis conditions. In the MW heating method, the reduction of Cu was enhanced and Cu was inhomogeneously deposited over the Ag cores. As the proportion of Cu was increased in the Ag-Cu bimetallic NPs, the absorption between 400 nm to 600 nm was greatly enhanced.

6.2.1 Ag Core Cu Shell NPs XRD Characterization

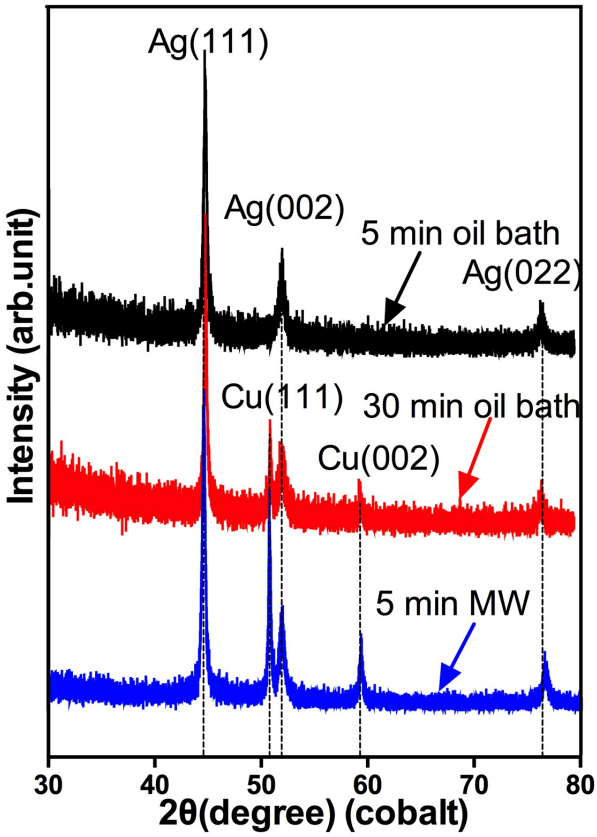

Figure 6.3: XRD diffraction patterns of the nanoparticles synthesized with oil bath heating for 5 minutes, 30 minutes and microwave reactor heating for 5 minutes.

It was observed from XRD (Fig.6.3) that only Ag had been formed in NPs synthesized with an oil bath heat source for 5 minutes, even though the initial ion ratio of Ag/Cu was 1. In contrast, NPs made with the MW reactor showed an XRD spectrum with both Ag and Cu phases present. The Ag/Cu phases ratio was determined to be 44:56 from the XRD spectrum, which was close to the initial ratio of ions used in the reactant liquid. No Cu phase was detected until the oil bath reaction time was increased to 30 minutes and the Ag/Cu phase fraction was still very high at 94:6. The results suggested that, under the conditions used, oil bath heating led to little reduction of the Cu ions for a solution with Ag/Cu = 1. The MW assisted reaction enhanced the Cu ion reduction considerably.

The size of the NPs synthesized with MW assist, measured by DLS, showed a wide distribution, with an average size of 109±45 nm as shown in Fig.6.4. NPs synthesized with an oil bath heating for 5 minutes resulted in smaller NPs with a wide size distribution 90.3±37.8 nm, as marked as a circle in Figure 6.4. When the oil bath dwell time was increased to 30 minutes the NPs increased a little in size, (106±44 nm), similar to the distribution in size synthesized using MW assist for 5 minutes.

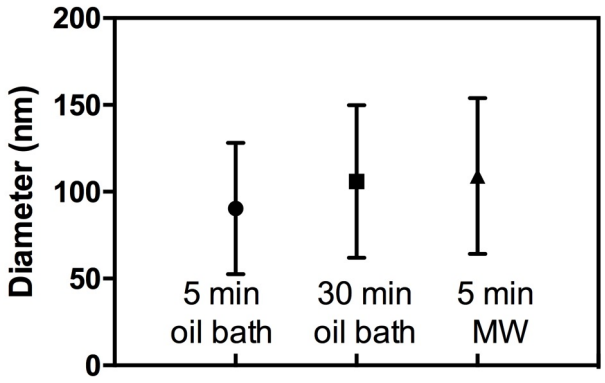

Figure 6.4: Size of nanoparticles measured by the dynamic light scattering method; the nanoparticles were synthesized with oil bath heating for 5 minutes, 30 minutes and microwave reactor heating for 5 minutes.

6.2.2 TEM Characterization

Figure 6.5(a) showed that the NPs synthesized using oil bath heating for 5 minutes were faceted. The NPs sizes measured using 25 individual particles was 147.5±26 nm (aggregates and triangular platelike crystals were not counted). Those NPs synthesized in the MW reactor for 5minutes were 139.6±21.4 nm by TEM measurement based on 27 particles (aggregates and triangular plate-like crystals were not counted). The measurement by TEM was thought to be biased towards the larger sizes, relative to the DLS measurement, because of agglomeration of the NPs during the TEM sample preparation which made it difficult to count some individual particles that were in contact with each other. The triangular-plate like crystals

that can be observed in Figure 6.5(a) and (b) were Ag plates which constitute a minor population for NPs in MW assisted and oil bath NPs synthesis. The shape of NPs synthesized by the MW reaction was relatively irregular while the NPs with oil bath heating exhibited more facets. This implied that the NPs growth occurred more slowly and followed the thermodynamic equilibrium path in oil bath, which was consistent with the fact that the sizes of MW grown NPs were much larger than that of the oil bath method for a same dwelling time.

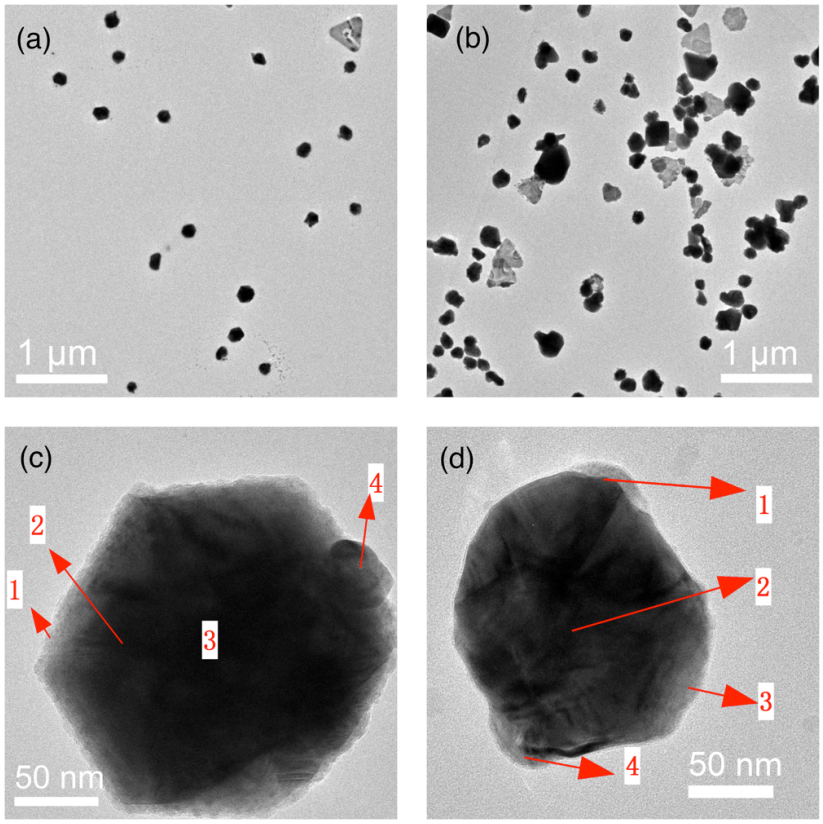

Figure 6.5: TEM images of the nanoparticles made with (a), (c) oil bath heating for 5 minutes, (b),(d) MW reactor heating 5 minutes. Locations for EDS analysis are marked with 1, 2, 3, and 4 in (c) and (d).

The chemical composition was determined at different locations within the NPs using TEM-EDS. The Ag/Cu molar ratios were collected using a spot size of 3 nm. The particles in Figure 6.5(c) and 6.5(d)were considered representative of oil bath and MW assisted

synthesis for 5 minutes. In the oil bath grown NPs, the faceting was well developed. In Figure 6.5(c), EDS analysis shown that Ag/Cu ratio at spots 1 through 4 were 83:17, 98:2, 98.4:1.6, and 82:18, which indicated that a thin Cu layer may have formed on the Ag-rich core, although this cannot be confirmed using this analysis it is reasonable to expect the formation of silver cores. This sequential reduction of Ag and Cu (i.e. the nucleation of Ag core and the gradual growth of Cu layer) can be explained by the larger difference in the reduction potential between Ag and Cu. In contrast, the NPs synthesized using MW exhibited different shapes and composition.

Figure 6.5(d) was a TEM image of a NP from the MW assisted synthesis within which the Ag/Cu molar ratio was measured at four different locations labeled 1, 2, 3, and 4. First, the MW assist NPs did not have well-developed facets, which implied that the growth path may be different from that observed with oil bath heating. Second, the composition of the surface region was not uniform. The Ag/Cu ratios at these locations were as follows: (1) 89:11, (2) 98:2, (3) 2.2:97.8 and (4) 80:20. While the core was still Ag-rich, the shell composition was different from spot to spot. At point 3, the Cu content was actually much higher than Ag content. Inhomogeneous Ag/Cu ratio from spot to spot around the periphery of the particle measured by TEM-EDS analysis suggested that the formation of Cu rich phases was not uniform and their growth mechanism may involve heterogeneous nucleation of Cu crystals on the Ag cores formed earlier in the reduction reaction. Given that MW heats the polyol solution of Cu and Ag ions more uniformly by agitating the glycol molecules, the reaction is thought to have occurred faster in the solution with nucleation of new Cu crystals at the surface of Ag cores.

6.2.3 Optical Property of Ag@Cu Core Shell NPs

From the UV-Vis spectrum, MW synthesized NPs showed broad adsorption spectra with high extinction intensity over the range 300 nm to 800 nm in Fig.6.6. There was some indication of a peak at approximately 430 nm for the MW synthesis, which would be consistent with Ag and a strong absorption from Cu at 587 nm. However, compared with the mixture of pure Ag NPs and pure Cu NPs, enhanced absorption was observed through a range of 420 nm to 800

nm from the MW synthesized NPs. It was reported in several previous studies [27, 162, 163] that two distinct peaks can be found in Ag/Cu core shell NP, one was contributed from the Ag phase and the other from the Cu phase. From the UV-Vis-NIR spectral data, it can also be concluded that the MW synthesized NP were not just a composite NP with independent contributions from the two separated solid phases to the extinction spectra. Compared with the results reported by other research groups, the optical absorption peak reported here suggested a much broader absorption over almost the entire range of measured wavelength, and was thought to be due to a change in the core size or the shell thickness.

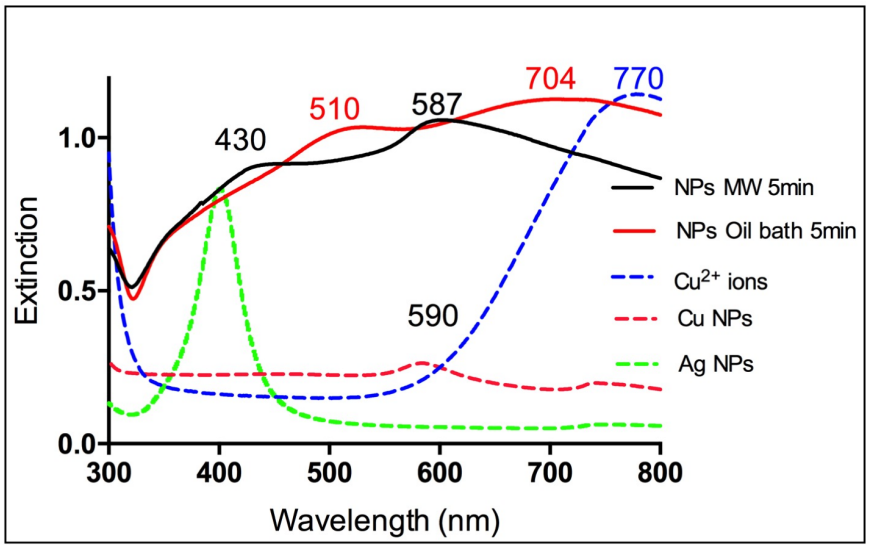

Figure 6.6: UV-Vis extinction spectrum (sum of scattering and absorption) from Cu-Ag nanoparticles (Ag/Cu=1) synthesized with MW heating (black solid) and oil bath heating (red solid). The spectra from pure Cu nanoparticles (dashed red), pure spherical Ag nanoparticles (dashed green) and Cu^{2+} ions (dashed blue) are included for comparison.

In previous study, Ag rich Ag/Cu alloy synthesized using oil bath heating showed one peak at 500 nm, which is similar to pure Ag NPs at the size around 100 nm [164]. In the optical absorption results from this study, the oil bath synthesized NPs, which were mostly Ag, also showed adsorption over the range 300 nm to 800 nm but with some evidence of an absorption peaks at 510 nm. This was thought to be related to the NP structure with its

Ag rich core and very thin Cu shell described above. The extinction spectra were mainly attributed to the Ag phase. The optical peak corresponding to the thin Cu shell was thought to have merged with the main Ag peak. The other broad peak at 700 nm corresponds to the Cu ions that remained in solution, but could also result from CuO which formed from the surface oxidation of Cu NPs. In the FDTD simulation process, extinction (absorption and

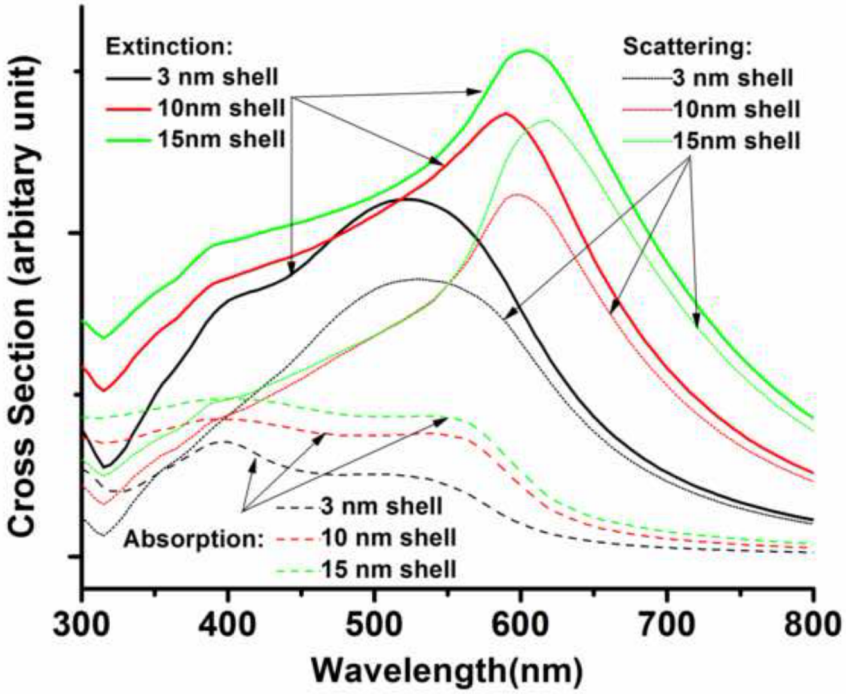

Figure 6.7: Simulated optical spectra of the Ag core-Cu shell particles (core size: 100 nm, shell thickness: 3,10, 15 nm); extinction spectra (solid line), scattering spectra (dotted line), absorption spectra (dashed line).

scattering) from one core-shell Ag-Cu nanoparticle was calculated when a 3D light source was targeting on a "box" in which the nanoparticle was centered. The refraction index in the box near the particle surface was fixed at 1.33 (n(water)=1.33). The absorption and scattering from the simulations were plotted in Figure 6.7. The Ag core was fixed at 100 nm and the Cu shell thickness was set at 3 nm, 10 nm or 15 nm. The calculated spectra were shown in Fig.6.7. The solid black line was the simulation for 3 nm shell thickness, the red line was for 10 nm shell thickness and the green line was for 15 nm shell thickness. The calculated ideal

Cu/Ag molar ratios for these shell thicknesses were: 0.06, 0.8, and 1 respectively. Compared with the extinction of pure Ag and Cu NPs, the core-shell particles dramatically increased the extinction coefficient for light in the range of 450∼600 nm, similar to the results of the experiments. In addition, an increase in the Cu shell thickness shifted the peak position from 540 to 620 nm, possibly due to Cu dielectric effect over the Ag core [165]. Therefore, it was expected that when the core size was constant, the shell thickness can greatly affect the extinction spectra causing broadening and shifting due to the dielectric effect according to their research [165]. Therefore the simulations help explain the experimental observation in Figure 6.6. Since the more uniform and thinner Cu layer was formed by oil bath synthesis, the extinction spectrum of the NPs from the oil bath exhibits blue-shift in comparison to the spectrum of NPs synthesized using MW. The combination of the experiment and the simulation in this study suggest that the formation of the Ag core-Cu shell structure can increase the extinction coefficient of the NPs over the entire visible range and different synthesis heating methods may provide the Cu shell with different composition, size and morphology.

6.2.4 Conclusion

The MW heating method has been shown to increase the rate of Cu reduction during the synthesis of Ag-Cu NPs and suggests this method would be advantageous for synthesizing nanoparticle core-shell structures using metals with very different redox potentials. MW synthesized core-shell Ag-Cu NPs are characterized by an inhomogeneous shell that may result from nucleation and growth of Cu satellites on the Ag cores. In contrast, Ag-Cu NPs made in oil bath are thought to have a more homogeneous core shell structure but the reduction rate of Cu was very slow and the expected Ag/Cu ratio is not achieved. The measured optical absorption of the core-shell NPs synthesized in this study showed high extinction intensity across a broad range of wavelengths compared to mixtures of Cu and Ag NPs and the spectra were significantly influenced by the synthesis conditions. Even though the Cu shell was inhomogeneous, the measured spectra for MW Ag-Cu NPs were found to be similar to the simulated result when the Ag core was 100 nm and Cu shell thickness was

10 nm and the resultant Cu/Ag molar ratio was 0.8. Both the experimental results and the simulation showed a broad extinction spectrum with two distinct peaks at 400 nm and 600 nm, instead of a linear sum of the Cu NP extinction spectrum and the Ag NP extinction spectrum. As the shell thickness increases, the local peaks of the optical spectra shift toward the higher wavelength. The broadened extinction and the peak shift for the visible light is thought to result from the hybridization of the surface plasmons at the inner and outer surface of the shell layer.

6.3 BIMETALLIC METALLIC NPS SYNTHESIS WITH TWO-POTS

6.3.1 Cu Core Ag Shell(Cu@Ag) NPs

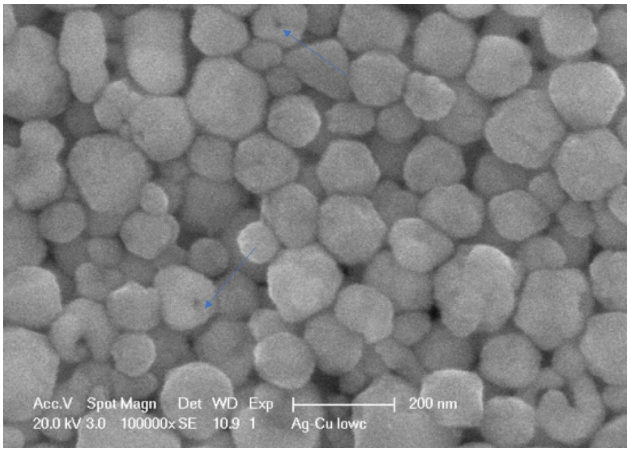

Figure 6.8: Ag-Cu NPs SEM in 100,000 magnification, donut shape NPs were pointed with blue arrow.

The Cu core Ag shell NPs shown in Fig.6.8 were synthesized in two steps. Cu seeds were prepared in the MW reactor at 175°C and then mixed with $AgNO_3$ EG precursors in an oil bath in the second step at 175 °C. The experimental details were described in Chapter 5. The average size of the particle measured with DLS was 128 ± 28 nm as shown in Fig.6.9. This was consistent with the average size of the NPs, 127 ± 24.35 nm, measured manually

by circling out about 50 particles with ImageJ in Fig.6.8. There were some donut-shape particles observed in Fig.6.8. These particles are thought to be formed from a re-oxidation process in the second synthesis step where Ag ion are introduced to the Cu seeds. The mechanism was similar to the reaction of Ag/Au in Sun et al's study [17]. The Ag^{+}/Ag redox potential (0.7994 eV vs. the standard hydrogen electrode (SHE) is higher than that of Cu^{2+}/Cu (0.337 eV vs. SHE). Cu seeds were oxidized when mixed with Ag ions in the EG solution. As the concentration of Ag reaching to a critical value, Ag atoms nucleate and grow into clusters and eventually form a shell structure over the Cu. Sun et al [17] mentioned that the shell was incomplete at early stage and it was possible for both species ions diffused across the shell, until the seed template was completely consumed. As the reaction proceeding, the incomplete shell will form a seamless and smooth shell through the process such as Ostwald ripening. The proposed reaction is shown in equation 6.1, in which two Ag atoms are generated when one Cu atom is oxidized [54, 151, 166]. In Tsuji's and Miyakawa's results [54, 166], besides Cu core and Ag shell NPs, hollow and donut shape Ag shell particle, similar to those observed in this study, were also observed in the TEM images. In order to confirm that most Ag was deposited over Cu cores, XPS was applied to examine the very surface of the NPs formed into a metallic film.

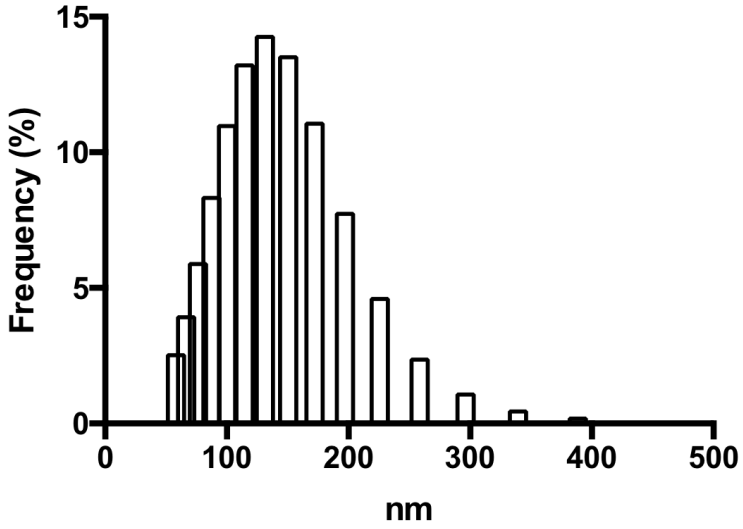

Figure 6.9: DLS measurement for Cu-Ag core shell particles

$$2Ag^{+} + Cu \longrightarrow Cu^{2} + +2Ag \tag{6.1}$$

6.3.2 XRD and XPS Characterization

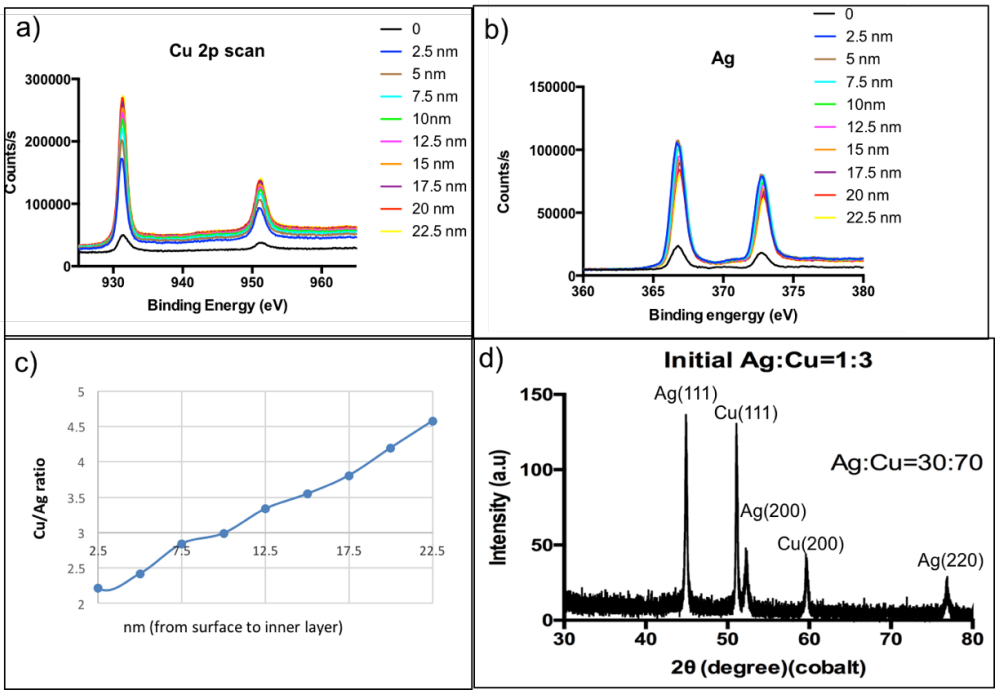

Figure 6.10: a), b) XPS depth profile from Cu@Ag NPs metallic film surface. (c) Cu/Ag ratio as a function depth (from surface to inner region). (d)XRD result of the Cu@Ag core shell NPs sample. The analyzed phase ratio was Ag:Cu = 3:7.

XPS depth profiling was used to measure molar atomic ratio of Cu/Ag from the surface to a depth of ∼23 nm in Fig.6.10. The X-ray spot size was 400 μm and therefore included thousands of nanoparticles. The Ar ion beam energy was set to 3 KeV and the estimated etching rate was 5 nm/min. Each cycle of depth profiling was applied for 30 s and 10 cycles of ion etching was performed. From the outer surface to the inner layer approximately 23 nm from the surface, the intensity of Cu and Ag signals were quantified as shown in Fig.6.10 (a) and (b). The Cu/Ag component ratio based on the detected XRD signal intensity kept

increasing from the surface into interior in Fig.6.10 (c). The base line was set at a ratio of 3 since the expected reactant [Cu]/[Ag] ratio was 3. Within the first 7.5 nm of the surface of the particles, the [Cu]/[Ag] ratio was lower than 3 suggesting, as expected, more Ag than Cu was found on the surface of the particles. It also indicated that some or all of the particles were not fully covered by Ag shells. XPS detected that the Cu/Ag ratio kept increasing to 4.5 with depth indicating the interior of the particles were richer in Cu.

Assuming that there is negligible solid solution between Ag and Cu, the XRD results give a measured Cu/Ag molar ratio of 2.33 which is less than the ratio of 3 expected from the ratio of the silver and copper precursors. This may be due to a galvanic replacement reaction in which part of the Cu cores reacted with Ag ions and become reoxidized Cu ions in the NPs liquid [17]. Therefore, the centrifuged sediments of NPs exhibited a Cu/Ag molar ratio less than 3 under XRD measurement. The shell thickness of Cu@Ag NPs can be estimated using these results, the experimental particle sizes and a model calculation.

Assume that all the particles were core shell structure and all the Ag component was deposited on the Cu seeds. The ideal model was exhibited in Fig. 6.11. The molar ratio of Cu/Ag in the particles was considered to be equal to the phase ratio nCu/nAg=2.33 measured from XRD, combining the Cu seed size (∼100 nm) measured by SEM and DLS. Equation 6.2 and equation 6.3 were presented to illustrate the process of calculation.

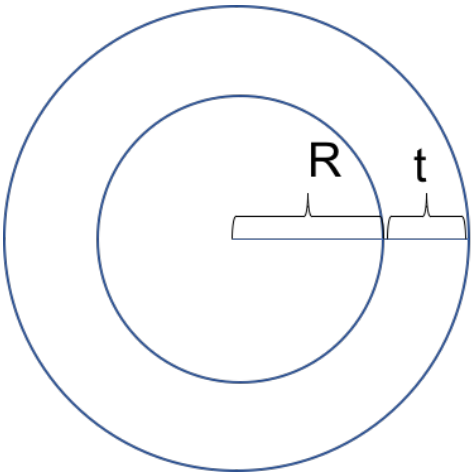

Figure 6.11: Ideal model for Cu@Ag core shell structure.

$$\frac{n(Cu)M(Cu)}{d(Cu)} : \frac{n(Ag)M(Ag)}{d(Ag)} = \frac{V(Cu)}{V(Ag)} \tag{6.2}$$

$$\frac{V(Cu)}{V(Ag)} = \frac{(R+t)^3 - R^3}{R^3} \tag{6.3}$$

Where n(Cu)/n(Ag)=2.33, M(Cu) and M (Ag) are the molecular weight. The density of Ag and Cu are listed as following: d(Ag) 10.49 g/cm^3, d(Cu) 8.96 g/cm^3. R is the radius of Cu core (100 nm) and the thickness of Ag shell can be calculated.

The calculated thickness of Ag shell would be about 7 nm. This assumption requires that the Ag fully covers the Cu cores. However, the XPS and TEM analysis showed that the Ag shell may not fully completed. Some of the Cu seeds were not fully covered with Ag (Fig.6.10(a)).

6.3.3 TEM and STEM-EDS Characterization

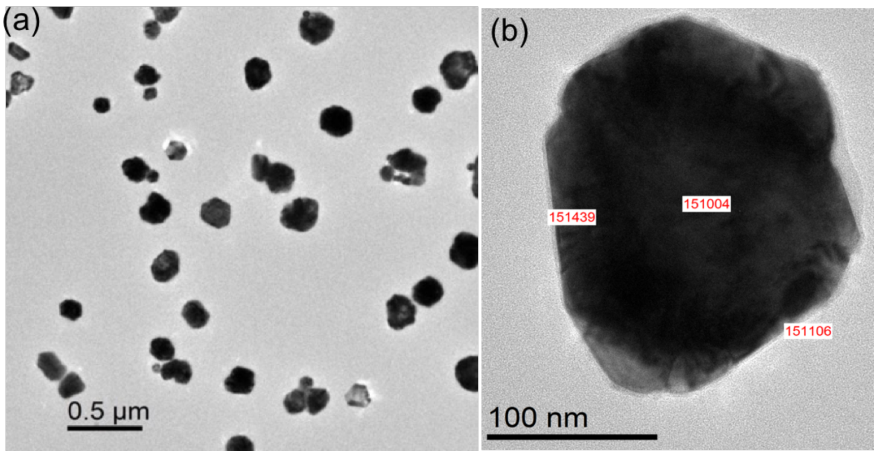

Figure 6.12: a)TEM image of Cu@Ag NPs(b) one NP Characterized with TEM-EDS

TEM-EDS of a representative Ag shell Cu core NP is shown in Fig.6.12(b), the measured Cu/Ag atomic ratio for the whole particle was 69/31. This was similar to the Cu/Ag ratio measured from XRD for the whole samples. From the left, center and right region, Cu/Ag atomic ratio from TEM-EDS were: 4.05/95.95; 86.74/13.26; 2.76/97.24 respectively. This

strongly suggests the presence of a silver shell on the Cu cores and explains why the Cu/Ag ratio on the surface detected by XPS was smaller than 3, while the inner layers shown a Cu/Ag ratio higher than 3. The EDS beam spot size was around 3 to 5 nm. TEM-EDS suggested that some locations of the outer layer of the particle were silver-rich and center of the particle was Cu-rich which makes the Cu/Ag phase ratio consistent with XRD.

STEM-EDS was applied to check about ten Cu@Ag particles. Four out of the ten particles were presented in Fig.6.13. The overall Cu/Ag atomic ratio of these four particles were: (a)90:10; (b)82:18;(c) 63:37; (d)40:60, Fig.6.13. Another four out of the ten examined particles were almost pure Ag or pure Cu. For example, the Cu/Ag phase ratio for two of these particles were 96:4 and 5:95. The last two out of the ten particles were hollow Ag shell particles but contained some copper (e.g. Ag/Cu=67:32; 87:13). From these phase ratio data of the ten particles, we could estimate that 60% of the particles by number were core-shell structure.

Fig.6.13 (a) and (b) show that small amount of Ag (green) was deposited on the Cu cores (red). The Ag shell was homogeneous but not fully formed and most of the particle is Cu. This explains why the XPS did not detect 100% Ag signal on the surface since the shells are not uniform. For the other two particles (c,d), more Ag is deposited on the Cu seeds forming a shell although the thicknesses differ. Also, if this is representative of many of the particles it explains why the XPS detected the surface of NPs film (400 um spot size) had a higher Ag content than the ratio of the phases detected by XRD. The Ag shell thickness could be estimated for the particle in Fig. 6.13 (c) at about 10 nm, it has a Cu/Ag ratio of 63:37 which is the closest to the XRD phase ratio. The particle in figure 6.13(d) has a hollow interior, probably due to the galvanic reaction that reoxidized the copper core. The silver shell could still be estimated at was about 44 nm. While the TEM results show that the core-shell structures are inhomogeneous, it is clear that many of the particles analyzed had a copper core-silver shell structure consistent with the finding of XPS. From analyzing these four particles, the average Cu/Ag phase ratio was 2.2:1 which also was close to the XRD result.

The possible synthesis mechanism could be deduced from the four particles in Fig.6.13 (a)-(d). When Ag ion was firstly introduced to Cu seeds, Ag ions immediately reacted with

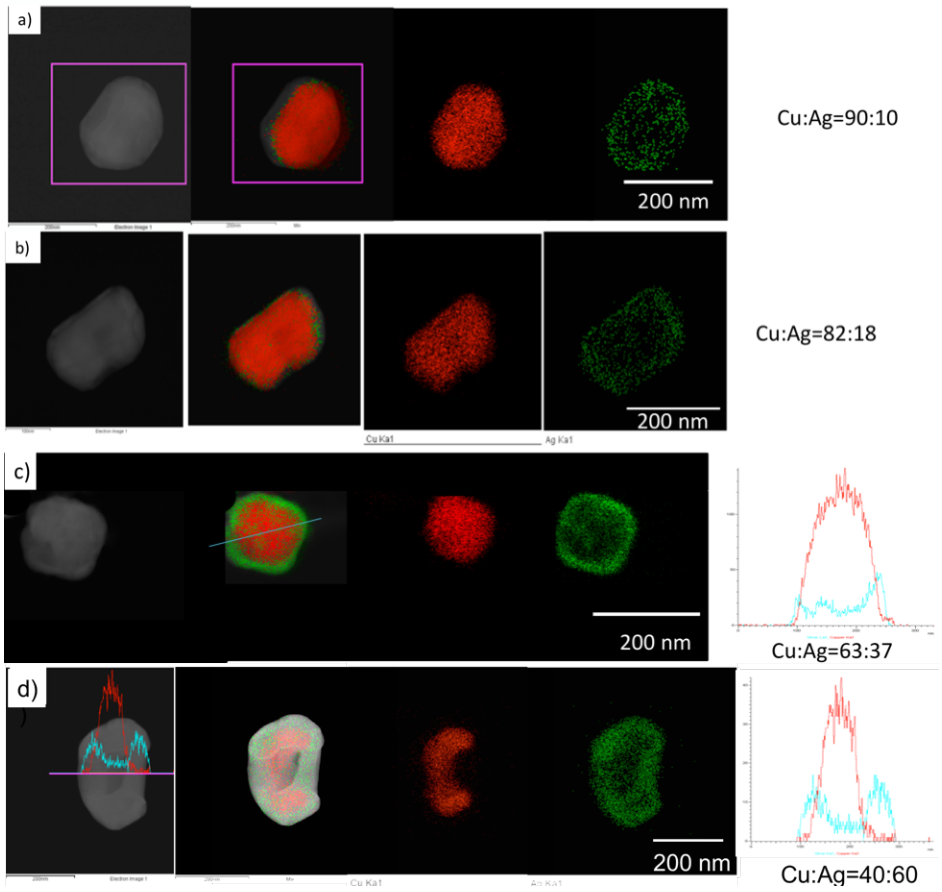

Figure 6.13: STEM-EDX images of Cu Core Ag shell NPs: particle formation process

Cu seeds (equation 6.1). At the same time Ag ions were also reduced by ethylene glycol at 175°C. When the concentration of Ag atoms reached to a critical value, Ag atoms nucleate, grow into clusters and eventually form a shell structure over the Cu. The thin layer was as shown Fig.6.13 (a) and (b). In the early stages of the reaction, Fig.6.13(a) and (b), the Cu/Ag ratio were above 70:30. As the reaction proceeding, Ag kept growing on the Cu seeds and formed a complete shell with a Cu/Ag ratio of 63:37 Fig.6.13(c), which was the closest to XRD examined molar ratio. Incomplete shells will then smooth out through processes such as Ostwald ripening at the high temperature. The mechanism of reaction is described in Fig. 6.16 [17]. The hollow particle in Fig.6.13(d) was also found by Tsuji et al's and Sun et al's [17, 54]. As Sun et al proposed, the shell was incomplete at early stage and it

was possible that both ions diffused across the shell, until the seed template was completely consumed. For our case, the reactant molar ratio [Cu]/[Ag] was 3 and the Cu seeds cannot be consumed especially since Ag ions were being reduced by EG as well.

6.3.4 Temperature Effects on Cu@Ag Core Shell NPs formation

During the synthesis experiments, we found out that different injection temperatures could greatly affect the silver deposition over the Cu cores. Not only the morphologies of the particles have been changed, the phase ratio of the resultant particles were also very different. There was few study that have provided systematic information regarding the temperature effects on the importance of the Ag^+/Cu galvanic effect. In this experiments, the SEM and XRD results have proved that most Cu have been replaced by Ag ions and re-oxidized at lower temperature. To form core shell particles, the higher reaction temperature ($\sim$175 °C) was required.

The particles reacted at each temperature (25, 50, 150, 175°C) are presented in Fig.6.14. When synthesized at 25 °C and 50°C, two types of particles were found. In Fig.6.14(a) and (b) showed that aggregates/clumps of smaller particles were deposited over larger particles. As the reaction temperature increasing to 150 °C and 175 °C, the particle sizes were becoming uniform and their surfaces became smoother shown in Fig.6.14(c) and Fig.6.14(d). This probably due to Ostwald ripening at the higher reaction temperatures.

The Cu/Ag ratios analyzed from XRD were listed as the temperature increased from 25 °C to 175°C as follows: 21:79; 54:46; 49:51; 71:29. This indicated that at lower temperature, Cu core were oxidized by $AgNO_3$ until all the Ag ions were reduced. The aggregates were mostly Ag.

The SEM images suggested that the reaction was very sensitive to temperature since the resultant particle morphologies were very different. Cu/Ag ratio from Ag-Cu bimetallic synthesized at 150, 160 and 175 °C in the second step were analyzed by XRD. The Cu/Ag phase ratio are listed in Fig.6.15, from 150 °C to 175 °C, the phase ratios were 49:52; 65:35; 69:31. As the temperature increasing, the molar ratio was closer to the reactant ratio.

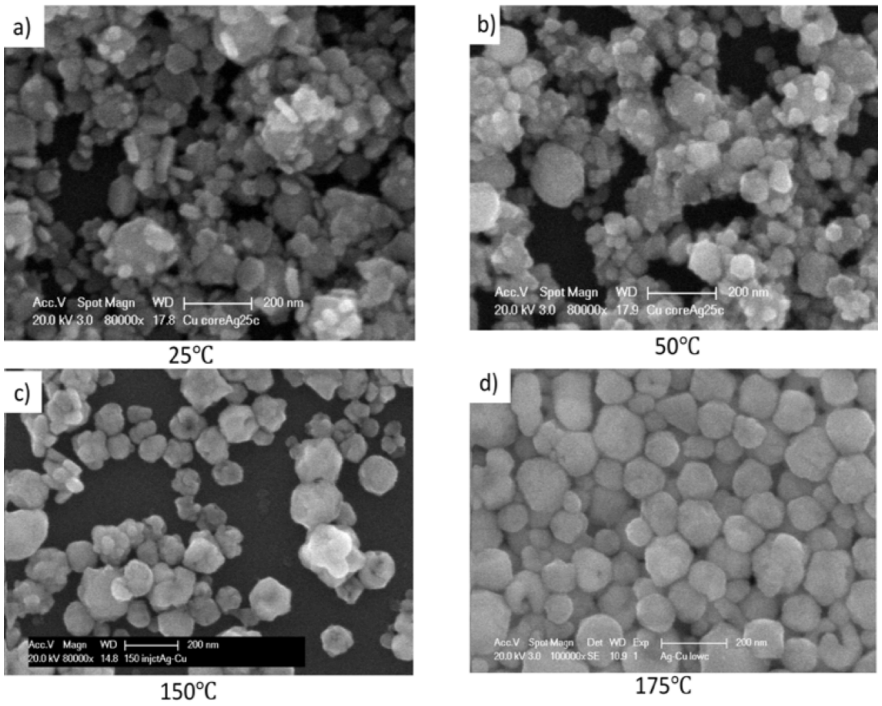

Figure 6.14: SEM images for Ag-Cu bimetallic NPs with an increasing temperature in the second step.

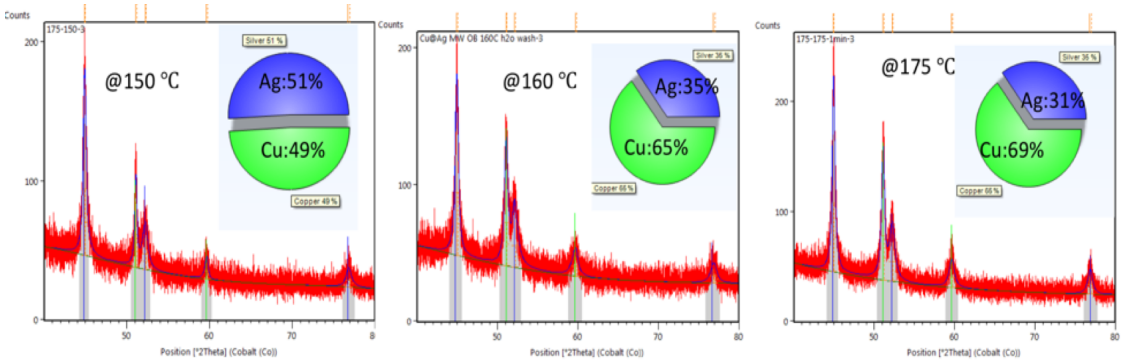

Figure 6.15: Cu/Ag ratio from Ag-Cu bimetallic synthesized at 150, 160 and 175 °C in the second step

Therefore, the galvanic reaction happened more easily at temperatures below 150 °C. At higher temperature, Ag ions can be reduced more effectively by EG and deposit Ag on

the Cu cores. The reaction with Cu seed was suppressed at higher temperature and the Ag is more easily deposited on Cu to give a shell. The creation of thicker silver shells will probably require an excess of copper ions in solution to slow the galvanic reaction. Therefore the copper-silver ion ratio in the reactant fluids should be higher than that required by the particles. Our findings were consistent with Tsujis result [54]. However, the reaction temperature has a strong effect on the phase distribution. Higher temperatures being required to give expected Ag/Cu ratio.

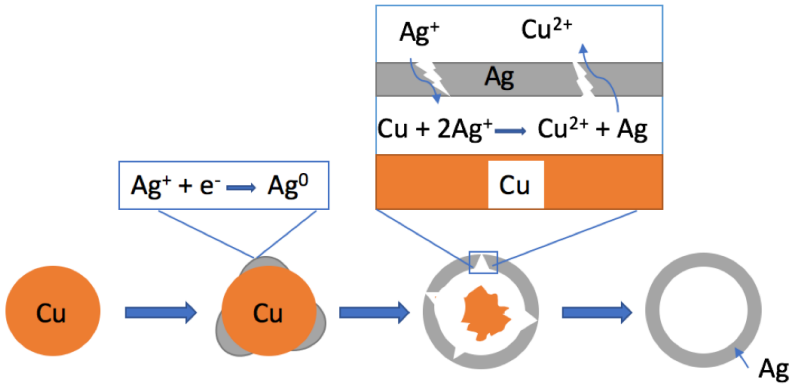

Figure 6.16: Cu@Ag NPs reaction mechanism [17]

6.3.5 Ag shell NPs Synthesis and Characterization

At [Ag]/[Cu]=1, Ag NO_3 and EG was injected into a fluid containing Cu seeds prepared in MW and cooled down at room temperature (25 °C). Following from the work on the effect of reaction temperature it is expected that the silver will be reduced by the galvanic reaction with copper rather than the reduction by ethylene glycol in MW. The TEM image showed that the particles were mainly hollow Ag nanoparticles. Instead of depositing on Cu seeds, Ag ions were reduced at the expense of oxidizing the copper core. The Ag/Cu atomic ratio was 80/20 analyzed by XRD (Fig.6.18). A representative particle, shown in Fig.6.17, was selected to illustrate the hollow NPs. Ag/Cu ratio in the center region was 98:2, while in the

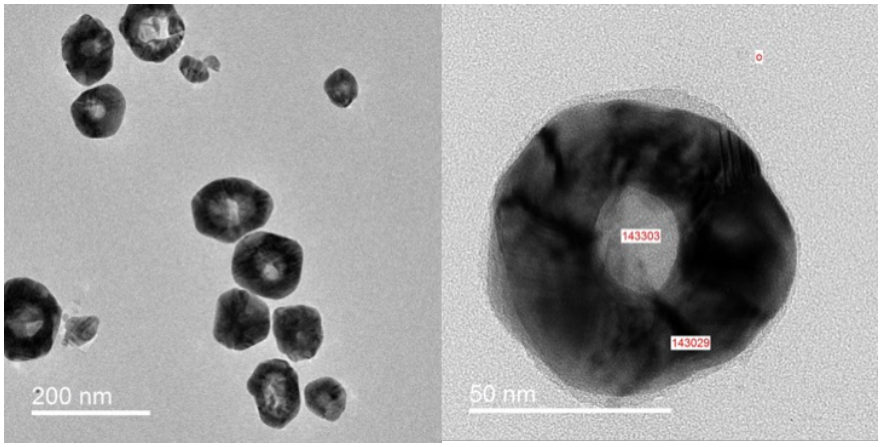

Figure 6.17: Ag shell NPs TEM image

peripheral region the Ag/Cu was 99:1 analyzed by TEM-EDX. Therefore, at low reaction temperature and higher [Ag]/[Cu] ratio, galvanic replacement was dominant.

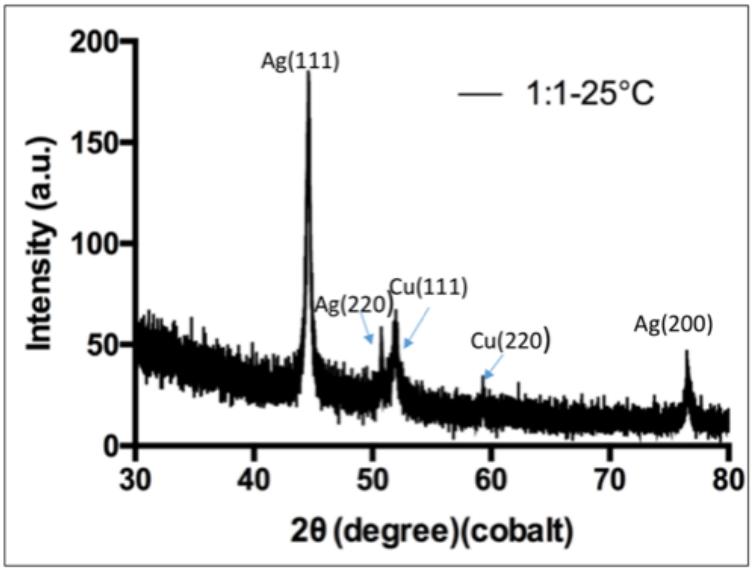

Figure 6.18: Ag shell NPs XRD spectrum

6.3.6 Ag Core Cu Shell (Ag@Cu) NPs in Two Pots

Ag core Cu shell NPs were synthesized in two steps. In the first step, Ag seeds were prepared by reducing $AgNO_3$ in oil bath at 120 °C for 5 minutes. When the Ag NPs were formed, the NPs liquid turned to bright yellow. In the second step, Cu (II) EG solution was mixed with Ag seeds and then placed in MW reacting for 5 minutes at 175 °C (25 minutes ramping time). Ag core Cu shell particle were formed in a MW reactor.

6.3.7 Particle Size Distribution

In the preliminary work, the ideal molar ratio [Cu]/[Ag] = (1,3) were synthesized by keeping the same reaction conditions. The nanofluid of [Cu]/[Ag]=1 was a silvery yellow color while the particles of [Cu]/[Ag]=3 nanofluid was silvery brownish a shown in Fig.6.19(a-b). These particles were dispersed in deionized water and remained stable for one week with little sedimentation. Dynamic light scattering (DLS) data of bimetallic nanoparticle with molar ratio [Cu]/[Ag]=1 shown the average size was about 100 nm±10 nm and with [Cu]/[Ag]=3 shown that the diameter of the particle was around 95.7 ±47 nm in Fig.6.20. The particles sizes were about 40 nm larger than that measured by TEM, which will be presented below.

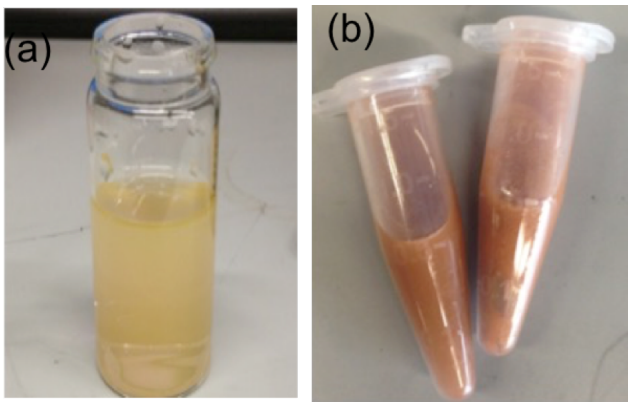

Figure 6.19: Ag-Cu bimetallic nanoparticles in molar ratio of (a)[Cu]/[Ag] =1;(b)[Cu]/[Ag]=3

6.3.8 XRD Characterization

The XRD shown the two separated phases of Ag and Cu suggesting a highly crystalline Ag-Cu bimetallic and Ag core Cu shell (Ag@Cu) NPs were formed by using microwave heating method. In previews studies, the synthesis of Ag core Cu shell NPs was done in a oil bath [54]. Their initial molar ratio was [Cu]:[Ag]=7:1.7, while the resultant shown that Cu/Ag phase ratio was 69:31. It indicated that almost half of total Cu ions are still not reduced. It also suggested that the size of the Ag core would grow relatively large (∼100 nm) before Cu started to deposit on Ag core. Hence, MW was used in this study to enhance the reduction of Cu.

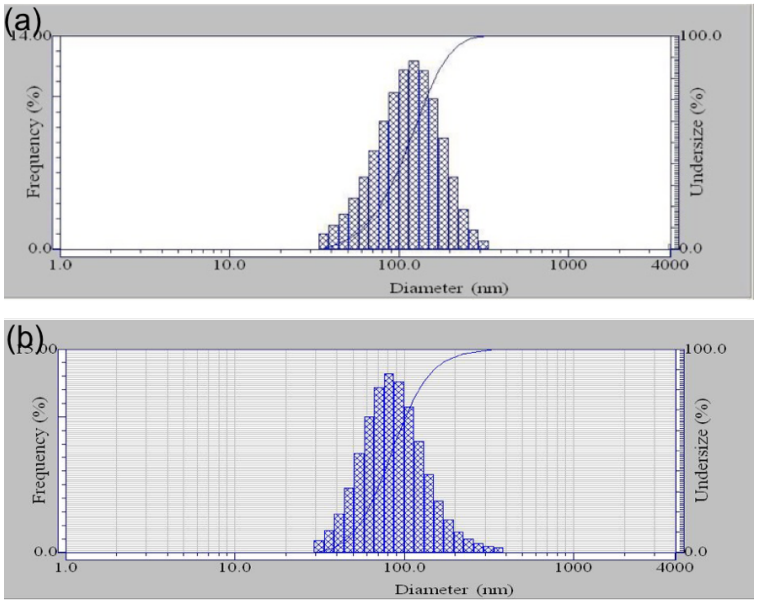

Figure 6.20: Ag-Cu core-shell nanoparticle size distribution measured by DLS (a) molar ratio [Cu]/[Ag]=1 (b) molar ratio of [Cu]/[Ag]=3

The Ag/Cu phase ratio detected from XRD about 1:1 shown in Fig.6.21, black. Oil bath synthesis was also using similar temperature and reaction time to those synthesized using the microwave reactor. However, little of the Cu phase was detected by XRD (Fig.6.21 (red line)). It was observed by X-ray diffraction of the dried nanofluid that little Cu formed in the oil bath synthesis. Until the reaction time increasing to 30 minutes when a weak Cu

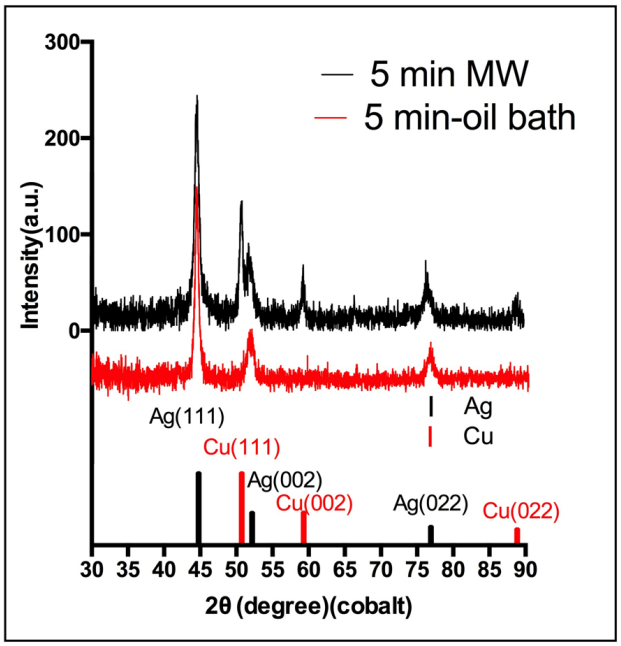

Figure 6.21: XRD of Ag@Cu core shell nanoparticle [Ag]/[Cu]=1, synthesized in MW reactor (black line) and oil bath (red line)

peaks was found. Microwave-assisted synthesized Ag-Cu nanoparticles gave clear Ag and Cu characteristic peaks. The resultant particles had a Ag/Cu phase ratio (Fig.6.21), consistent with the initial $[Ag^{+}]/[Cu^{2+}]$ ratio in the reactant solution, indicating full reduction of both Ag and Cu. within 5 minutes. It can therefore be concluded that microwave enhances the reduction of Cu during the formation of the copper shell. It was also consistent with what might be expected based on the known effect of microwave synthesis. Microwave irradiation is known to produce internal heating in polar liquids and increases the temperature of the whole volume uniformly. Microwave synthesis of nanoparticles tends to be rapid and highly reproducible if uniform heating is achieved by suitable control of microwave output power, temperature and pressure [167]. It is thought that, in this study, the microwave heating enhanced the reduction rate for the copper ions to form the copper shell.

In the previous one pot synthesis used in this study, Ag-Cu bimetallic NPs have been synthesized. The resultant particles were compared with the particles synthesized in oil bath

in section 6.2. The XRD result proved that microwave radiation greatly improved that reduction of Cu ions in the nanofluid. The particles synthesized in one pot by MW are larger (∼150 nm) than those synthesized in a two-step process, in which Ag seeds were prepared first in an oil bath and then mixed with Cu (II) EG solution for microwave reaction. The average size of Ag@Cu NPs synthesized in the two step synthesis were about 50 nm. Therfore smaller Ag core Cu shell NPs were synthesized in the two-step process. This was probably was due to the Ag seeds formed in the first step providing more efficient heterogeneous nucleation sites for nucleation of Cu.

In the one pot MW reaction, Ag^+ ions were reduced vigorously by EG in the MW radiation first and the particles continued to grow until all the Ag^+ ions were consumed. Then the Cu^{2+} were reduced. However, in the two pots synthesis, fine Ag cores can be prepared in oil bath since oil bath heating system was relatively mild. Once the Ag cores was mixed with Cu^{2+} and EG and moved to MW reactor, the Cu was quickly deposited on Ag core and resulted in smaller sized bimetallic NPs compare to the NPs synthesized in one pot.

6.3.9 XPS Characterization

The Ag-Cu nanoparticles were spin-coated on a silicon wafer for characterization by X-ray photoelectron spectroscopy. (Thermo Scientific ESCALAB 250Xi XPS). The main characteristic peaks of binding energy verses counts were presented in Fig.6.22. Fig.6.22 a) showed binding energy peaks of CuO instead of individual signals of Ag or Cu. This suggested that the surface of the nanoparticles is covered with CuO at with a depth of 4.5 nm. Ion beam etching was then used to remove the surface layer. The etching rate of the ion gun correlated to the binding energy of a material and applied energy by the XPS system. After etching away approximately 5 nm of the surface with an etching rate of 0.44 nm/s at 3000 eV, the binding energy of Cu and Ag were detected as shown in Fig.6.22 c) and d) while the signal of CuO was not found. Therefore, it was probable that the surface of Ag-Cu NPs was coated with a very thin layer of CuO protecting the particle from further oxidation. The thin oxidation layer was possible formed when the fluid was taken out from the MW reactor and exposed to ambient environment. The oxide layer is not thought to have grown with

time since the color and size of the particles were not changed over two weeks. The samples were monitored consistently with UV-Vis spectrum.

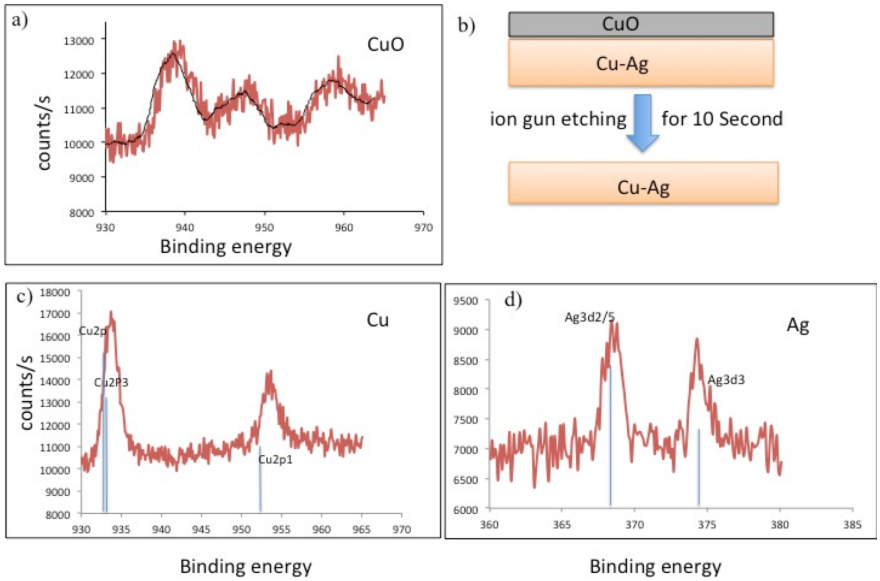

Figure 6.22: X-ray photoelectron spectroscopy of a thin film of Ag-Cu bimetallic NPs nanoparticle with molar ratio of 1:3; a) characteristic peaks of CuO before etching b) schematic diagram of oxide layer; c)d) binding energy of Cu and Ag.

6.3.10 TEM Characterization

The size of the nanoparticle synthesized with the reactant molar ratio [Ag]/[Cu]=1 under MW for 1-minute reaction time were 40± 20nm measured from 50 particles. The diffraction pattern showed both Ag and Cu in Fig.6.23. The three spots 1, 2, 3 on one particle were measured with EDX (spot size ∼3nm), the corresponding atomic ratios of Ag/Cu are as following: 5:95, 94.8:5.2, 2:98 in Fig.6.24. The Ag/Cu ratio difference according to their specific region indicated that Cu is mainly located on the peripheral regions while most Ag is located in the center of the particle. Therefore, it can conclude that Ag core Cu shell particles were formed in the MW synthesis. Two different diffraction patterns were taken from a smaller particle in Fig.6.25. The spacing in the center region was analyzed as identical

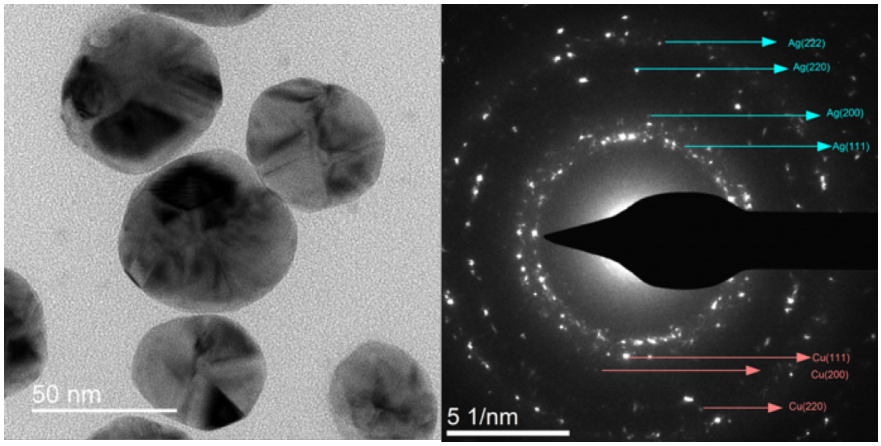

Figure 6.23: TEM image and diffraction pattern from Ag-Cu NPs ([Ag]/[Cu]=1, 1 minute MW reaction. The blue arrow line from top to bottom indicating: Ag (222), Ag (220), Ag(200), Ag(111) ; The red arrow line from the top to bottom indicating Cu(111), Cu(200), Cu(220))

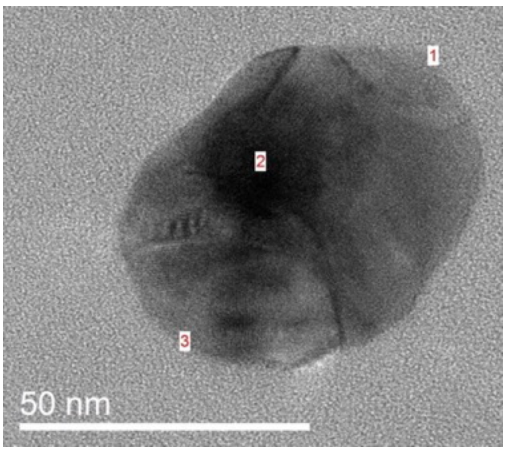

Figure 6.24: Ag seed MW 1minute Ag@Cu nanoparticle.

as Ag (111), Ag (220) and Ag (200). The diffraction pattern on the edge was identified as Ag/Cu alloy [3]. Since the measured dAg/Cu (111) spacing was 2.14, which was between d(Cu)=2.087 and d(Ag)= 2.37. This was probably because for a nanoparticle with smaller size (∼30 nm), the shell of Cu was still very thin and not fully covered the whole Ag seed.

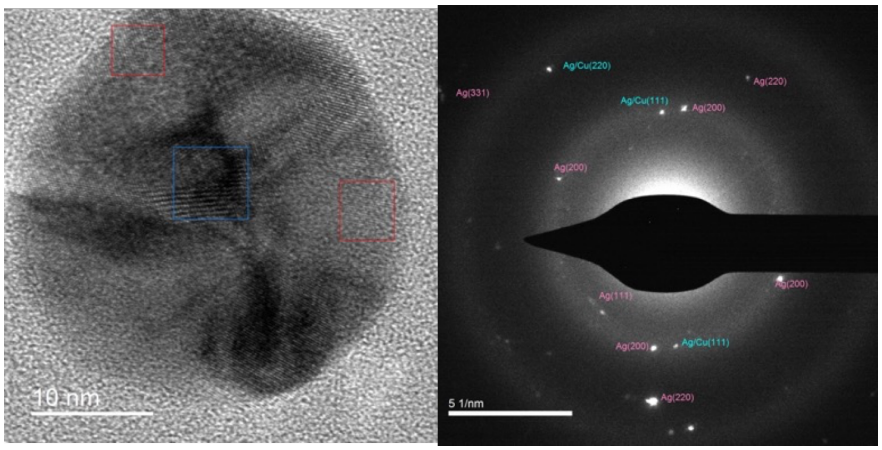

Figure 6.25: A smaller particle around 34nm, the d spacing in the blue square measured through FFT transform pattern corresponding to Ag (111) d spacing, the d spacing measured in red square is close to d spacing of Cu.

Particle synthesized in the molar ratio of 1:3 were also studied. The size of nanoparticle was 50 ±20 nm after being synthesized in MW for 1 minute as shown in Fig.6.26 (a). The size was slightly larger than for particles synthesized with the molar ratio of 1:1. The Cu shell thickness was around 5 nm measured in the Fig. 6.26 (b). Thus, the Ag seeds size was about 40 nm. The HR-TEM image in Fig.6.26 (b) is a higher resolution image of the region in the blue square Fig. 6.26 (a). The d spacing measured from the red squares in Fig. 6.26 (b) corresponded the d spacing of Cu, and the blue squares corresponded to d spacing of Ag. Based on the XRD result, the bimetallic nanoparticle Ag/Cu ratio was 1:3 indicating the full reduction of Cu ions. Therefore microwave heating system increased the reduction and crystallization of copper [168]. In our experiments, we developed two-step method that controlled Ag core size in an oil bath and reached full reduction of Cu ions in MW. The Ag cores provided nucleation sites for Cu atoms for fast deposition with the assistance of MW radiation. Thus, smaller Ag core Cu shell NPs can be achieved compared to the one pot reaction. Control the reactant [Cu]/[Ag] ratio could be used to make thicker Cu shells.

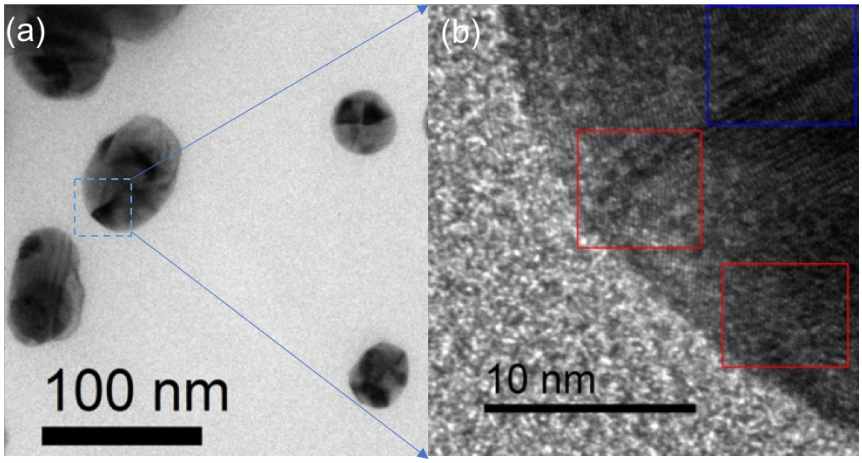

Figure 6.26: (a) a TEM image of Ag core Cu shell NPs; (b)HR-TEM image is from the square drawn on the image with dash line, the d spacing measured in red squares corresponding to the d spacing of Cu. The d spacing measured in the blue square corresponding to d spacing of Ag. (1:3 MW 1min)

6.4 OPTICAL PROPERTIES OF BIMETALLIC NANOPARTICLES

The optical properties of the bimetallic nanofluids were studied in this research. The characteristic absorption peaks of metal nanoparticles are effected by the particles composition, structure and their size due to the metallic nanoparticles unique property of surface plasmonic resonance (SPR) when interacting with the photons of visible light [169, 170].

6.4.1 Ag@Cu NPs Optical Properties

In these experiment, the pure silver nanoparticles prepared in an oil bath (red dash line in Fig.6.27) with size of 30 nm exhibited an absorption peak at 400 nm. It has been reported that as Ag NPs size increases, the optical absorption peak would shift towards the IR region [171]. As the reaction temperature reached 175 °C in the MW reactor, Cu deposited over the Ag seeds. The Ag seeds exhibited a characteristic peak at about 420 nm to 430 nm, which is similar to the characteristic peak of pure 40 nm Ag NPs [171]. This is consistent with the

TEM result (Fig.6.25) which showed that the Ag seeds were about 40 nm. By increasing the reactive [Cu]/[Ag] molar ratio from 1:1 to 3:1, the Cu absorption peak became more obvious at 580 nm. This suggested that the copper shell was becoming thicker. Since MW can achieve full Cu ion reduction, the Cu shell sizes can be controlled. The whole visible wavelength range from 300 to 800 nm were also enhanced compared to the mixture of Ag and Cu NPs. The broadened extinction and the peak shift for the visible light probably result from the hybridization of the surface plasmons at the inner and outer wall of the shell layer.

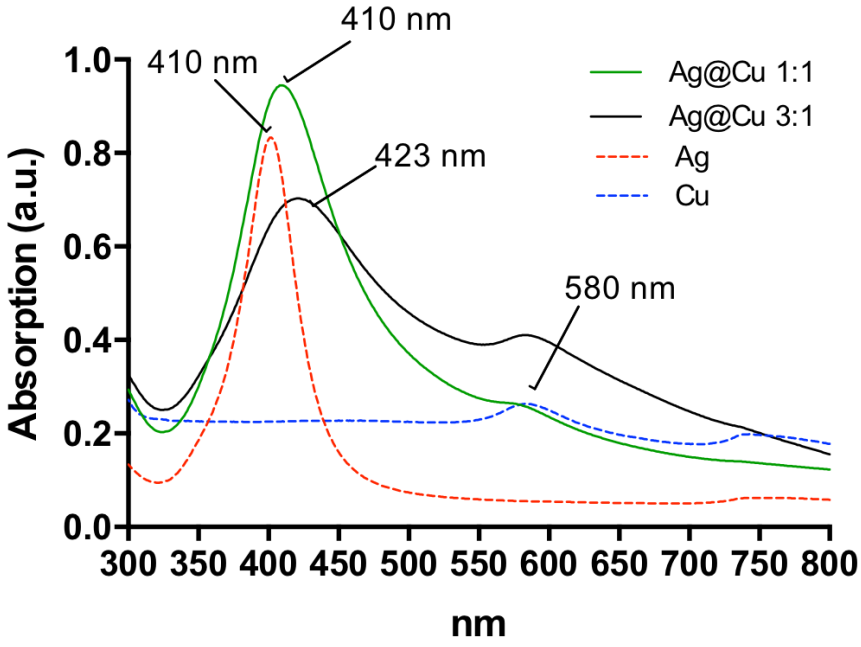

Figure 6.27: Ag seed Ag@Cu nanoparticle UV-Vis-NIR spectra

6.4.2 Optical Properties of Cu Core Ag Shell NPs

Ag NO_3 EG solution was injected into Cu seed at 150°C and cooled down after 5 minutes. The color of the NPs liquid prepared at lower reaction temperature was closer to the color of pure Cu NPs which was brick red. Hence, the absorption peak showed a relatively intense

peak at 580 nm in Fig.6.28 (black line) [47]. The particles prepared at 175°C exhibited a merged absorption peak from both Ag and Cu component where the Ag shell is thought to be dominating the absorption and so the Cu absorption peak was relatively weak Fig.6.28 (red line). This merging of two characteristic peaks was also observed in other hybrid nanoparticles materials [172]. The interaction between two different materials depends on the thickness of the shell and results in a tunable symmetric and antisymmetric nanoshell plasmon [173]. Here, the Ag shell exhibited a dominant extinction peak compared to the Cu's characteristic peak.

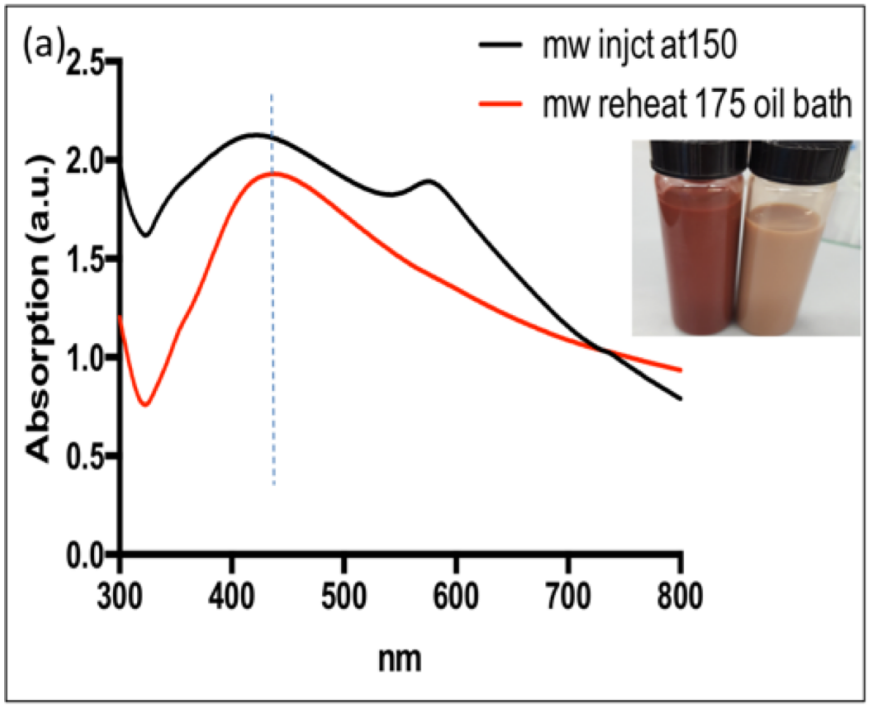

Figure 6.28: (a)UV/vis absorption spectrum from NPs synthesized at 150 °C (left) and NPs reheated in oil bath at 175 °C(right).

6.5 SUMMARY OF AG-CU BIMETALLIC NPS

6.5.1 Cu Core-Ag Shell NPs

The two pot method was introduced in this research and increased the reduction of Cu core seeds as well as increased the reaction efficiency in the first step. In the second step, the Cu core was reacted with Ag NO_3 at high temperature, and it was easier to form a core shell structure due to the deposition of Ag over Cu core at higher reaction temperatures. As the reaction proceeded at lower temperatures, Ag ions were reduced by consuming the Cu core. When the Cu:Ag ratio was 1, galvanic replacement happened easily. Hollow particles were formed at low temperature. Cu core-Ag shell NPs exhibited a merging of extinction peak and Ag shell showed a dominant peak while Cu's characteristic peak was relatively weak.

6.5.2 Ag Core-Cu Shell NPs

From studying the Ag@Cu core shell particles synthesis, it was apparent that the use of MW in the second step enhanced the formation of the copper shell. Optical extinction was observed for the entire visible wavelength range for the core-shell structures. Both Ag and Cu NPs characteristic extinction were found in the UV-vis results as well as the extinction in between was enhanced compared to the mixture of pure Ag and Cu NPs. As the reactive [Cu]/[Ag] molar ratio increasing, the characteristic peak of the Cu shell was enhanced. When the size of Ag seeds was increased, its characteristic peak would also shift towards the IR region. This could may provide new directions in the design of hybrid metallic NPs with turntable SPR.

7.0 ANTIBACTERIAL EFFECTS OF METAL NANOPARTICLES

7.1 EFFECT OF NANOPARTICLES ON ENVIRONMENTAL MYCOBACTERIA

7.1.1 Characterization of Silver Nanoparticle

The crystallite size of the silver nanoparticles used in this study was measured using TEM (JEOL 200CX) bright field images shown in Fig.7.1. The TEM samples were prepared using a drop of silver nanofluid dried on a copper grid in air. The morphology of the particles is equiaxed and selected area diffraction confirmed that the particles were metallic silver. The mean particle diameter measured with ImageJ was 20±5 nm. The DLS data showed that the average size of Ag NPs was about 100 to 125 nm, which was larger than the size measured with TEM. This probably affected by aggregation of Ag NPs [174].

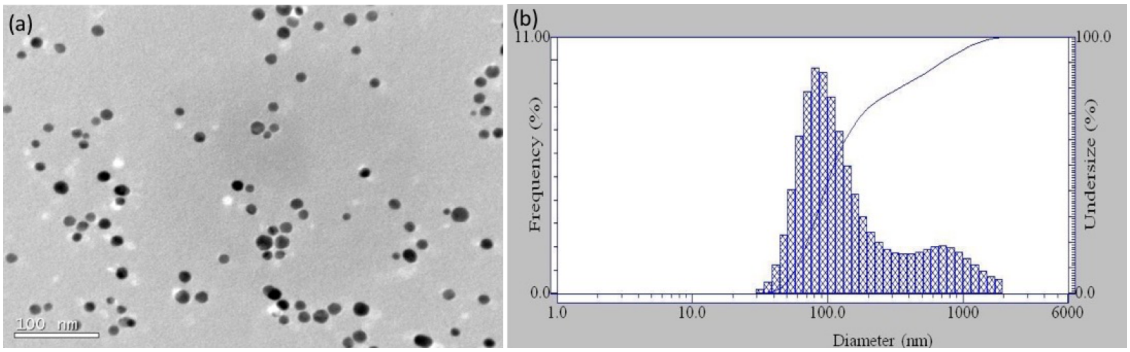

Figure 7.1: (a)TEM image of silver nanoparticles;(b) DLS meassurement for Ag NPs.

7.1.2 Toxicity of Ag NPs to Planktonic Mycobacteria

The percent survival of mycobacteria wild type (MC^2 155) and Ag resistant mutants (Agr-1) was evaluated when exposed to silver nanoparticles for 48 hours and then plated for CFU counting. The results are shown in Figure 7.2. Without Ag NPs in the media, M. Smegmatis grew 188,800%. Ag NPs inhibited growth of MC^2 155 above 12.5 μM and a bactericidal effect was achieved above 25 μM (Figure 7.2). Reduction over the seeded bacteria by 96% was achieved at 100 M Ag NPs. At 200 μM the Ag NPs were completely bactericidal; no CFUs could be counted. There is a clear correlation between Ag NPs concentration and antibacterial effect as seen in previous studies [16],in which the bactericidal effect was also achieved at 25 μM and the reduction reached to 98.7% at 100 μM Ag NPs. However, Ag NPs inhibition effect for the Ag resistant strain, Agr-1 is not obvious until the concentration of Ag NPs increasing to 50 μM. At 100 to 200 μM the Ag NPs did show a bactericidal effect against the silver resistant mutants.

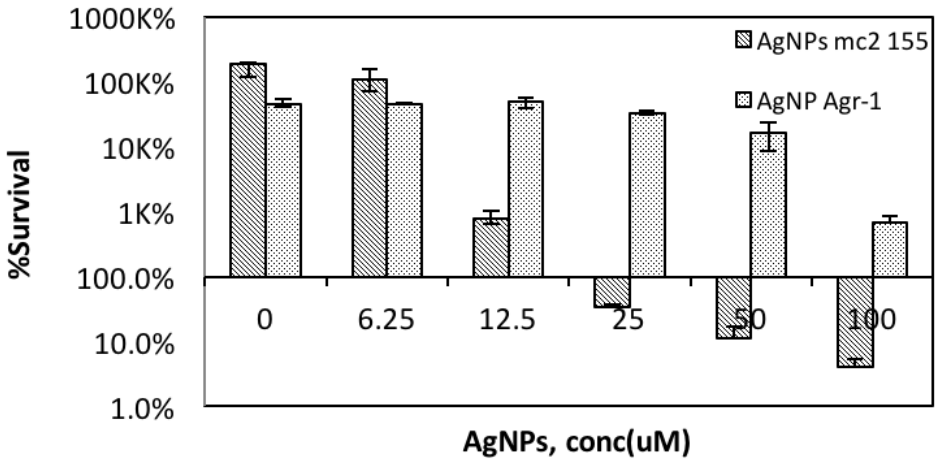

Figure 7.2: Susceptibility of M.Smegmatis (Agr-1) and (MC^2 155) to Ag NPs

7.1.3 Cu NPs Characterization

Cu NPs dispersions reduced by ascorbic acid in DI water (10 nm) were stored in capped glass holder in ambient air for two weeks. The particle sizes measured by DLS were around 10 nm (Fig.7.3). The Cu NPs powder was then prepared for XRD by heating the synthesized dispersion in an oven at 110 °C overnight to evaporate the liquid. The characteristic diffraction peaks of the Cu NPs were shown in Fig. 7.4. The results showed that the particles are metallic copper even after two months in an aqueous suspension. There was also a trace amount of Cu_2O detected.

7.1.4 Toxicity of CuNP to Planktonic M. smegmatis

Fig.7.5 shows the results of CFU counting after 48 hours of exposure to copper nanoparticles. M. Smegmatis (MC^2 155) grew by 133,000% in 48 hours in the unchallenged control group. Cu NPs inhibited growth of MC^2 155 below 3 mM and was completely bactericidal at 5 mM. The same effect also observed on the silver resistant mutant. The bactericidal effect of Cu NPs was achieved at 3mM and completely killing at 5 mM for Agr-1. In the experiments in which planktonic bacteria were exposed to Ag NPs, the silver resistant mutant (Agr-1) showed high resistance to Ag NPs. In Fig.7.2, the survival rate of MC2 155 was 4.1% at the concentration of 100 μM Ag NPs, while the Agr-1 mutants survival rate was 660% which is much higher than the wild type. However, the survival rate of MC^2 155 in the concentration of 5mM Cu NPs was 0.3%, while at the same condition it was completely killing for Ag-r1 mutants. At the concentration of 3 mM Cu NPs, the survival rate of Ag-r1 was 133% which is much lower than the 400% survival rate of the wild type. Therefore, it was clear that the Ag-r1 is more susceptible to Cu NPs than the wild type MC^2 155.

7.1.5 Toxicity of the Mixed Suspensions of AgNP and CuNP to Planktonic M. smegmatis

In the mixture of Ag and Cu nanoparticles, the base Ag NPs concentrations were adjusted to 6.25, 12.5, 25, 50, 100 μM in the culture media and for each of the base Ag NPs concen-

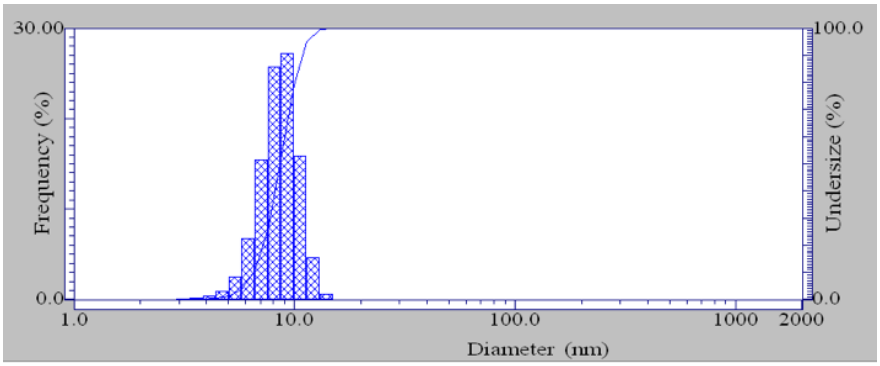

Figure 7.3: Cu NPs nanoparticles size measured by DLS.

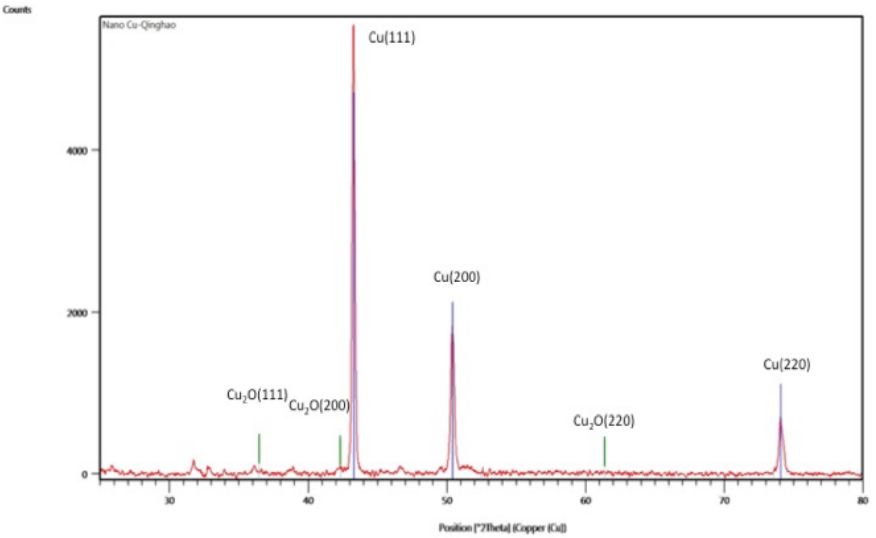

Figure 7.4: Xrd data shows the characteristic diffraction position of Cu NPs.

trations, Cu NPs were added to change the Cu/Ag ratio to 10, 25, 50 and 100. For example, when the Ag/Cu ratio was 10 relative to the base Ag NPs concentrations, the amount of Cu NPs added to the culture media was 62.5, 125, 250, 500 and 1000 μM.

Optical density (OD) data were taken for M. smegmatis in planktonic cultures exposed to mixtures of copper and silver nanoparticles for 48 hours. The survival rate was plotted as OD (48 hours)/OD (initial) verses Ag NPs concentration in μM in shown in Fig.7.8. How-

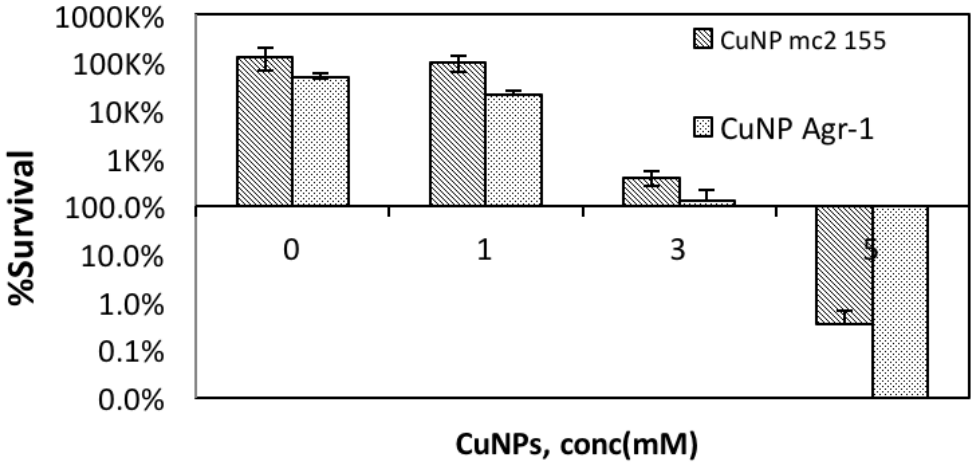

Figure 7.5: Susceptibility of M.smegmatis (Agr-1) and (MC^2155) to CuNPs in planktonic states

ever, the interpretation of OD ratio plot is not quite the same as the survival rate measured by CFU counting. For CFU counts bactericidal effect occurs when the survival rate is below 100%. While for the OD measurement the bactericidal effect occurs at ratios below 1. Therefore, for the OD measurements, the bactericidal effect for Agr-1occurred when the AgNPs concentration (Ag control) was 100 μM. In the mixture of Cu/Ag the amount of silver required for the bactericidal effect decreased as the Cu/Ag increased. For example, when the amount of CuNPs was ten times higher than AgNPs, the bactericidal concentration was at 25 μM AgNPs and 250 μM CuNPs.

In summary, the pure Ag NPs and Cu NPs antibacterial effects were shown respectively in Fig.7.2 and Fig.7.5. For pure AgNPs case, Agr-1 mutants growth was inhibited at 50 μM and the bactericidal effect of AgNPs was at 100 μM. For pure CuNPs case, Agr-1 mutants growth was inhibited at 1mM and the bactericidal effect of CuNPs was at 3 mM. In the mixture of AgNPs and CuNPs, the bactericidal effects (where the ratio of OD (48 hours)/OD (initial) is less than 1) first occurred at Ag NPs=100 μM. When AgNPs was less than 25 μM, bactericidal effect occurs when the amount of CuNPs was 250 μM. The mixture would also be bactericidal when AgNPs was 6.25 μM if the amount of CuNPs was 625 μM and also

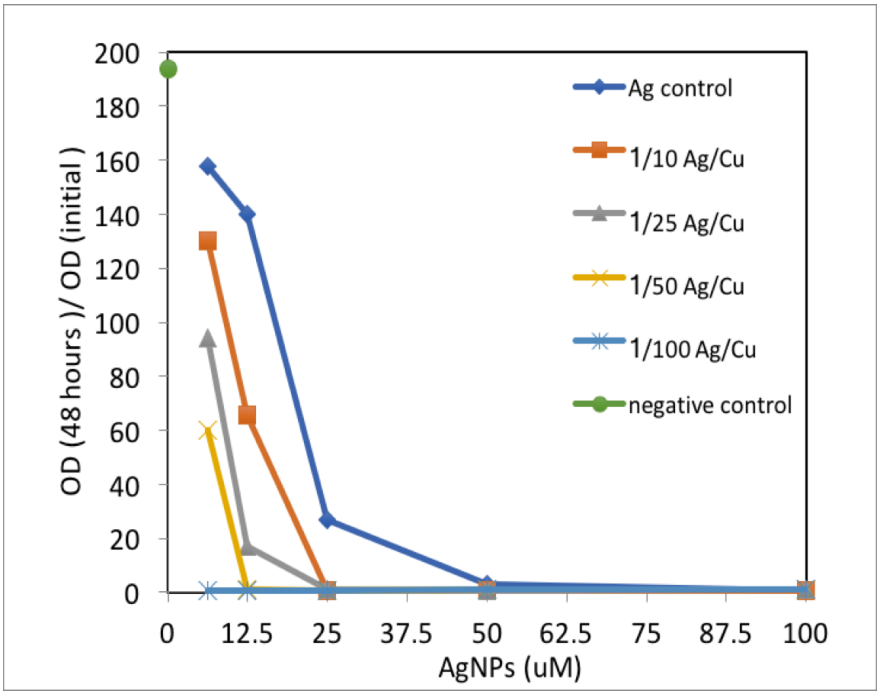

Figure 7.6: Survival rate of Agr-1 in the mixture of Ag and Cu nanoparticles (OD after culturing 48 hours over initial OD) at wavelength of 600nm

when the Ag NPs was 25 μM and Cu NPs was 250 μM (Ag/Cu =10). Considering only the materials costs, this is the most economic mixture of Ag and Cu NPs applied that achieved a bactericidal effect.

7.1.6 Discussion

It has been hypothesized that some species of mycobacteria may have developed a higher resistance to silver as a result of expose to silver ions in their natural environment [16]. If this is the case one would expect that the proliferation of silver nanoparticles in the human environment may cause other species to develop resistance. M. smegmatis cultured in a silver enriched environment developed a stronger resistance to silver than an unmodified strain [16]. This work established the toxic effects on silver nanoparticles and copper nanoparticle on wild type and silver resistant mutants of M. smegmatis. M. smegmatis wild type was susceptible

to Ag NPs at relatively low concentrations, around 12.5 μM. The mutation showed much less susceptibility until the silver content increased to over to 100 μM. Importantly, Cu NPs showed the bactericidal effect at a concentration a hundred times larger than that for Ag NPs. However, the silver resistant mutants were somewhat more susceptible to killing by Cu NPs than Ag NPs, this can be observed from Fig.7.5. Compared with pure Ag NPs or Cu NPs suspensions, the mixed suspensions of Ag NPs and Cu NPs showed an important synergistic antibacterial effect. The bactericidal condition for (Cu(250 μM)/Ag(25 μM)) against silver resistant mutant is about ten times lower than bactericidal condition of Cu NPs ($\sim$ 3mM) and four times lower than the bactericidal condition for Ag NPs (100μM). Therefore, through comparing the antibacterial effects from different amounts of the pure Ag, Cu and the mixture of Ag and Cu NPs, we successfully proved that the mixture of Ag and Cu NPs have an enhanced antibacterial effect in aqueous environment.

Considering the cost ratio of Ag/Cu is around 6.7(silver 17$, copper 2.5$) ignoring the synthesis cost, therefore the option of mixture Ag NPs 25 μM and Cu NPs 250 μM (1.6 mg/L) should be more economical. Due to the maximum contamination level for Cu in drinking water is 1mg/L, the practical application for the mixture of Ag and Cu NPs can be adjusted by slightly increased Ag concentration and decreases in the content of Cu to achieve the bactericidal effect. The ability to reduce the copper content needed for the bactericidal effect by the addition of silver nanoparticles will lower the amount of copper released into drinking water if indeed the silver nanoparticles do release silver ions by oxidation in the presence of the copper nanoparticles. The release of metal ions into the liquid was tested in the next section.

7.2 METAL NANOPARTICLES ION RELEASE IN WATER

7.2.1 Metal Nanoparticle Release and Kinetics

Ag (30 nm), Cu (100 nm), Ag@Cu. Cu@Ag NPs and mixture of Ag and Cu NPs in the ratio of 1:3 have been tested and compared in terms of the release of ions into water over a

period of 7 days under ambient conditions at ∼25°C. The mixtures could release copper and silver ions into the water however one might also expect a galvanic effect that would release copper ions only, based on a comparison of the reduction potentials of copper and silver in water (Ag: +0.7994eV, Cu:+0.521 eV). The galvanic effects mostly occur when the two metallic components, with different electrical potentials, are in electrical contact and both are exposed to an electrolyte, enhancing the ionization of one component of relative negative potential [128]. Unfortunately the water could not be analyzed using common chemical analysis techniques because of the difficulty in removing the nanoparticles and the effects they could have on the results based on the very low concentration of ions expected in solution. Hence it was decided to detect the concentration of ions in the water using electrodes in the presence of the nanoparticles. The ion release rate of Ag-Cu bimetallic nanoparticles was monitored in order to compare it with ion release from pure metal nanoparticles NPs. Any changes in ion release into the nanofluid would be expected to affect the proliferation of bacteria.

Since the membrane of Cu ion selective electrode will be poisoned by the solution containing Ag ions [175], the total ion release in solution was measured by using a conductive electrode [176]. In contrast the silver electrode could be used to measure the concentration of silver ions in the mixtures.

7.2.2 Ag NPs

For the case of Ag NPs, the reaction that releases silver ions from Ag NPs has been reported to follow first order kinetics in several previous studies [7, 116, 125, 177, 178]. Ag NPs react with the oxygen dissolved in aqueous solution (equation7.1) resulting in the release of silver ions under acidic conditions (equation 7.2).

$$2Ag + O_2 \longrightarrow Ag_2O \tag{7.1}$$

$$Ag_2O + 4H^+ \longrightarrow Ag^+ + 2H_2O \tag{7.2}$$

Lee et als [178] research claimed that the redox reaction for silver ionization happened very fast and can reach to equilibrium within the first 6 hours. They also observed that the first-order constant (k) of Ag^+ ions released from Ag NPs was 0.0734/h at 0.05mg/L total Ag at 22°C within 6h. They compared the ion releasing rate (within 6 h) among three different Ag NPs concentrations (0.05,0.1,1 mg/L) and found that the first-order constant decreased as the concentration increasing. This result was consistent with Liu et als [116] research. Liu also observed the first order constant decrease with increasing total silver concentration with longer periods of time (8 days), from 0.88 day-1 at 0.05 mg/L total Ag NPs (6 8 nm), to 0.53 day-1 at 0.2 mg/L and 0.023 day-1 at 2 mg/L. The high concentrations is a complication, since release may be inhibited by reaction induced proton depletion (pH rise), by oxygen depletion and by high concentrations of free silver and free citrate, which may interact with the surface and inhibit surface reactions [116]. Also, the capping agents over Ag NPs in previous studies, were found to affect the dissolution rate of Ag NPs [125]. Kittler et al observed that the rate of dissolution and the final degree of dissolution were higher for PVP-stabilized nanoparticles than for citrate-stabilized nanoparticles. It was suspected that the released Ag ions could be reduced by the citrate coating [125].

The size of Ag NPs also affects the ion releasing rate [120]. Zhang et al compared citrate-coated Ag NPs of 20, 40, 80 nm releasing about 0.175mg/L, 0.1mg/L and 0.05 mg/L Ag ions over 10 days when the total Ag concentrations were kept at 0.6 mg/L. The smaller size of the Ag NPs led to higher ion releasing rate due to the higher surface energy [120]. The release for each case became stable after about 10 days. They also reported that as the Ag NPs concentration reached above 0.6 mg/L, aggregation of Ag NPs would occur rapidly and slow down the oxidation reaction [120].

In this study, Ag NPs (30 nm) coated with PVP in a nanofluid with a concentration of 46 mg/L was prepared, which was much higher concentration than the previously reported concentrations. This concentration was chosen to be consistent with the mixtures of Ag/Cu nanoparticles for which the Cu NPs concentration was 85.3mg/L (1.3 mM) which was in the testing range of the planktonic experiments. Also, the concentrations were consistent with the molar ratio of Ag-Cu bimetallic nanoparticle (1:3), the Ag NPs concentration was 46 mg/L so that the molar ratio of Ag NPs and Cu NPs would be 1:3.

A silver ion selective electrode detected an increase in the Ag ion concentration for 0.487 mg/L (ppm) Ag NPs. Over 6 days the silver ion concentration increased from 1.245 to 1.72 mg/L as shown in Fig.7.7. These results are within the expected range based on the other results of the other research discussed above. The non-zero intercept/initial concentration was also observed in Lee et als results [178]. The higher initial concentration of Ag NPs seems to lead to a higher initial Ag^+ concentration. The detected initial concentration of (Ag^+) at time 0 was about 0.1 mg/L detected in the sample containing 1 mg/L Ag NPs, and reached to 0.5 mg/L after a week [116]. Here, the non-zero initial concentrations were probably due to the way the nanofluids were stored and sampled. High concentration of Ag NPs were synthesized and washed with deionized water three times to remove the excess capping agent and then dilute into the desired concentration with deionized water. Three samples were prepared for each experiment. The ions detected at the start of the experiment probably came from some unreacted reactant ($AgNO_3$) that was not removed by washing. The unexpected values of ion concentration at time 0 was also observed in other research, although no explanation was offered [123].

In order to analyze the experimental data a modified first-order kinetics (equation 7.4) was applied considering the non-zero initial value, Y(0). This equation was based on the equation proposed by Kittler et al [125]. Their model assumed that the initial value of released ion at time (0) was zero and the final value of released ions reached to equilibrium.

The Ag release was plotted in Fig. 7.7(a) and the results detected with Ag selective ion electrode were fitted to equation (4) and presented in Fig. 7.7 (b). The first order constant k(Ag) was 0.27/day (0.01129/h with R^2 =0.9697), which is very close to Kittler et als result (0.017/h at 50mg/ L, PVP-coated Ag NPs).

7.2.3 Cu NPs

The release of Cu^+/ Cu^{2+} from Cu NPs was within a short period of time since the oxidation reaction happened much faster than that for Ag NPs. Previous studies showed a thin Cu oxidation layer forms over the Cu NPs and this caused the release of Cu ion to slowdown [179]. The XPS result in Chapter 6 (section 6.2) exhibited a thin layer of CuO (4 5 nm) over the

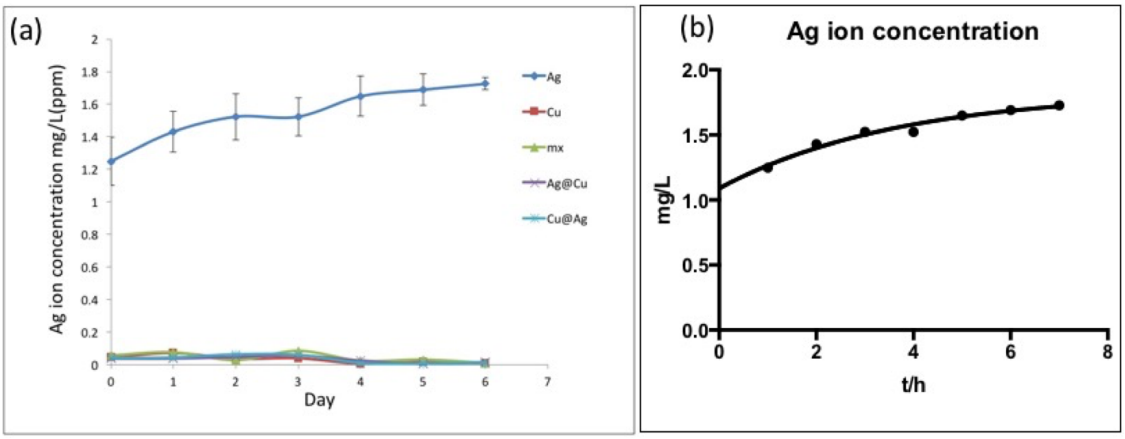

Figure 7.7: (a) Ag ion selective electrode detected silver ion content increased over a period of time. (b) The fitted lines from the first order kinectics equation 7.4.

surface of Ag core Cu shell NPs. Since the reaction for Cu NPs proceeded in similar way in the ambient air, it is believed that there will be a thin layer of CuO present on the surface of Cu NPs. Cu (II) oxidation is the most common oxidation state (US EPA,1995) and this is known to form complexes with hydroxide and carbonate ions. The complex was influenced by pH and dissolved oxygen. Cu (II) ions were the major species in water up to pH 6; at 6-9.3, aqueous $CuCO_3$ was prevalent; at higher pH from 9.3-10.7, the aqueous $[Cu(CO_3)_2]^{2-}$ [180]. In this research, the detected pH was 6 and so Cu^{2+} was expected to be the major species resulting from oxidation.

The release of Cu ions from Cu NPs has also been described using first-order kinetics shown in equation 7.3 over a period of 24 hours [124,125]. This equation was originally used for fitting the silver ion release in Kittler et als research, but also fitted for the release of Cu^{2+} from Cu NPs. A thin layer of Cu oxidation (Cu_2O/CuO) was also detected in their XPS results, which was not considered in the kinetics since the major component was Cu(0) [124]. Most of the Cu ions were released within the first 24 hours which was consistent with the experimental results presented here [123,181].

$$Y(t) = Y(final)(1 - exp(-kt)) \tag{7.3}$$

Equation 7.3 was used to fit the experimental results, where Y(t), is the amount of copper released at time t, Y(final) is the final concentration of copper released [124]. Considering the intercepts value, Y(0), a modified equation 7.4 based on first order-order kinetics was used to fit the experimental results for total ion release since the copper electrode could not be used.

$$Y(t) = Y(0) + (Y(final) - Y(0))(1 - exp(-kt)) \tag{7.4}$$

where Y(0) is the initial concentration, Y(final) was final concentration of released metal ions, i.e., extrapolated t infinite. The values for y(final) and k were extracted from the data by suitable least-squares fitting (table7.1). The results are shown in Fig. 7.8. The fitting results were appropriate since the R^2 values were larger than 0.95. Therefore, this modified first order kinetic model was a good description for our results.

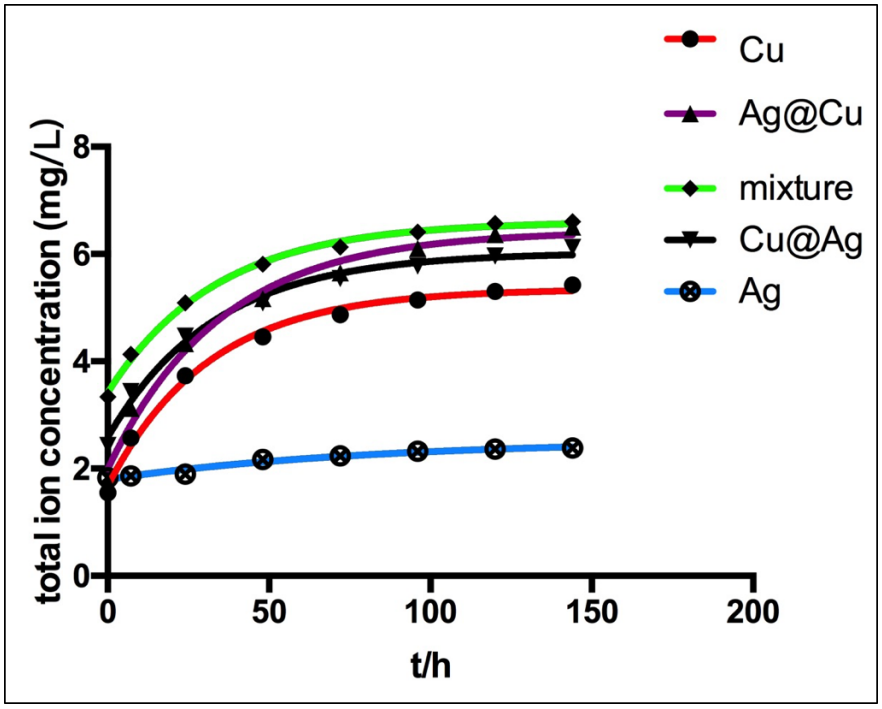

Figure 7.8: The markers were the experimental data of the released ions concentration from Cu, Ag@Cu, Cu@Ag, mixture and Ag NPs. The fitted lines were from the first order kinetics equation 7.4.

Table 7.1: Fitting results by a modified first-order kinetic rate equation

Sample	Y(0)	Y(f)	k(1/h)	R^2
Ag	1.794	2.522	0.01265	0.9703
Cu	1.587	5.336	0.03313	0.9918
Ag@Cu	1.908	6.416	0.02946	0.9831
Cu@Ag	2.509	6.017	0.03126	0.9876
Mixture	3.351	6.595	0.03084	0.995

In this study, the total ion release was monitored each day and plotted in Fig.7.8. For Ag NPs, the ion releasing rate was relatively low compared to the other species due to the relatively lower redox potential of Ag relative to Cu component which would result in a lower rate of ion release into the water. Only 0.487 mg/L Ag ions were detected after 6 days. The total ion increase in 6 days for Cu NPs, bimetallic and the mixture NPs were in a similar range: Cu NPs (3.4687 mg/L), Cu core Ag shell NPs (3.675 mg/L), Ag@Cu (3.695 mg/L) and mixture NPs (3.267 mg/L). However, there was much lower concentration of silver ion detected from the samples of Cu, bimetallic and the mixture NPs shown as in Fig.7.7(a). This is expected if galvanic effects were present. Therefore much of the measured ion release from the mixtures and the bimetallic nanoparticles was probably copper. The concentration of Cu ion released from bimetallic Ag@Cu NPs and the mixtures after a week was slightly higher than that of Cu NPs. This could also be caused by the galvanic corrosion between the attached Ag and Cu phases in the bimetallic particles where as in the pure Cu NP the Cu was oxidized by the dissolved oxygen.

7.2.4 Discussion

The Ag ion release from mixture of Ag NPs and Cu NPs and bimetallic NPs in DI water were suppressed by the presence of Cu, probably due to galvanic corrosion and copper having a more negative reduction potential. Therefore, unless all the Cu became completely ionized, Ag ions would not be released in significant quantities from the nanoparticles. As the introduction section mentioned, first order kinetics is thought to describe the ion release mechanism [116, 120, 125]. The k first-order constant was listed in table 7.1. In a decreasing order: Cu: 0.033/h; Cu@Ag: 0.03126/h; mixture: 0.03084/h; Ag@Cu: 0.02946 /h; Ag:0.01265/h. The rate constant among Cu, Cu@Ag, Ag@Cu and mixed Cu and Ag NPs were very close to one another.They were one order of magnitude smaller than the results of Yu et al research, where the rate constants were measured in organic media instead of DI water [124]. Cu NPs have the highest rate constant, probably due to their relatively smaller size (∼100 nm) compared to that of the bimetallic NPs. The difference in release rates constant between mixture and bimetallic NPs was about 3%. Therefore, it is not thought that the galvanic effect in the bimetallic NPs added much to the ion release rate.

It was noticeable that the release for Cu, Ag@Cu, Cu @Ag and the mixture NPs were much faster in the first 24 hours [179]. Except for releasing higher amount of total ion concentration/Cu ion concentration, the mixture and bimetallic NPs ion release behaviors were not much difference from that of Cu NPs. The most important result was that there was no significant Ag ion release detected in the mixture and bimetallic NPs in deionized water. This is consistent with a galvanic reaction in which the copper is more anodic than the silver. Therefore, the presence of metallic copper will suppress the formation of silver ions. Sediments were also observed after about a week in Cu NPs, mixture and bimetallic NPs samples and could explain the slowing of the total ion release rate from the particles at longer time [116, 120, 125]

In the planktonic experiments, the results did show that the combination of Ag and Cu NPs had better antibacterial effects for silver resistant mutant S.megmatis in culture media. If this is related to the release of ions from the nanoparticles, then the efficacy is not thought to be controlled by the release of silver ions but by the rates of copper ions release into

the media caused by the galvanic reaction. Although the Cu, mixture and bimetallic NPs release behavior were close, the killing mechanism may not be simply correlated to the Cu ion release. Nanoparticle directly contacting cell wall could also be a significant mechanism for bacteria inactivation [91, 92, 182].

Therefore, based on the antibacterial effects from mixture of NPs, which was better than that of Cu NPs, the silver nanoparticles may have also played a role by direct contact with the bacteria and thereby affect the cell membrane directly. It has been reported that the main antibacterial effects from Ag NPs were through the extracellular dissolution and the dissolution on the particle-cell interface [7, 8]. The Ag ionbiosensor applied in their experiment detected 3 times more Ag ions concentration internally in the E.coli cells than that detected in the extracellular suspensions. Since Ag NPs coated with PVP have negative -potential they have the potential to attract counter-ions e.g., Ag^+ and H^+ cation into their diffuse layer by chemisorption [183]. Upon direct contact with negatively charged bacterial cells, the increased concentration of both, Ag^+ and H^+ ions on the particle surface could cause additional damage to bacterial cell membranes, because of the higher local concentration of Ag ions and higher local dissolution rate of Ag NPs.

7.3 INHIBITION OF BIOFILM FORMATION

The antibacterial efficacy of silver nanoparticles and copper nanoparticles was demonstrated for the M.smegamatis wild type (MC^2155) and the silver resistant mutant (Agr-1) in the planktonic state. Deposition by printing allows the same nanoparticles used in planktonic susceptibility studies to be used to study biofilms which are frequently more resistant to antibacterial than the planktonic state [6, 82, 85].

The objective of this research was to culture biofilm on Ag NPs printed polycarbonate micro-filters to examine the effect of nanoparticle patterning rather than the effect of the different nanoparticle metals. This will be an important consideration when optimizing the application of nanoparticles to filters to prevent biofilm formation and fouling. The areal density and morphology of the deposited silver was controlled by varying nanofluid

concentration and the deposition scripture of the inkjet printing system. The effects of areal coverage on biofilm growth were studied.

7.3.1 Polycarbonate Membrane Annealing

The silver nanoparticles were deposited on microporous track etched polycarbonate membranes (Whatman 7060-1304). In order to achieve circular drop formation, the membrane filters were annealed at 125 °C for 10, 20, 30 and 60 minutes. After annealing, Ag NPs suspensions were printed on each of the membranes with the same printing scripture to test the effect of annealing on drop shape. The results are shown in Fig. 7.9. It can be observed that drops spread out mainly along one axis, which is thought to be the track etching directions and tend to form an elliptical spot on the membranes without annealing or for annealing times less than 30 minutes heat treatment. Drops formed round spots gradually on the membranes with longer time of heat treatment. Therefore, all the membranes were annealed for 1 hour to achieve circular drops. The effect of annealing on drop shape is thought to be due to changes in wetting conditions during the heat treatment but the origin of this effect is unclear.

7.3.2 Contact Wetting Angle

A paper coated with paraffin wax paper was used as a moisture-proof substrate. This hydrophobic substrate was placed under the hydrophilic PC membrane to stop the drops from spreading and the assembly became hydrophobic with a contact angle 88 ± 2 degree. Assuming the wet angle was 90 degree, the drop volume was estimated. When an aqueous suspension of nanoparticles was directly printed on a polycarbonate membrane without the hydrophobic substrate the liquid soaked through the membrane and quickly spread on the surface and the spots merged. (Fig. 7.10 (b)). The hydrophobic substrate solved the wetting problem so that the printed drops remained discrete and circular in Fig. 7.10 (a).

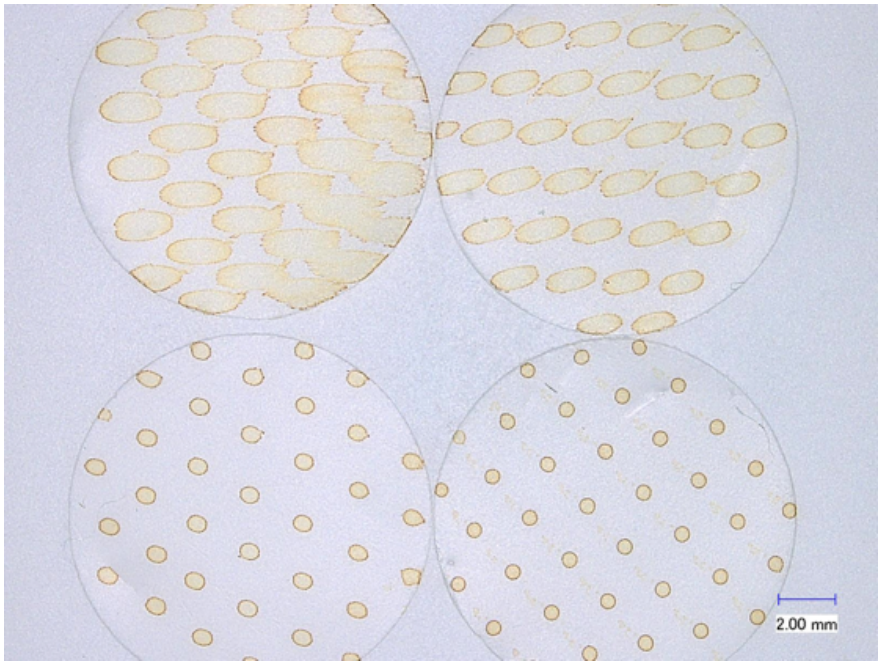

Figure 7.9: Membranes heated to 125°C for 10(left top), 20(right top), 30(left bottom) and 60 (right bottom) minutes, then printed AgNPs with the same pattern scripture.

7.3.3 Deposition of Silver Nanoparticle

Ag-NPs suspensions were deposited on polycarbonate membranes by an inkjet printer (Microfab.Co). The advantage of depositing by the inkjet printer is that the drop sizes and distance can be controlled. The morphology of silver nanoparticle patterned substrates were characterized by optical microscopy. The suspensions were the same as those used in experiments with planktonic bacteria. The residue of each evaporated drop formed a pattern known as the "coffee stain phenomenon [10], where the thickness of the nanoparticle coating in the peripheral region of the spot is higher than the coating in the interior of the dried drop due to evaporation from the triple point where the meniscus meets the substrate. Capillary flow sweeps the particles to the periphery of the drop and pins the meniscus. When the same drops were printed on a silicon wafer substrate, a small mound was observed in the center region of the drop. This is thought to be caused by Marangoni flow, which acts to bring the particles back to the center. Fig. 7.11(a) shows examples of dried spots on the silicon wafer

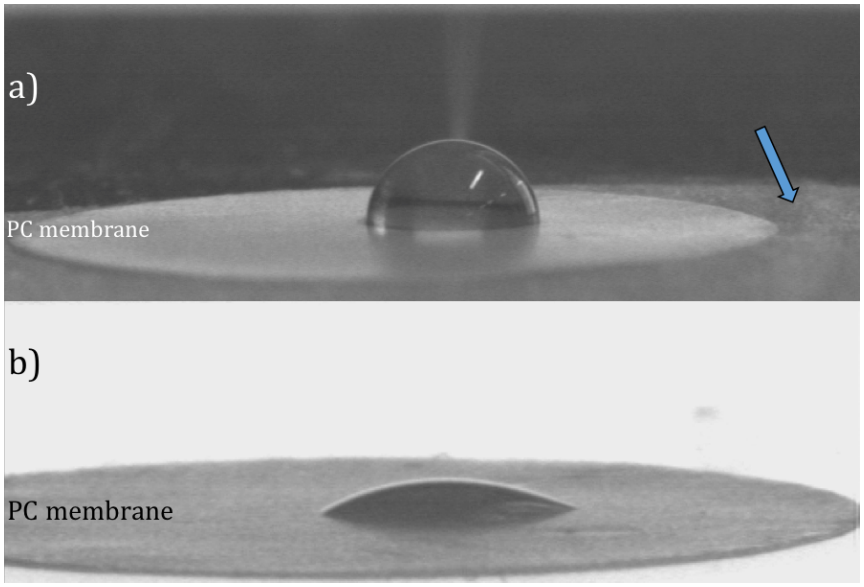

Figure 7.10: a) a silver nanoparticle drop on a PC membrane placed on a hydrophobic layer; b) a drop soaked in a PC membrane

and Fig. 7.11(b) shows the 3D profile taken by an optical profiler (Veeco/Wyko NT 1100). While on the porous polycarbonate membranes, the capillary flow was dominant so that we mainly observed the coffee ring phenomenon without the central mound. This difference is thought to occur because on a porous substrate, radial flow is enhanced by the draining of fluid into the pores, reducing the evaporation flux and leading to reduced Marangoni flow and so the classic coffee staining deposition occurs [10].

7.3.4 Areal Coverage of AgNPs Deposited by Inkjet Printer

Areal coverage of printed spots on the filters were printed in the range of 7.5 % to 30 % areal coverage and measured with a Keyence digital optical microscope. Drops were printed from a nozzle with an orifice dimension of 60 μm. A continuous stream of single drops was achieved by adjusting the backpressure and the setting of bipolar pulse waveform (details were given in chapter 5). The Drop-on-Demand (DOD) inkjet printing process shown in Fig. 7.12 b) c) is designed to avoid satellites. The dynamics of droplet formation of liquid

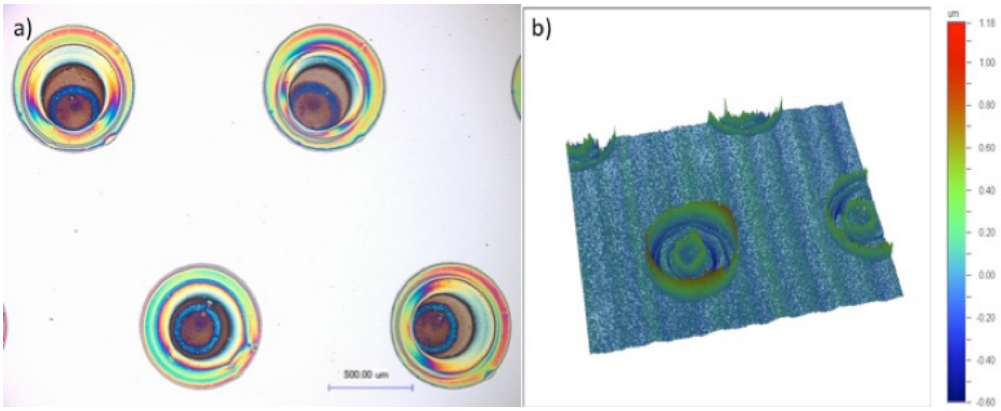

Figure 7.11: a) silver nanoparticle solution printed on a silicon wafer; b) 3D image shows the profile of image (a)

in a piezoelectric inkjet printing process with a bipolar pulse was investigated in this study with the 2.2 g/L aqueous Ag NPs suspension. Fig. 7.12 (a) [Microfab Co.] illustrates the required condition for one single primary drop printed from the nozzle.

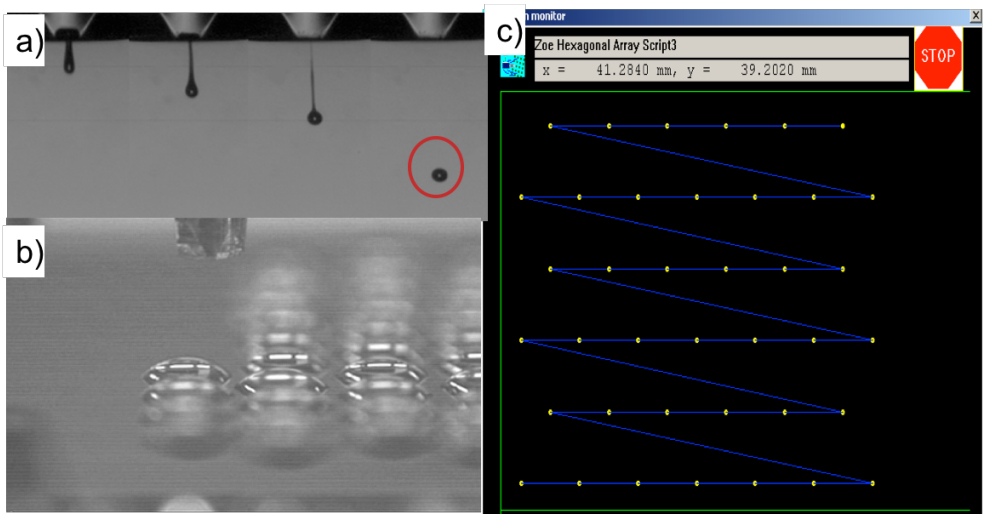

Figure 7.12: a) drops printed from 60um nozzle (Microfab Co.) b) Pattern formation on a substrate c) Demo of printing scripture

Patterning was designed to be self-similar so that size of the spot and the interspot spacing (scale of the pattern) were varied while maintaining the same area density (AD) coverage. The size of the spots was changed by varying the number of droplets used to create each spot. Fig. 7.13 was an example of a 7.5 % AD pattern.

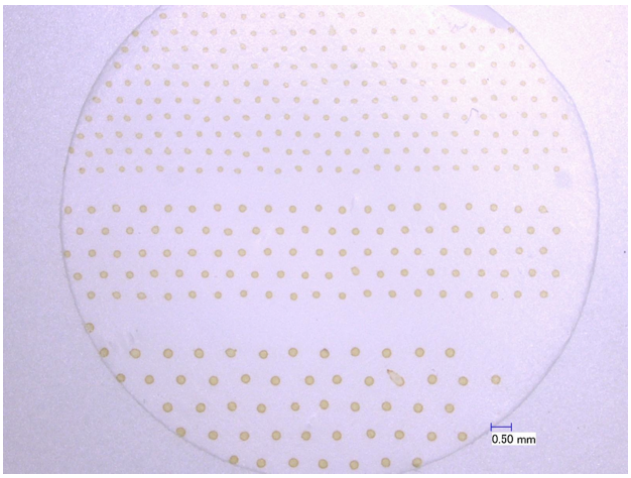

Figure 7.13: Self similarity of patterns of 10 % areal coverage on a membrane

7.3.5 Efficacy of Ag NPs Coated Membrane Filters Against Biofilm

When cultured on porous membranes using the surface bioreactor arrangement described in chapter 5, but printed with Ag-NP, growth of M. smegmatis (MC2 155) was inhibited when compared to growth on an uncoated control membrane. Figure.7.14 shows SEM images of the bacterial colonies on the control membrane filter and the membrane printed with 2.2g/L Ag NPs (AD 15 %) after being cultured for 41 hours. Fig.7.14 b) d) were the processed images of a) and c) processed by image processing software (ImageJ). Discrete bacterial colonies are clearly visible in SEM images. Compared with the negative control, it is obvious the diameters of the colonies on Ag NP printed membranes are smaller and the number of colonies was less. ImageJ was also used to measure the size and numbers of the colonies, which were presented in Fig.7.16. At least three samples for each condition were cultured for about 41 hours. The colonies were characterized with SEM. By analyzing the SEM images

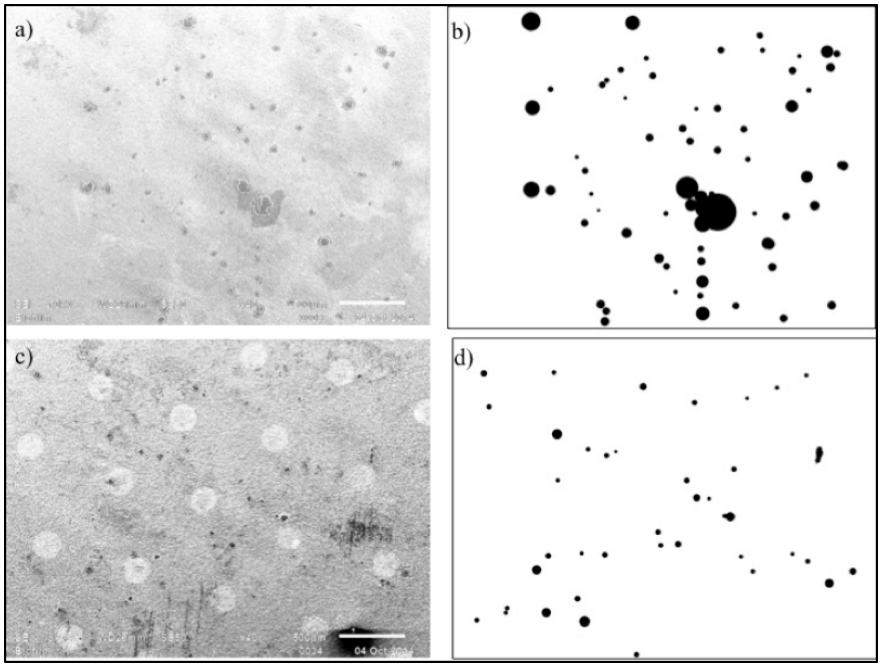

Figure 7.14: After 41 hours culturing colonies were found in the membranes, a) control; b) processed relative image by Image J; c),d) 200 drop pattern. AD=15 %

with ImageJ, the total colonies area was selected and masked with black circles. The colony area percentage was calculated by summing up the total colonies area (the black dots) and dividing the imaged area. All the images were processed in the same procedure, which was exhibited in Fig. 7.14 .

At this culturing time a small number of the colonies were so large that they start to merge together. Each biofilm colony was dense and covered the pores in the membranes. Such unchallenged growth and merger of the biofilm colonies will eventually foul the filter. The experiments clearly show that the printed silver spots inhibit the growth of the colonies and reduce the number of colonies that are formed. The negative control showed the highest colonies area% $\sim$1.89$\pm$0.335% compared to the samples treated with Ag NPs. The colonies area percentage was decreased as the Ag area density increased as shown in Fig. 7.16(a),i.e, 0.82$\pm$0.058 % at AD 7.5%, 0.12$\pm$0.006 at AD 15%, and 0.1$\pm$0.048% at AD 30%.

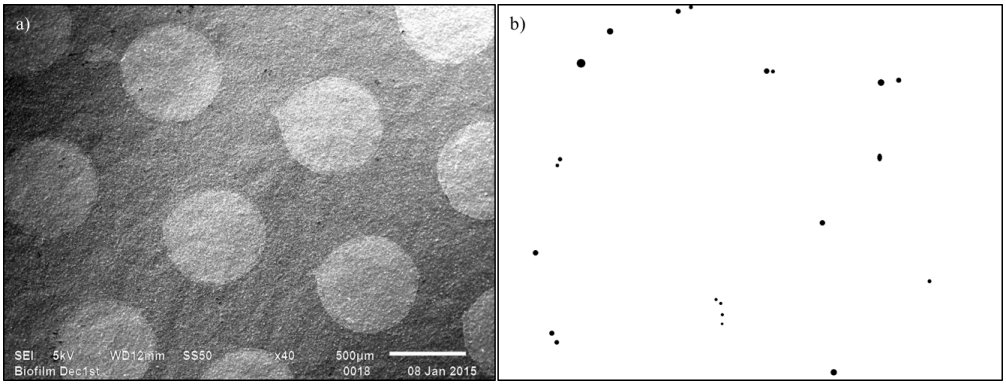

Figure 7.15: (a) SEM image of a 30% AD membrane printed with Ag NPs(b) a processed image with the colonies selected out.

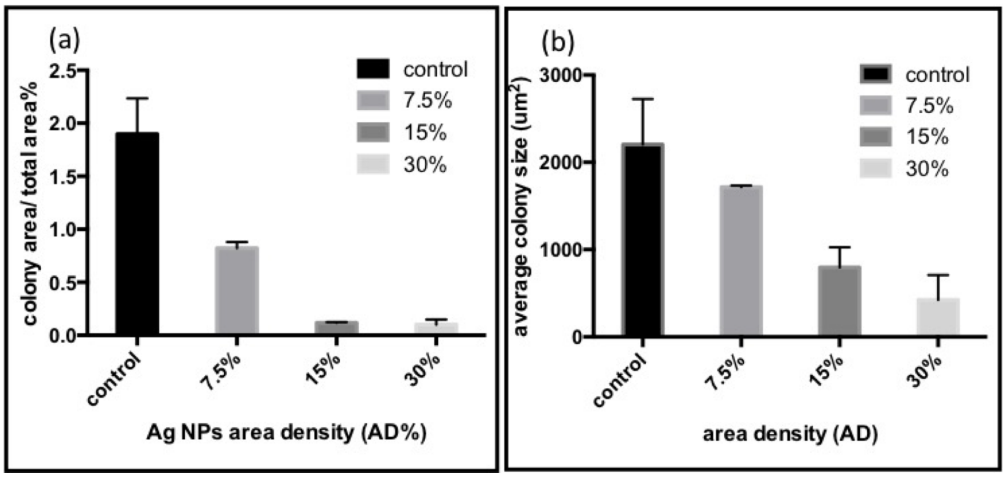

Figure 7.16: (a) Total conlony area verses the meatured area was ploted in the function of printed Ag NPs area density. (b) Average conlony sizes on each microfilter samples printed with Ag NPs patterns with 7.5%, 15%, 30% area density (AD).

As the areal density increased from 7.5% to 30%, the average size of the colonies decreased from 1716 μm^2 to 423 μm^2 (Fig.7.16 (b)). The 30 % AD membrane was printed with the same Ag NPs suspension (2.2g/L) and tested against MC^2 155 mycobacteria. After culturing for 41 hours, few colonies were observed on the membranes and their sizes were

much smaller than for the negative control and for the 15% AD Fig.7.14. Fig.7.15(a) is the SEM image of a 30% AD membrane and Fig. 7.15 (b) is the processed image of image (a).

7.3.6 The Effect of Printed Patterns on the Location of Biofilm Colonies

A set of membranes printed with the same 2.2g/L AgNPs solution (15 % AD) were tested for short period of biofilm colonization. M.smegmatis were cultured for only one day, before they formed large, obvious colonies. Due to the decreasing culturing time, the earlier stage of biofilm colonization could be studied with a particular reference to the spatial location of the printed silver spots. Fig.7.17 (b) shows an example of the colonies with diameters less than 30 μm found equidistant from the drops shown in Fig.7.17(a). No colonies of bacteria were observed on the nanoparticle spots. The orange dashed line outlines a printed Ag NPs spot, whereas the yellow dash line in Fig.7.17(c) is a hypothetical silver ion rich zone in which no colonies were found. Silver ions are thought to have diffused from the Ag NPs spot to form the silver ion rich area. It is thought such a zone of killing exists around each nanoparticle spot, which was very similar to the observation in the disc diffusion antibiotic sensitivity test [184]. In the antibiotic sensitivity testing, if an antibiotic diffuses on an agar plate and stops the bacteria from growing or kills the bacteria, there will be an area around the wafer where the bacteria have not grown enough to be visible, which is called a zone of inhibition [184]. Fig.7.17(d) shows that the bacteria grew along the boundaries of the silver rich zone but did not grow into it. Beyond the killing zones, bacterial colonies were observed, especially at locations equidistant from the spots but the growth of these colonies was inhibited relative to the negative control where the colonies grew randomly and merged together eventually.

7.3.7 Discussion

The SEM results from the work demonstrate that biofilm was inhibited by Ag NPs spot patterns deposited by the inkjet printing system. The inkjet printing technique achieved individual drops printed on a membrane and allows for control of the amount silver nanoparticle in each spot and the spatial arrangement of the spots on the filter surface. On the lower AD

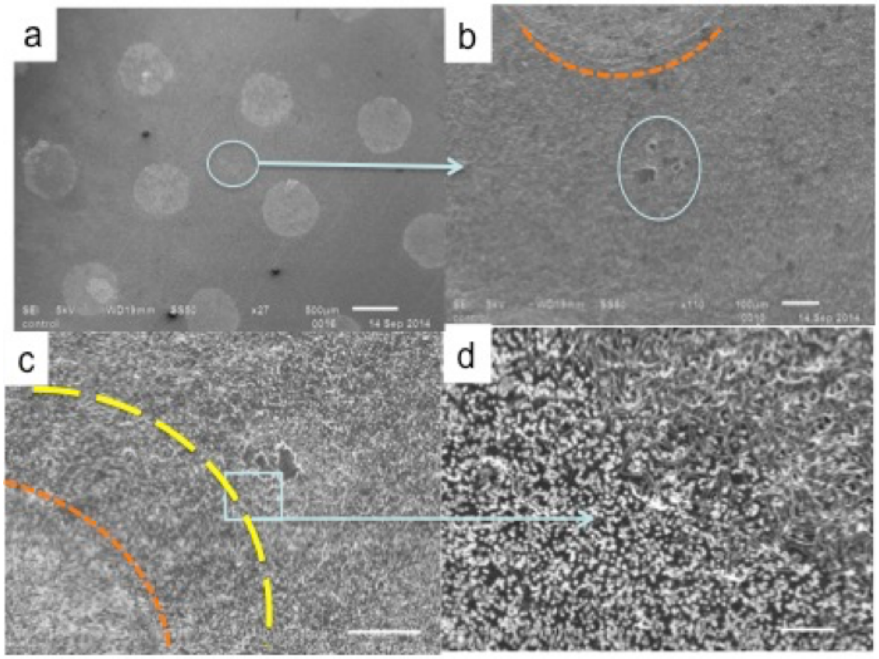

Figure 7.17: Demonstration of the silver spot inhibition effect to biofilm growth at the early attachment stage. a) SEM image of membranes printed with the same 2.2g/L AgNPs solution (10 % AD);b) colonies cultured for 24 hours found in the (a);c) orange dashed line demonstrates the boundary of a silver spot and yellow dashed line is a hypothetical silver rich zone spreading from the silver spot. d) SEM image of bacteria zoomed in from the square in image (c).

membranes, more colonies were observed at locations between the spots due to either the smaller size of the silver spot or larger distance between them. Since the "zones of killing are not space filling in two dimensions, one would expect that, bacteria will grow out from the locations equidistant from the spots and eventually formed a biofilm that will foul the filter. Therefore, fouling will eventually occur for any coating although it may take a much longer period of time.

The zone of inhibition produced in the antibiotics sensitivity test is known to be due to diffusion of the antibiotic out though the agar media. Similarly, the printed Ag NPs dots are thought to be sources of silver ions or even silver nanoparticles which can diffuse out of the

nanoparticle spots into the surrounding wet micro-filter. The released Ag ions or nanoparticles could then directly discourage proliferation of bacteria colonies leading to the "zone of killing around the printed spots. In previous studies, paper wafers/filters were usually impregnated with Ag NPs nanofluid (10μL,) and placed in agar dishes for testing [185]. The measured zones of inhibition against E.coli were in the range of millimeter to centimeter size [186] which is certainly much larger than the killing zones measured on patterned filters in this study and show it is possible to get such diffusion effects from nanoparticle soaked filters. The results of this study show that these effects also apply to patterned filters and higher area coverage of Ag NPs result in improved antibacterial effects and can decrease the size and total number of biofilm colonies at any given culture time. The sample printed with 30% AD Ag NPs effectively eliminated most of the bacteria colonies. The volume for each Ag spots was about 0.02 μL and so the pattern design greatly decreased the total amount of Ag NPs required in antifouling applications compared to covering the entire filter with dilute coatings of AgNPs. Therefore 2D patterning of antibacterial nanoparticles could be used to reduce the amount of silver needed to retard biofilm fouling by manipulating the "killing zones through the diffusion of silver ions or silver nanoparticles out of the printed nanoparticle spots.

8.0 SINTERING OF NANOPARTICLES

8.1 SINTERING OF NANOPARTICLE FILMS

8.1.1 Preparation of Nanoparticle Films

Nanoparticle liquids were suspended in ethanol in the volume ratio of 5%∼ 10%. These NPs inks were then deposited on clean 1×1 cm glass wafers by screen printing. The overall thickness for Cu NPs, mixture and bimetallic NPs films were about 1 μm, while the Ag NPs films thickness were about 300 ∼500 nm. All the sintering procedures were processed in a nitrogen atmosphere.

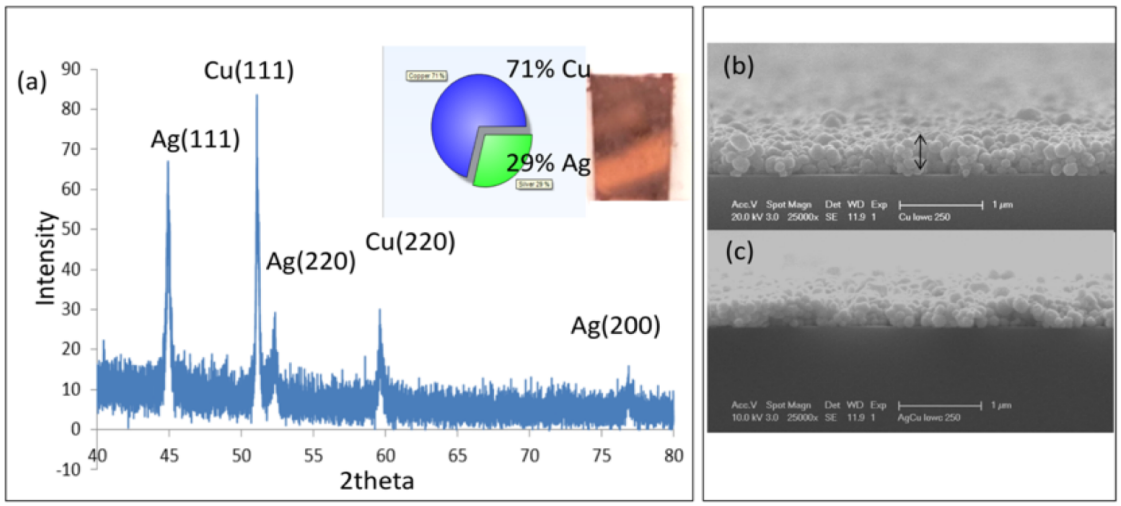

Figure 8.1: XRD spectrum from Ag shell Cu core NPs thin film; (b) Cu NPs film SEM profile; (c) Cu@Ag film SEM profile

The lowest reported sintering temperature for Cu NPs were at 250 to 300 °C [21, 142]. For Ag-Cu core shell particles, the sintering temperature were reported to be about 200 to 250 °C in nitrogen [52]. Mixture of Ag and Cu NPs have been sintered at temperatures from 180 to 210 °C [21]. Based on these studies, the sintering temperature in this study were set in the range of 180 to 300 °C. Due to the various species of nanoparticles, and the size difference, different sintering behavior were observed.

The bimetallic films were a rose gold color as shown in Fig.8.1 (a). Each batch of samples were characterized with XRD before sintering and had a Ag/Cu phase ratio of $\sim$ 30/70 shown in Fig. 8.1(a). The top view and the profile of each film was examined with SEM. Fig.8.1 (b) and (c) gives examples of the SEM profile of Cu NPs film and Cu@Ag films respectively,sintered at 250 °C.

8.1.2 Mixture of Ag and Cu NPs Films Characterization

Ag NPs and Cu NPs films were examined as well as Ag NP/Cu NP 1:3 mixtures and bimetallic nanoparticles with the Ag/Cu molar ratio of 1:3, which was confirmed with SEM-EDX and XRD, Fig.8.2(b). Two kinds of mixed NPs films were prepared: mix-1 and mix-2. The mix-1 film in Fig.8.2(a) was a mixture NPs of Ag (30 nm), Fig.8.2 (c) and the Cu (100 nm) Fig. 8.2(d). The mix-2 film was a mixture NPs of Ag (80 nm) and the Cu (100 nm) shown in Fig.8.8.

8.1.3 Resistivity of Nanoparticle Films

The resistivity of metal NP films were studied to characterized the sintering behavior of each kind of NPs. Low temperature sintering is an effective method to increasing the durability of the antibacterial films in the application of antibacterial filters treated with metal nanoparticles [187, 188]. By bonding the particles to each other and the substrates through sintering without coarsening the particles, the antibacterial effects as well as the durability of the metal particles can be achieved [11].

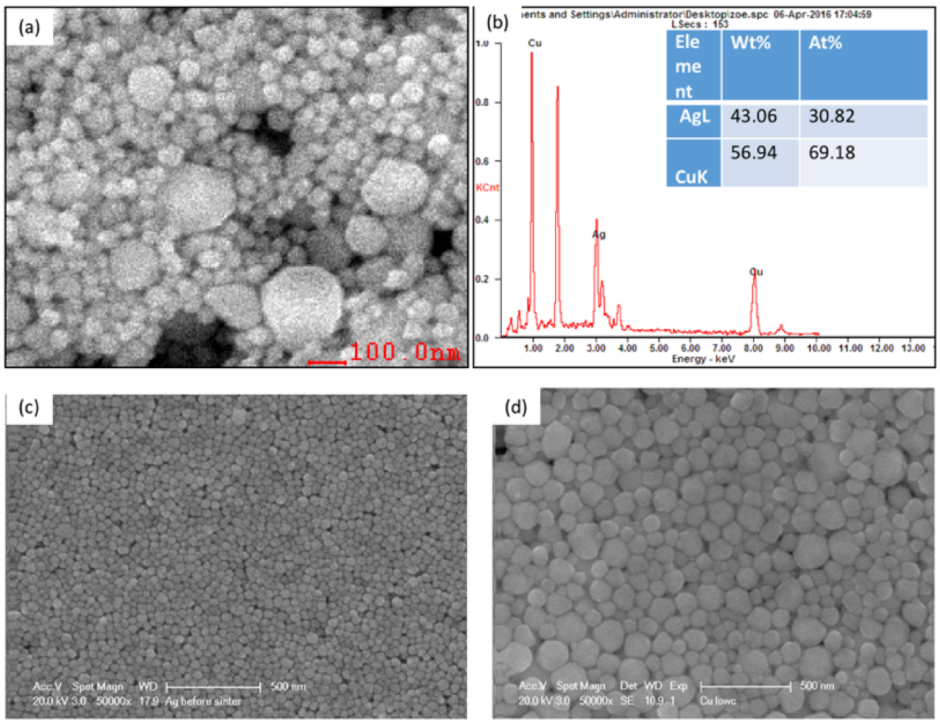

Figure 8.2: (a) A mixture of Ag (30 nm) and Cu (100 nm) NPs, in the molar ratio Ag:Cu 1:3 before sintering; b) SEM-EDX spectrum for the area in (a); c) Pure Ag NPs (30 nm) before sintering; d) Cu NPs (106±31.5nm) before sintering.

The sintering temperature of Cu NPs is reportedly higher than that of Ag NPs (section 8.1.1). Mixed Ag and Cu NPs films were also found to sinter at lower temperature than Cu NPs films [21]. In this research, for the first time that Ag shell Cu core NPs films sintering behavior were compared with Ag/Cu mixture NP films with the same molar ratio.

Ag (30 nm), Cu, Cu-Ag bimetallic and mixture NPs films were sintered in the temperature range from 180 °C to 300 °C. The relative morphology changes of the particles were characterized in SEM using images like those in Fig. 8.3-8.9. Ag (30 nm) thin films were about 100 nm thick, which is much thinner than the other films used for the Cu NPs, the mixtures and the bimetallic particles. Ag (30nm) films showed low resistivity of 20 $\mu\Omega\times$cm when sintered at temperature as low as 180 °C. Cracks that extended to the substrate were formed on sintering at 200 °C (86.7 $\mu\Omega\times$cm) due to differential sintering and the structure

had formed isolated island of silver at 225 °C,shown in Fig.8.3. The resistivity of Ag (30 nm) films reached 2537$\mu\Omega\times$cm because of the differential sintering .

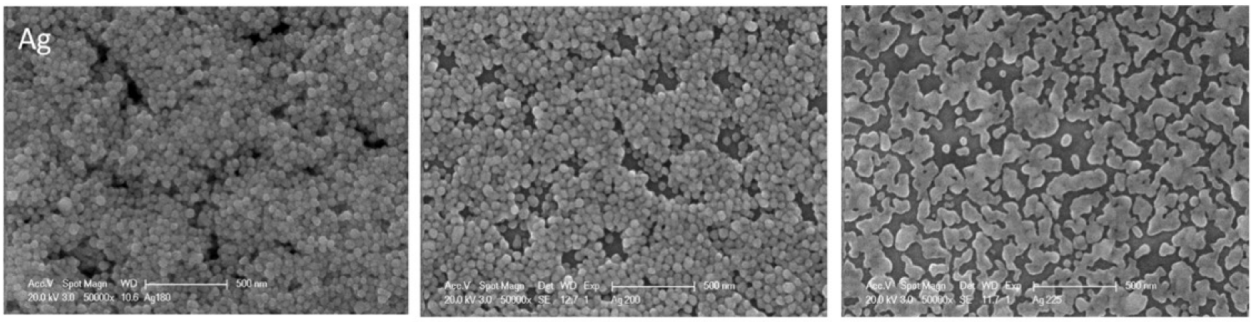

Figure 8.3: The sintering results of Ag (30 nm) NPs sintered at (a) 180 °C ; (b) 200 °C; (c)225 °C .

Ag NPs (80 nm) were synthesized in the same method as Ag NPs (30 nm) except for longer heating time ∼2 hours, which was explained in section 6.11. The resistivity of these films decreased dramatically from 180 to 200 °C, which were 7.8×10^8 $\mu\Omega\times$cm and 1860 $\mu\Omega\times$cm respectively. The higher resistivities of the films made with larger particles at these temperatures are consistent with less neck growth between the larger nanoparticles at 180 °C and increasing the temperature to 200 °C lead to more neck growth and lower electrical resistivity. The Ag particles also grew as the sintering temperature increased, as shown Fig. 8.7. Differential sintering was not observed because the film was about 1 μm, which was thick enough to prevent the formation of silver islands even when sintered at 300 °C.

SEM images of films made from Cu NPs (∼100 nm) sintered at increasing temperature is presented in Fig. 8.4. On sintering at 200°C the films exhibited high resistivity 2.64E+09$\mu\Omega\times$cm which then dramatically decreased to 4294$\mu\Omega\times$cm on sintering at 225°C. As the temperature increase 250 °C, the Cu NPs films reached their lowest resistivity of 442$\mu\Omega\times$cm due to the necking between particles. Differential sintering behavior was observed at 300 °C in Fig. 8.4(c), where NPs aggregates were formed and large cracks were observed between the particles. The film resistivity consequently increased to 2.2E+08$\mu\Omega\times$cm.

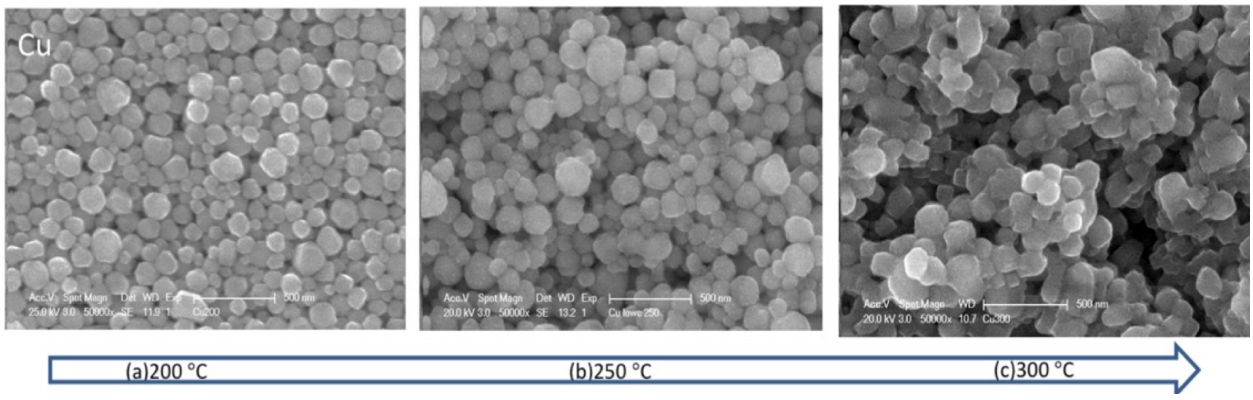

Figure 8.4: The sintering results of Cu NPs ($\sim$ 100 nm) sintered at(a) 200 °C ; (b) 250 °C; (c)300 °C .

8.1.4 The Sintering of Mixture NPs and Bimetallic NPs

The mix-1(Ag 30 nm and Cu 100 nm) NPs film sintering behavior was closer to that of the Cu NPs at lower temperature as shown in Fig.8.5. A high resistivity was observed at 200 °C and it dramatic dropped on sintering at 225°C. However, it then continued to decrease even at 300 °C this suggests that while the kinetics of neck growth at the lower temperature are not that different from Cu NPs. The mixed nanoparticle films were more resistant to cracking caused by differential sintering. Observation of the film sintered at 300 °C showed large holes and cracks all over the film, although the film was still very conductive suggesting that the differential sintering did not completely destroy the connectivity between the comparatively large dense aggregates. The resistivity results of these Cu/Ag mixtures were consistent with Woo et als results [21], where the resistivity also kept decreasing even after sintering at 325°C.

The microstructure of Cu@Ag NPs films is shown as a function of sintering temperature in Fig 8.6. The first row of micrographs are Cu@Ag NP films sintered at 200, 250 and 300 °C. Cu@Ag NPs films became conductive after sintering at 225 °C. The resistivity of Cu@Ag was 66 $\mu\Omega\times$cm which was lower than the resistivity values for Cu NPs and the mixed NP films

sintered at 250 °C. Actually, it was the lowest resistivity measured for copper containing films in this study and suggested that more neck growth has occurred in this material. Differential sintering and minor crack formation occurred in films sintered at 300°C. It has been reported that the Ag shell can gradually separate from the Cu core on core-shell NPs as the temperature increasing to 250 °C and even higher temperature [52]. This may also be the reason why the resistivity increased to 99 $\mu\Omega\times$cm after the Cu@Ag NPs were sintered at 275°C and eventually reached to 2.4E+3 $\mu\Omega\times$cm at 300 °C. Although, in this study, no direct evidence of this was observed in SEM. Careful observation of the films showed some hollow silver particles and densification of these particles and their shrinkage may also break the interparticle necks and increase resistivity.

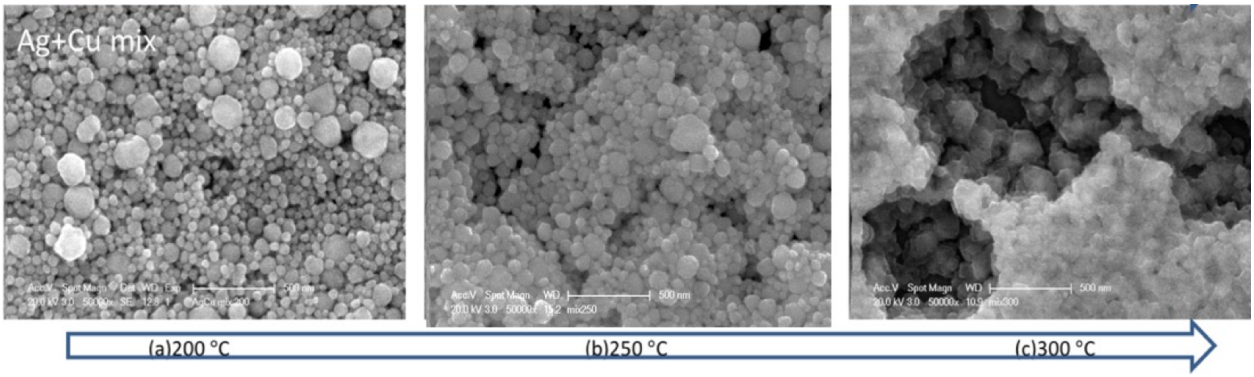

Figure 8.5: Mixture-1 of Ag and Cu NPs sintering process at(a) 200 °C ; (b) 250 °C; (c)300 °C.

Ag (80 nm) NPs films thickness were intentionally controlled to be very similar to the mix-2 films (1.5 um) in Fig.8.7. Compared to Ag (30 nm) films, Ag (80 nm) NPs formed necking above 180 °C and the films became conductive at higher temperature (200°C.) This is consistent with slower necking between the larger Ag particles. The Ag particles also sintered into aggregates at 300°C. and crack appeared in the film. Interestingly the differential sintering did not lead to uncovering of the substrate and connectivity was maintained in the film and the resistivity remained low $\sim$ 96 $\mu\Omega\times$cm. Mix-2 NPs films were not conductive until sintered at 250°C. Therefore, Ag NPs size is thought to be controlling the lowest sintering

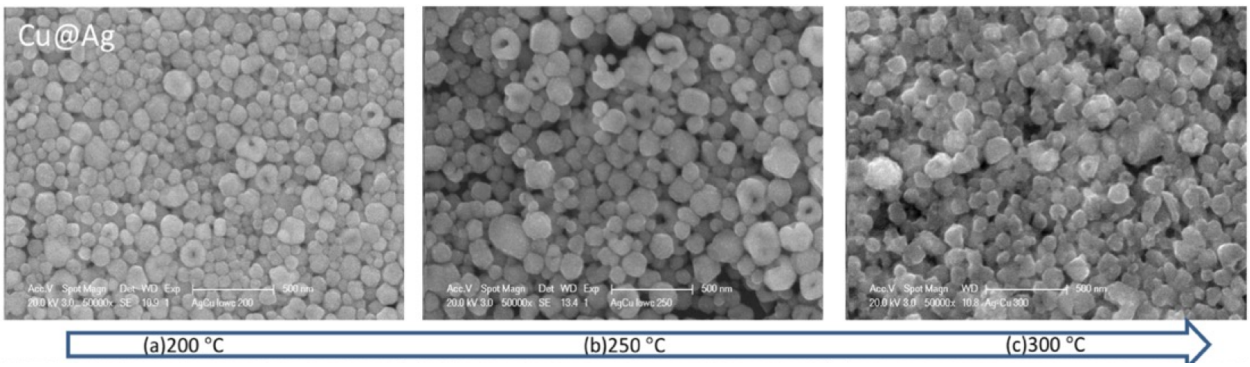

Figure 8.6: Cu@Ag bimetallic NPs sintering process at (a) 200 °C ; (b) 250 °C; (c)300 °C.

temperature in the mixed NP films when the Cu NPs size was fixed. This is thought to be due to the lower surface driving force for Ag NPs (80 nm) than for the smaller Ag NPs (30 nm). Also the smaller sized Ag NPs will more easily fill the interstices among the Cu larger particles [189] leading to more neck formation. Based on the Furnas model [189], Mix-1 would exhibit better sintering behavior at lower temperature because for the larger number of necks. Similar to mix-1 films Fig.8.5, large cracks were observed on the film after annealed at 300 °C as shown in Fig.8.8. In comparison, there were few cracks found in the bimetallic particles films sintered at 300 °C Fig.8.6.

8.1.5 Temperature Dependence of Resistivity

The resistivity of six kinds of metallic NPs films as function of annealing temperature are plotted in Fig. 8.9. Woo et al [21] controlled the particle size and volume ratio of Ag and Cu particles in Ag-Cu particle mixtures and explained the effect on conductivity using the maximum packing density in the bimodal particle system [21]. The Furnace model [189] was proposed to explain the ideal Ag/Cu ratio (1/3) films had higher conductivity than Cu particles films based on the improved packing of the nanoparticles in the film. In this research, we further compared the Ag shell Cu core NPs sintering behavior with the same composition ratio of Ag/Cu mixture NPs, and showed that the Ag shell Cu core NPs exhibited evidence of necking ~200 °C and a relatively low resistivity of 3.45×10^5 $\mu\Omega \times$cm.

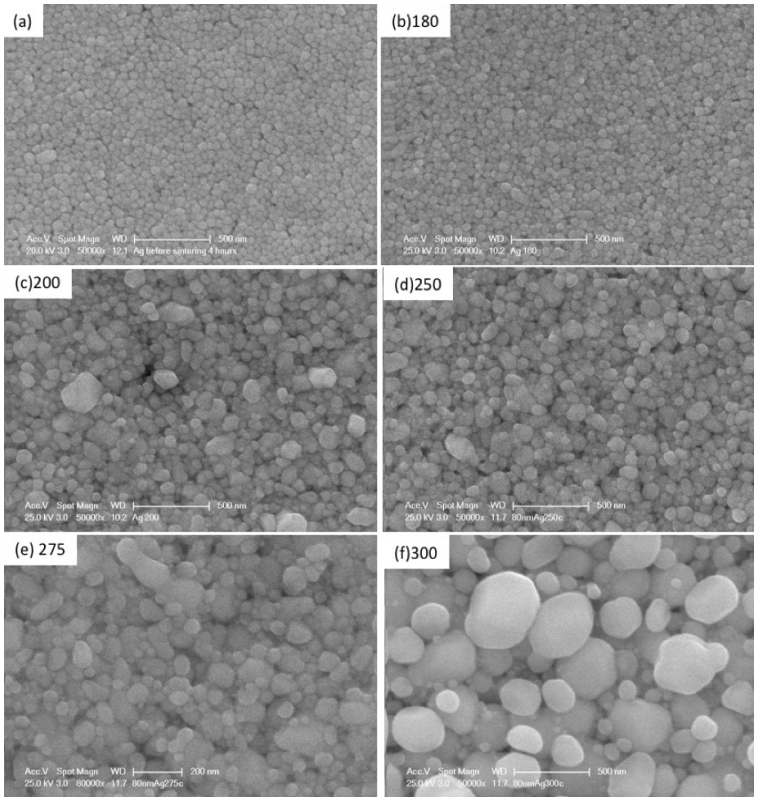

Figure 8.7: Ag NPs (80 nm) sintered in the temperature range from 180 °C to 300 °C

While necking is not thought to have formed at 200 °C for Cu and Ag/Cu mixture particles, since the resistivity for Cu and Ag/Cu mixture NPs films were 2.64x10^9 and 3.55x10^8 $\mu\Omega\times$cm respectively, which were 3 to 4 orders of magnitude larger than that of Ag shell Cu NPs films.

As temperature increasing, neck growth proceeded and Ag shell Cu core NPs reached their lowest resistivity 66.7 $\mu\Omega\times$cm when sintered at 250°C. However, the resistivity for Cu and the mix-1 samples achieved at 250 °C were 442 and 1140 $\mu\Omega\times$cm respectively, which were one order of magnitude larger than that of core shell particle films.

At the higher temperatures, differential sintering occurred for both Cu NPs and Ag shell Cu core NPs when sintered at 300°C resulting in cracking. Hence, the resistivity of Cu and Cu@Ag NPs films increased to 2.28x10^8 $\mu\Omega\times$cm and 2.42x10^4 $\mu\Omega\times$cm respectively. Although the resistivity of Ag/Cu mixture-1 NPs films were still low at 373.9$\mu\Omega\times$cm. Interestingly, the large cracks and large holes observed on the films did not affect the conductivity.

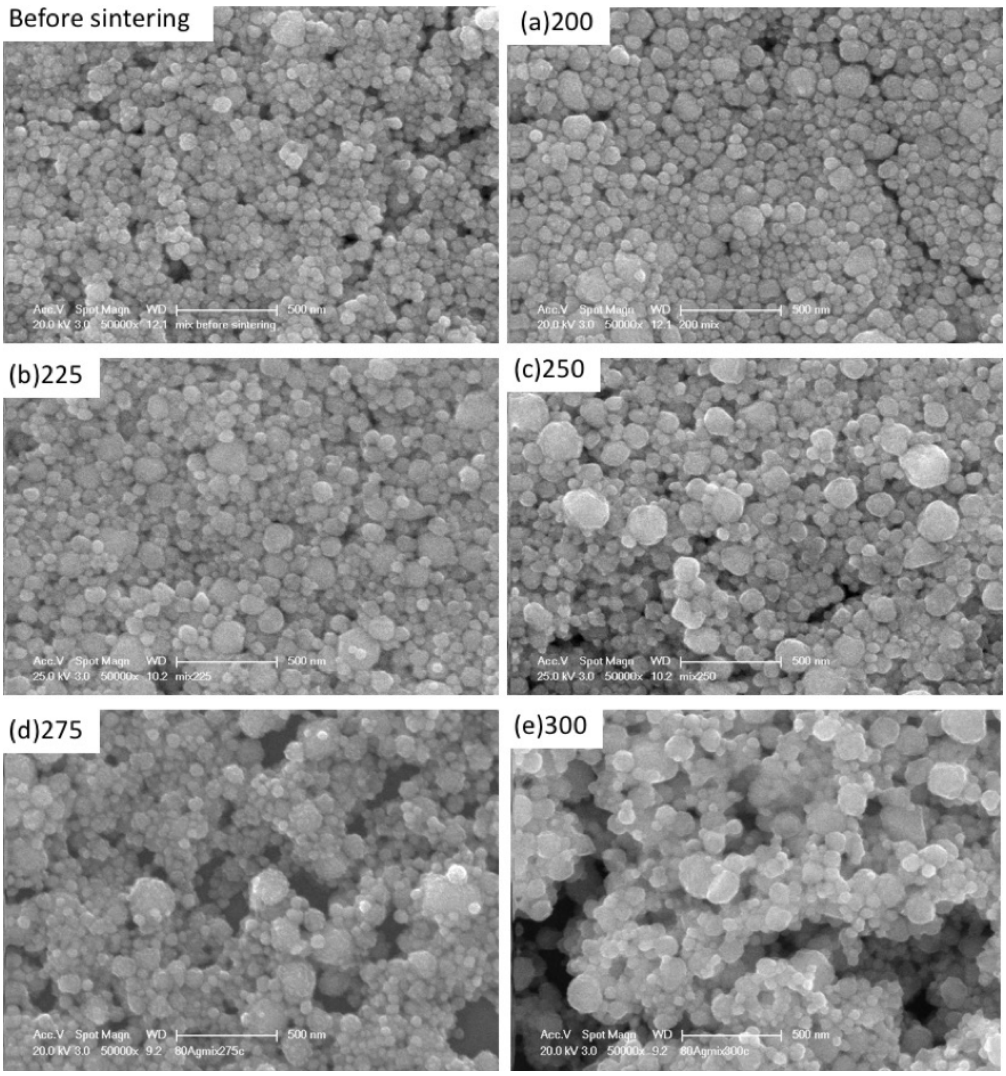

Figure 8.8: Mixture-2 of Ag (80 nm) and Cu (100 nm) sintered in N_2 in the temperature range from 180 °C to 300 °C

Cu@Ag core shell particles did show superior conductivity compared with the similar ratio mixture films containing both small and large Ag NPs particles. Although the Ag (80 nm) particles coarsened and the grain size increased in Fig 8.7, the average resistivity of the Ag films was still low 75.5 $\mu\Omega\times$cm at 300 °C. This is thought to be due to the film thickness which was relatively large (1.5 μm) compared to the Ag NPs (30 nm) films, where isolated aggregates of grains resulted. This did not occur in the thicker film.

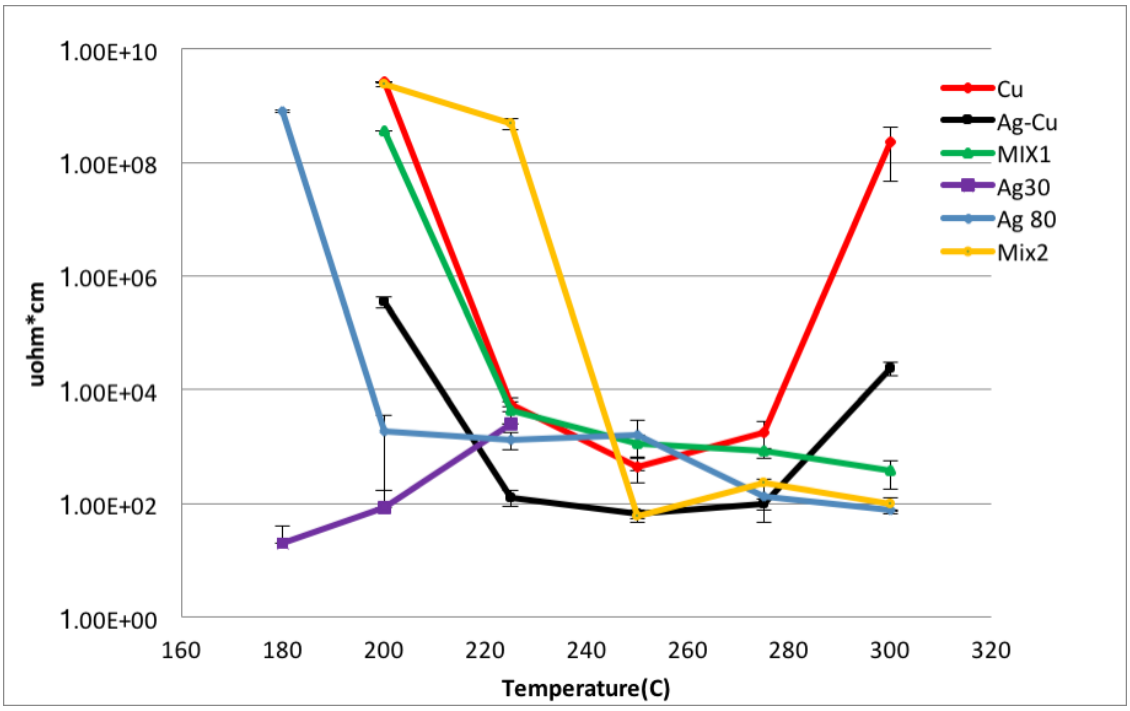

Figure 8.9: Resistivity as a function of temperature, combined with Ag (80 nm), blue; Mix 2, mixture of Ag (80 nm) and Cu NPs (100 nm), yellow

8.1.6 The Advantage of Core-Shell particles sintering

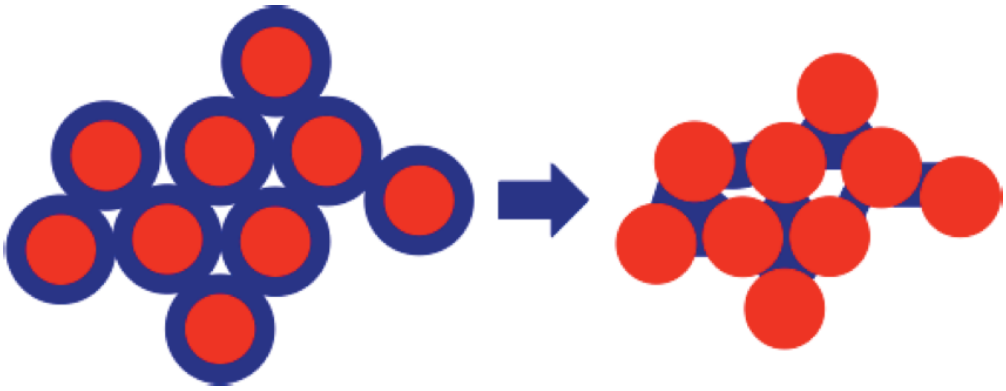

Figure 8.10: A schematic representation of the structure change of the copper-silver core-shell system during sintering. Red - copper, Blue silver [18]

Kim et al reported that Ag necking formed due to the faster diffusion of Ag in the Cu Ag core-shell NPs at 220 °C [190]. The schematic sintering process for core shell structure based on Kim et al experimental result was presented in Fig.8.10 [18, 190]. This is also consistent with the sintering results of this study, where Cu@Ag NPs films exhibited low resistivity 128.8 $\mu\Omega\times$cm at 225 °C. Necks grew at higher temperature, and eventually resulted in differential sintering and small cracks and pores staring to form at 300 °C. Ag with faster diffusivity than Cu is thought to be the reason for the low temperature sintering (<250 °C) of the films. When the temperature increased above 250 °C, Cu core were observed to form necks and became coarsened.

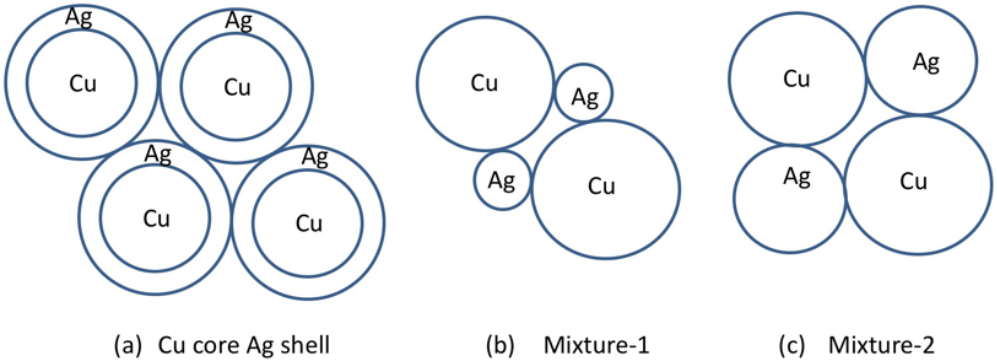

Figure 8.11: Sintering models of (a)Cu core Ag shell NPs, (b) Mix-1 (Ag (30 nm), Cu (100 nm)) ;(c) Mix-2 (Ag (80 nm), Cu (100 nm)

By comparing the schematic diagrams of Cu@Ag, mix-1 and Mix-2 in Fig.8.11, it is easy to appreciate that there should be a higher proportion of Ag-Ag contacts in the core shell particle films compared to the mixed particle films mix-1 and mix-2 in the initial stage of sintering. Therefore, it is thought that Ag-Ag bonds and Ag necks formed first in the core-shell particles and lead to lower resistivity at 200 °C in core shell structures. The slow sintering at low temperature for the mixture NPs could be due to the presence of contacts between copper nanoparticles which suffer from slower neck formation. This would lead to higher resistivity. Therefore, the sintering process for mixture particles were delayed and so was the differential sintering. The large hole and cracks formed along the grain boundaries

could be due to differential sintering between the silver particles. For mix-2 samples (Ag (80 nm) and Cu (100 nm) in 1/3 molar ratio, there will be even fewer Ag-Ag contacts and neck formation at 200 and 225 °C and the resistivity were in the order of 10^9 and 10^8 $\mu\Omega\times$cm.

8.1.7 Summary

In this research, the sintering behavior of Ag core Cu shell NPs, Cu@Ag NPs and the similar phase ratio Ag/Cu NPs mixtures were compared. It was shown that the core shell particle can be sintered at lower temperature (200°C) than films made from Cu or mixture NPs. The lowest resistivity was 66.78 $\mu\Omega\times$cm for the copper core-silver shell nanoparticles sintered at 250°C. It is thought that higher fraction of Ag-Ag contacts and hence necks were formed by the core-shell particles compared to the mixtures in which contacts were formed randomly. This improved the sintering and increased the conductivity of the particles films. The mixtures of Ag/Cu particles sintering relatively slowly due to the lower fraction of Ag/Ag necks and the differential sintering behavior was delayed to 300°C.

9.0 CONCLUSIONS

9.1 NANOPARTICLE SYNTHESIS

Ag-Cu bimetallic nanoparticles were successfully synthesized with one step and two-step method assisted with a microwave reactor.

9.1.1 Bimetallic Nanoparticle One-Pot Synthesis and Characterization

Cu reduction has been greatly increased during the synthesis of Ag-Cu NPs with the assistance of a MW reactor. This method would be advantageous for synthesizing nanoparticle core-shell structures using metals with very different redox potentials. MW synthesized core-shell Ag-Cu NPs are characterized by an inhomogeneous shell that may result from nucleation and growth of Cu satellites on the Ag cores. In contrast, Ag-Cu NPs made in oil bath are thought to have a more homogeneous core shell structure but the reduction rate of Cu was very slow and the expected Ag/Cu ratio was not achieved.

The measured optical absorption of the core-shell NPs synthesized in this study showed high extinction intensity across a broad range of wavelengths compared to mixtures of Cu and Ag NPs and the spectra were significantly influenced by the synthesis conditions. Even though the Cu shell was inhomogeneous, the measured spectra for MW Ag-Cu NPs were found to be similar to the simulated result for 100nm Ag cores with a Cu shell thickness of 10 nm resulting in a Cu/Ag molar ratio of 0.8. Both the experimental results and the simulation showed a broad extinction spectrum with two distinct peaks at 400 nm and 600 nm, instead of a linear sum of the Cu NP extinction spectrum and the Ag NP extinction spectrum. As the shell thickness increases, the local peaks of the optical spectra shift toward higher

wavelength. The broadened extinction and the peak shift for the visible light is thought to result from the hybridization of the surface plasmons at the inner and outer surface of the shell layer.

9.1.2 Bimetallic Nanoparticle Two-Pot Synthesis and Characterization

Cu core-Ag shell NPs

The two pot method increased the reduction of Cu core seeds and also increased the reaction efficiency in the first step. In the second step, the Cu core was reacted with Ag $AgNO_3$ at high temperature, and it was easier to form a core shell structure due to the enhanced deposition of Ag over Cu core at higher reaction temperatures. As the reaction proceeded at lower temperatures, Ag ions were reduced by consuming the Cu core. When the Cu:Ag ratio was 1, galvanic replacement occurred easily. Thus, hollow particles were formed even at very low temperature. In terms of optical properties, Cu core-Ag shell NPs exhibited a merging of extinction peaks, the Ag shell resulted in a dominant peak while the Cu characteristic peak was relatively weak.

Ag core-Cu shell NPs

From studying the Ag@Cu core shell particles synthesis, it was apparent that the use of MW in the second step enhanced the formation of the copper shell. Optical extinction was observed for the entire visible wavelength range for the core-shell structures. Both Ag and Cu NPs characteristic extinction peaks were found in the UV-vis results and the extinction in between was enhanced compared to the mixture of pure Ag and Cu NPs. As the reactant [Cu]/[Ag] molar ratio increased, the characteristic peak of the Cu shell was enhanced. When the size of Ag seeds was increased, its characteristic peak would also shift towards the IR region. This may provide new directions in the design of hybrid metallic NPs with turntable surface plasmon resonance. The visible range absorption could be used as agents for optical imaging [24]

9.2 ANTIBACTERIAL EFFECTS OF METAL NANOPARTICLES

9.2.1 Metallic Nanoparticle Antibacterial Effect

Ag NPs inhibition effect for the Ag resistant strain, Agr-1 mutant was not obvious until the concentration of Ag NPs increased to 50 μM. At 100 to 200 μM the Ag NPs did show a bactericidal effect against the silver resistant mutants. Agr-1 mutant growth was inhibited at 50 μM and the bactericidal effect of Ag NPs was at 100 μM. Without Ag NPs in the media, M. Smegmatis grew 188,800%. Ag NPs inhibited growth of wild type M. Smegmatis MC2 155 above 12.5 μM and a bactericidal effect was achieved above 25 μM. Reduction over the seeded bacteria by 96% was achieved at 100 μM Ag NPs. At 200 μM the Ag NPs were completely bactericidal; no CFUs could be counted.

Cu NPs were as effective against silver resistant mutant as wild type. Cu NPs inhibited the growth of Ag resistant strain, Ag-r1 mutant at 1 mM, the bactericidal effect occurred at 3mM and completely killing at 5 mM. The survival rate of MC2 155 in the concentration of 5mM Cu NPs was 0.3%, while at the same condition it was completely killing for Ag-r1 mutants. When treated with the concentration of 3mM Cu NPs, the survival rate of Ag-r1 was $\sim$133% which is much lower than the 400% survival rate of the wild type. Therefore, the Ag-r1 is more susceptible to Cu NPs than the wild type MC2 155.

The mixed suspensions of Ag NPs and Cu NPs showed an important synergistic antibacterial effect. The bactericidal condition for (Cu(250 μM)/Ag(25 μM)) against silver resistant mutant is about ten times lower than bactericidal condition of Cu NPs (3mM) and four times lower than the bactericidal condition for Ag NPs (100μM). In the mixture of AgNPs and CuNPs, the bactericidal effects (where the ratio of OD (48 hours)/OD (initial) is less than 1) first occurred at Ag NPs=100 μM. When Ag NPs was less than 25 μM, bactericidal effect occurs when the amount of CuNPs was 250 μM. The mixture would also be bactericidal when AgNPs was 6.25 μM if the amount of CuNPs was 625 μM and also when the Ag NPs was 25 μM and Cu NPs was 250 μM (Ag/Cu =10). Considering only the materials costs, this latter case is the most

economic mixture of Ag and Cu NPs applied that achieved a bactericidal effect. Therefore, through comparing the antibacterial effects from different amounts of the pure Ag, Cu and the mixture of Ag and Cu NPs, it was shown that the mixture of Ag and Cu NPs have an enhanced antibacterial effect in aqueous environment.

9.2.2 Inhibition of Biofilm Formation

Pattern of Ag NPs (2.2g/L) spots can inhibit the attachment and colonization of bacteria at AgNP area densities as low as 7.5 %.At 30% Ag NPs area density, the average size of the colony and the total colony area coverage was greatly diminished. As the areal density increased from 7.5% to 30 %, the average size of the colonies decreased from 1716 μm^2 to 423 μm^2.

2D patterning of antibacterial nanoparticles could be used to reduce the amount of silver needed to retard biofilm fouling by manipulating the "killing zones" through the diffusion of silver ions or silver nanoparticles out of the printed nanoparticle spots. Bacteria tended to grow at locations equidistant from the spots. These colonies will eventually form biofilm that will foul the filter. Therefore, fouling will eventually occur for any coating although it may take a much longer period of time. The printed Ag NPs dots are thought to be sources of silver ions or even silver nanoparticles which can diffuse out of the nanoparticle spots into the surrounding wet micro-filter. The released Ag ions or nanoparticles could then directly discourage proliferation of bacteria colonies leading to the zone of killing around the printed spots. The volume for each Ag spots was about 0.02 μL and so the pattern design greatly decreased the total amount of Ag NPs required in antifouling applications compared to covering the entire filter with dilute coatings of AgNPs.

9.2.3 Ion Release from the Nanoparticles

Solubility experiments suggested that Ag ions release from Ag NPs in the NPs mixtures and the bimetallic NPs in deionized water was suppressed by the presence of Cu due to a galvanic effect.The silver ion release and total ion release fit

the first order kinetics model, which is consistent with the results with previews studies [116, 120, 125] The concentration of ions released from bimetallic Ag@Cu NPs and the mixtures after a week was slightly higher than that of Cu NPs. The release constants of Cu, Ag-Cu bimetallic and mixture NPs were close to one another and the release rate is very fast in the first 24 hours and slowing down gradually after one day. The release rate of Ag NPs is slower than that of Cu NPs.

9.2.4 Sintering of Ag Shell Cu Core Nanoparticle

Cu core Ag shell nanoparticles sintered at lower temperature (200 °C) and achieved the lowest resistivity of 66.78 $\mu\Omega\times$cm comparted to films made from Cu NPs or mixtures of Cu-NPs and Ag NPs. Cu core Ag shell thin films showed a superior electrical conductivity after sintered at low temperature, (200 °C to 275 °C) , for one hour under N_2 atmosphere when compared to Cu NPs and the same molar ratio mixture of Ag NPs (30 nm) and Cu NPs (100 nm). The reduced resistivity is consistent with enhanced necking due to the higher higher fraction of Ag-Ag contacts for the Ag shell Cu core NPs. This improved the sintering and increased the conductivity of the particles films.

10.0 FUTURE WORK

Synthesis of bimetallic nanoparticle using microwave reactors for high yield and uniform core-shell structures is one area for future study. A systematic study of microwave assisted reactions should be undertaken using different combinations of reagents, reducing agents as well as stabilizers and reaction temperature. Also by experimenting with different reaction ratios and temperatures it may be possible to control the core-shell structures and optical absorption of Cu-Ag nanoparticles. Based on the superior conductivity after sintered at temperature as low as 200 °C, bimetallic core-shell particles might be used to enhance the conductivity of silver-copper nanoparticle interconnects after low temperature heat treatment.

The antibacterial efficacy of bimetallic nanoparticle as well as the mixture of Cu and Ag nanoparticles could also be very important in controlling silver resistant bacteria. This study has shown that mixtures of Cu and Ag nanoparticles did shown enhanced antibacterial efficiency compared to pure Ag or pure Cu nanoparticle. However, due to the galvanic effects, few silver ions are released into aqueous suspensions and most of the ion release is thought to be copper. The enhanced efficacy of the mixtures could be associated with enhanced release of copper ions due to the galvanic effect or due to direct contact of NPs with the bacterial cell wall, reacting with the bio-ligands on the cell wall and eventually deactivating the bacteria. Planktonic experiments should be undertaken to test the antibacterial effects of bimetallic nanoparticles. In addition antibacterial particles made up of copper oxide and silver may release both copper and silver ions into solution without the galvanic effect suppressing the release of silver ions.

Ag hollow nanoparticle have also been synthesized in this work and it would be interesting to test the antibacterial effects of Ag hollow nanoparticle to compare with the Ag sphere

particles. The Ag hollow nanoparticle would have a higher surface area to volume ratio than solid Ag spheres particles and could therefore release more silver ions into solution and show enhanced efficacy for a given mass of silver.

Inkjet printing may provide a processing method for controlled deposition of antifouling nanoparticle treatments for filters. This will involve deposited spots of high antibacterial nanoparticle concentration surrounded by a "zone of killing" formed by the diffusion of silver ions of Ag NPs out from the spots. Individual bacteria will be killed or inactivated in this zone before colony formation. Hence the location and size of bacterial colonies can be controlled by patterning small amounts of antibacterial nanoparticles. The size of the spots and the mass on nanoparticles in each spot could be manipulated to maximize the efficacy of the nanoparticle spots and reduce the amount of silver required to protect the filter. Flow cell experiments would be required to directly test the effects on fouling.

BIBLIOGRAPHY

[1] G. Barcaro, A. Fortunelli, G. Rossi, F. Nita, and R. Ferrando, "Electronic and structural shell closure in agcu and aucu nanoclusters," *The Journal of Physical Chemistry B*, vol. 110, no. 46, pp. 23197–23203, 2006.

[2] S. Nunez and R. Johnston, "Structures and chemical ordering of small cu- ag clusters," *The Journal of Physical Chemistry C*, vol. 114, no. 31, pp. 13255–13266, 2010.

[3] H. Jiang, K.-s. Moon, and C. Wong, "Synthesis of ag-cu alloy nanoparticles for lead-free interconnect materials," in *Advanced Packaging Materials: Processes, Properties and Interfaces, 2005. Proceedings. International Symposium on*, pp. 173–177, IEEE, 2005.

[4] N. Dimitratos, J. K. Edwards, C. J. Kiely, and G. J. Hutchings, "Gold catalysis: helping create a sustainable future," *Applied Petrochemical Research*, vol. 2, no. 1-2, pp. 7–14, 2012.

[5] C. Langlois, Z. Wang, D. Pearmain, C. Ricolleau, and Z. Li, "Haadf-stem imaging of cuag core-shell nanoparticles," in *Journal of Physics: Conference Series*, vol. 241, p. 012043, IOP Publishing, 2010.

[6] P. Stoodley, K. Sauer, D. Davies, and J. W. Costerton, "Biofilms as complex differentiated communities," *Annual Reviews in Microbiology*, vol. 56, no. 1, pp. 187–209, 2002.

[7] Z.-m. Xiu, Q.-b. Zhang, H. L. Puppala, V. L. Colvin, and P. J. Alvarez, "Negligible particle-specific antibacterial activity of silver nanoparticles," *Nano letters*, vol. 12, no. 8, pp. 4271–4275, 2012.

[8] G. Grass, C. Rensing, and M. Solioz, "Metallic copper as an antimicrobial surface," *Applied and environmental microbiology*, vol. 77, no. 5, pp. 1541–1547, 2011.

[9] J. Park and J. Moon, "Control of colloidal particle deposit patterns within picoliter droplets ejected by ink-jet printing," *Langmuir*, vol. 22, no. 8, pp. 3506–3513, 2006.

[10] R. D. Deegan, O. Bakajin, T. F. Dupont, G. Huber, S. R. Nagel, and T. A. Witten, "Capillary flow as the cause of ring stains from dried liquid drops," *Nature*, vol. 389, no. 6653, pp. 827–829, 1997.

[11] T. A. Dankovich and D. G. Gray, "Bactericidal paper impregnated with silver nanoparticles for point-of-use water treatment," *Environmental science & technology*, vol. 45, no. 5, pp. 1992–1998, 2011.

[12] S. K. Misra, A. Dybowska, D. Berhanu, S. N. Luoma, and E. Valsami-Jones, "The complexity of nanoparticle dissolution and its importance in nanotoxicological studies," *Science of the total environment*, vol. 438, pp. 225–232, 2012.

[13] R. L. Coble, "Sintering crystalline solids. i. intermediate and final state diffusion models," *Journal of applied physics*, vol. 32, no. 5, pp. 787–792, 1961.

[14] J. Xiong, Y. Wang, Q. Xue, and X. Wu, "Synthesis of highly stable dispersions of nanosized copper particles using l-ascorbic acid," *Green Chemistry*, vol. 13, no. 4, pp. 900–904, 2011.

[15] M. Tsai, W.-S. Hwang, H. Chou, and P. Hsieh, "Effects of pulse voltage on inkjet printing of a silver nanopowder suspension," *Nanotechnology*, vol. 19, no. 33, p. 335304, 2008.

[16] C. Larimer, M. S. Islam, A. Ojha, and I. Nettleship, "Mutation of environmental mycobacteria to resist silver nanoparticles also confers resistance to a common antibiotic," *Biometals*, vol. 27, no. 4, pp. 695–702, 2014.

[17] Y. Sun, B. Mayers, and Y. Xia, "Metal nanostructures with hollow interiors," *Advanced Materials*, vol. 15, no. 7-8, pp. 641–646, 2003.

[18] M. J. Kammer, "Technology, science, and environtmental impact of a novel cu-ag core-shell solderless interconnect system," 2014.

[19] N. Toshima and T. Yonezawa, "Bimetallic nanoparticles-novel materials for chemical and physical applications," *New J. Chem.*, vol. 22, pp. 1179–1201, 1998.

[20] W. Li, W. Li, M. Wang, G. Liu, and M. Chen, "Direct writing of stable cu-ag-based conductive patterns for flexible electronics," *RSC Adv.*, vol. 6, pp. 10670–10676, 2016.

[21] K. Woo, D. Kim, J. S. Kim, S. Lim, and J. Moon, "Ink-jet printing of cu- ag-based highly conductive tracks on a transparent substrate," *Langmuir*, vol. 25, no. 1, pp. 429–433, 2008.

[22] M. B. Cortie and A. M. McDonagh, "Synthesis and optical properties of hybrid and alloy plasmonic nanoparticles," *Chemical reviews*, vol. 111, no. 6, pp. 3713–3735, 2011.

[23] L. Zhang, D. A. Blom, and H. Wang, "Au–cu2o core–shell nanoparticles:a hybrid metal-semiconductor heteronanostructure with geometrically tunable optical properties," *Chemistry of Materials*, vol. 23, no. 20, pp. 4587–4598, 2011.

[24] S. E. Skrabalak, J. Chen, Y. Sun, X. Lu, L. Au, C. M. Cobley, and Y. Xia, "Gold nanocages: synthesis, properties, and applications," *Accounts of chemical research*, vol. 41, no. 12, pp. 1587–1595, 2008.

[25] J. H. Noh, S. H. Im, J. H. Heo, T. N. Mandal, and S. I. Seok, "Chemical management for colorful, efficient, and stable inorganic–organic hybrid nanostructured solar cells," *Nano letters*, vol. 13, no. 4, pp. 1764–1769, 2013.

[26] F. Wang, Y. Han, C. S. Lim, Y. Lu, J. Wang, J. Xu, H. Chen, C. Zhang, M. Hong, and X. Liu, "Simultaneous phase and size control of upconversion nanocrystals through lanthanide doping," *Nature*, vol. 463, no. 7284, pp. 1061–1065, 2010.

[27] M. Tsuji, S. Hikino, R. Tanabe, M. Matsunaga, and Y. Sano, "Syntheses of ag/cu alloy and ag/cu alloy core cu shell nanoparticles using a polyol method," *CrystEngComm*, vol. 12, no. 11, pp. 3900–3908, 2010.

[28] N. Cioffi, L. Torsi, N. Ditaranto, G. Tantillo, L. Ghibelli, L. Sabbatini, T. Bleve-Zacheo, M. D'Alessio, P. G. Zambonin, and E. Traversa, "Copper nanoparticle/polymer composites with antifungal and bacteriostatic properties," *Chemistry of Materials*, vol. 17, no. 21, pp. 5255–5262, 2005.

[29] K. S. Tan and K. Y. Cheong, "Advances of ag, cu, and ag–cu alloy nanoparticles synthesized via chemical reduction route," *Journal of nanoparticle research*, vol. 15, no. 4, p. 1537, 2013.

[30] R. Ferrando, J. Jellinek, and R. L. Johnston, "Nanoalloys: from theory to applications of alloy clusters and nanoparticles," *Chemical reviews*, vol. 108, no. 3, pp. 845–910, 2008.

[31] C. B. Murray, S. Sun, W. Gaschler, H. Doyle, T. A. Betley, and C. R. Kagan, "Colloidal synthesis of nanocrystals and nanocrystal superlattices," *IBM Journal of Research and Development*, vol. 45, no. 1, pp. 47–56, 2001.

[32] J. A. Creighton, C. G. Blatchford, and M. G. Albrecht, "Plasma resonance enhancement of raman scattering by pyridine adsorbed on silver or gold sol particles of size comparable to the excitation wavelength," *Journal of the Chemical Society, Faraday Transactions 2: Molecular and Chemical Physics*, vol. 75, pp. 790–798, 1979.

[33] I. Sondi, D. V. Goia, and E. Matijević, "Preparation of highly concentrated stable dispersions of uniform silver nanoparticles," *Journal of colloid and interface science*, vol. 260, no. 1, pp. 75–81, 2003.

[34] N. R. Jana, L. Gearheart, C. J. Murphy, *et al.*, "Seed-mediated growth approach for shape-controlled synthesis of spheroidal and rod-like gold nanoparticles using a surfactant template," *Advanced Materials*, vol. 13, no. 18, p. 1389, 2001.

[35] L. Suber, I. Sondi, E. Matijević, and D. V. Goia, "Preparation and the mechanisms of formation of silver particles of different morphologies in homogeneous solutions," *Journal of Colloid and Interface Science*, vol. 288, no. 2, pp. 489–495, 2005.

[36] A. Zielińska, E. Skwarek, A. Zaleska, M. Gazda, and J. Hupka, "Preparation of silver nanoparticles with controlled particle size," *Procedia Chemistry*, vol. 1, no. 2, pp. 1560–1566, 2009.

[37] F. Fievet, J. Lagier, and M. Figlarz, "Preparing monodisperse metal powders in micrometer and submicrometer sizes by the polyol process," *Mrs Bulletin*, vol. 14, no. 12, pp. 29–34, 1989.

[38] F. Fievet, J. Lagier, B. Blin, B. Beaudoin, and M. Figlarz, "Homogeneous and heterogeneous nucleations in the polyol process for the preparation of micron and submicron size metal particles," *Solid State Ionics*, vol. 32, pp. 198–205, 1989.

[39] G. Viau, F. Fievet-Vincent, and F. Fievet, "Nucleation and growth of bimetallic coni and feni monodisperse particles prepared in polyols," *Solid State Ionics*, vol. 84, no. 3-4, pp. 259–270, 1996.

[40] F. Bonet, V. Delmas, S. Grugeon, R. H. Urbina, P. Silvert, and K. Tekaia-Elhsissen, "Synthesis of monodisperse au, pt, pd, ru and ir nanoparticles in ethylene glycol," *Nanostructured Materials*, vol. 11, no. 8, pp. 1277–1284, 1999.

[41] B. Wiley, T. Herricks, Y. Sun, and Y. Xia, "Polyol synthesis of silver nanoparticles: use of chloride and oxygen to promote the formation of single-crystal, truncated cubes and tetrahedrons," *Nano Letters*, vol. 4, no. 9, pp. 1733–1739, 2004.

[42] A. R. Siekkinen, J. M. McLellan, J. Chen, and Y. Xia, "Rapid synthesis of small silver nanocubes by mediating polyol reduction with a trace amount of sodium sulfide or sodium hydrosulfide," *Chemical physics letters*, vol. 432, no. 4, pp. 491–496, 2006.

[43] A. Henglein, T. Linnert, and P. Mulvaney, "Reduction of ag+ in aqueous polyanion solution: Some properties and reactions of long-lived oligomeric silver clusters and metallic silver particles," *Berichte der Bunsengesellschaft für physikalische Chemie*, vol. 94, no. 12, pp. 1449–1457, 1990.

[44] Q.-m. LIU, D.-b. ZHOU, Y. Yamamoto, R. Ichino, and M. Okido, "Preparation of cu nanoparticles with nabh4 by aqueous reduction method," *Transactions of Nonferrous Metals Society of China*, vol. 22, no. 1, pp. 117–123, 2012.

[45] L. Chen, D. Zhang, J. Chen, H. Zhou, and H. Wan, "The use of ctab to control the size of copper nanoparticles and the concentration of alkylthiols on their surfaces," *Materials Science and Engineering: A*, vol. 415, no. 1, pp. 156–161, 2006.

[46] T. M. D. Dang, T. T. T. Le, E. Fribourg-Blanc, and M. C. Dang, "Synthesis and optical properties of copper nanoparticles prepared by a chemical reduction method," *Advances in Natural Sciences: Nanoscience and Nanotechnology*, vol. 2, no. 1, p. 015009, 2011.

[47] J. Ramyadevi, K. Jeyasubramanian, A. Marikani, G. Rajakumar, and A. A. Rahuman, "Synthesis and antimicrobial activity of copper nanoparticles," *Materials Letters*, vol. 71, pp. 114–116, 2012.

[48] Z. Zhang, B. Zhao, and L. Hu, "Pvp protective mechanism of ultrafine silver powder synthesized by chemical reduction processes," *Journal of Solid State Chemistry*, vol. 121, no. 1, pp. 105–110, 1996.

[49] K.-S. Chou and C.-Y. Ren, "Synthesis of nanosized silver particles by chemical reduction method," *Materials Chemistry and Physics*, vol. 64, no. 3, pp. 241–246, 2000.

[50] I. Pastoriza-Santos, D. S. Koktysh, A. A. Mamedov, M. Giersig, N. A. Kotov, and L. M. Liz-Marzán, "One-pot synthesis of ag@ tio2 core- shell nanoparticles and their layer-by-layer assembly," *Langmuir*, vol. 16, no. 6, pp. 2731–2735, 2000.

[51] J. Belloni, M. Mostafavi, H. Remita, J.-L. Marignier, and M.-O. Delcourt, "Radiation-induced synthesis of mono-and multi-metallic clusters and nanocolloids," *New Journal of Chemistry*, vol. 22, no. 11, pp. 1239–1255, 1998.

[52] M. Grouchko, A. Kamyshny, and S. Magdassi, "Formation of air-stable copper–silver core–shell nanoparticles for inkjet printing," *Journal of Materials Chemistry*, vol. 19, no. 19, pp. 3057–3062, 2009.

[53] A. Muzikansky, P. Nanikashvili, J. Grinblat, and D. Zitoun, "Ag dewetting in cu@ ag monodisperse core–shell nanoparticles," *The Journal of Physical Chemistry C*, vol. 117, no. 6, pp. 3093–3100, 2013.

[54] M. Tsuji, S. Hikino, Y. Sano, and M. Horigome, "Preparation of cu@ ag core–shell nanoparticles using a two-step polyol process under bubbling of n2 gas," *Chemistry letters*, vol. 38, no. 6, pp. 518–519, 2009.

[55] S. Horikoshi and N. Serpone, *Microwaves in nanoparticle synthesis: fundamentals and applications*. John Wiley & Sons, 2013.

[56] N. N. Mallikarjuna and R. S. Varma, "Microwave-assisted shape-controlled bulk synthesis of noble nanocrystals and their catalytic properties," *Crystal growth & design*, vol. 7, no. 4, pp. 686–690, 2007.

[57] I. Bilecka and M. Niederberger, "Microwave chemistry for inorganic nanomaterials synthesis," *Nanoscale*, vol. 2, no. 8, pp. 1358–1374, 2010.

[58] O. Akhavan, M. Abdolahad, Y. Abdi, and S. Mohajerzadeh, "Silver nanoparticles within vertically aligned multi-wall carbon nanotubes with open tips for antibacterial purposes," *Journal of Materials Chemistry*, vol. 21, no. 2, pp. 387–393, 2011.

[59] M. Chen, X. Wang, Y. Yu, Z. Pei, X. Bai, C. Sun, R. Huang, and L. Wen, "X-ray photoelectron spectroscopy and auger electron spectroscopy studies of al-doped zno films," *Applied Surface Science*, vol. 158, no. 1, pp. 134–140, 2000.

[60] B. V. Crist, "Handbook of monochromatic xps spectra, the elements of native oxides," *Handbook of Monochromatic XPS Spectra, The Elements of Native Oxides, by B. Vincent Crist, pp. 548. ISBN 0-471-49265-5. Wiley-VCH, October 2000.*, vol. 1, 2000.

[61] L.-Q. Mai, A. Minhas-Khan, X. Tian, K. M. Hercule, Y.-L. Zhao, X. Lin, and X. Xu, "Synergistic interaction between redox-active electrolyte and binder-free functionalized carbon for ultrahigh supercapacitor performance," *Nature communications*, vol. 4, 2013.

[62] U. N. D. Programme, *The Human Development Report*. Human Development Report, 1999.

[63] T. P. Primm, C. A. Lucero, and J. O. Falkinham, "Health impacts of environmental mycobacteria," *Clinical microbiology reviews*, vol. 17, no. 1, pp. 98–106, 2004.

[64] M. J. Tobin-DAngelo, M. A. Blass, C. del Rio, J. S. Halvosa, H. M. Blumberg, and C. R. Horsburgh, "Hospital water as a source of mycobacterium avium complex isolates in respiratory specimens," *Journal of Infectious Diseases*, vol. 189, no. 1, pp. 98–104, 2004.

[65] M. Rodgers, B. Blackstone, A. Reyes, and T. Covert, "Colonisation of point of use water filters by silver resistant non-tuberculous mycobacteria.," *Journal of clinical pathology*, vol. 52, no. 8, p. 629, 1999.

[66] J. Falkinham Iii, "Surrounded by mycobacteria: nontuberculous mycobacteria in the human environment," *Journal of applied microbiology*, vol. 107, no. 2, pp. 356–367, 2009.

[67] A. J. Huh and Y. J. Kwon, "nanoantibiotics: a new paradigm for treating infectious diseases using nanomaterials in the antibiotics resistant era," *Journal of Controlled Release*, vol. 156, no. 2, pp. 128–145, 2011.

[68] D. H. Nies, "Microbial heavy-metal resistance," *Applied microbiology and biotechnology*, vol. 51, no. 6, pp. 730–750, 1999.

[69] M. J. Hajipour, K. M. Fromm, A. A. Ashkarran, D. J. de Aberasturi, I. R. de Larramendi, T. Rojo, V. Serpooshan, W. J. Parak, and M. Mahmoudi, "Antibacterial

properties of nanoparticles," *Trends in biotechnology*, vol. 30, no. 10, pp. 499–511, 2012.

[70] U. Szewzyk, R. Szewzyk, W. Manz, and K.-H. Schleifer, "Microbiological safety of drinking water," *Annual Reviews in Microbiology*, vol. 54, no. 1, pp. 81–127, 2000.

[71] L. M. Feazel, L. K. Baumgartner, K. L. Peterson, D. N. Frank, J. K. Harris, and N. R. Pace, "Opportunistic pathogens enriched in showerhead biofilms," *Proceedings of the National Academy of Sciences*, vol. 106, no. 38, pp. 16393–16399, 2009.

[72] T. P. Stinear, T. Seemann, P. F. Harrison, G. A. Jenkin, J. K. Davies, P. D. Johnson, Z. Abdellah, C. Arrowsmith, T. Chillingworth, C. Churcher, *et al.*, "Insights from the complete genome sequence of mycobacterium marinum on the evolution of mycobacterium tuberculosis," *Genome research*, vol. 18, no. 5, pp. 729–741, 2008.

[73] S. Gupta, S. B. Pandit, N. Srinivasan, and D. Chatterji, "Proteomics analysis of carbon-starved mycobacterium smegmatis: induction of dps-like protein," *Protein engineering*, vol. 15, no. 6, pp. 503–511, 2002.

[74] R. H. Taylor, J. O. Falkinham, C. D. Norton, and M. W. LeChevallier, "Chlorine, chloramine, chlorine dioxide, and ozone susceptibility of mycobacterium avium," *Applied and Environmental Microbiology*, vol. 66, no. 4, pp. 1702–1705, 2000.

[75] C. Le Dantec, J.-P. Duguet, A. Montiel, N. Dumoutier, S. Dubrou, and V. Vincent, "Chlorine disinfection of atypical mycobacteria isolated from a water distribution system," *Applied and environmental microbiology*, vol. 68, no. 3, pp. 1025–1032, 2002.

[76] L. L. Silver, "Challenges of antibacterial discovery," *Clinical microbiology reviews*, vol. 24, no. 1, pp. 71–109, 2011.

[77] K. Mijnendonckx, N. Leys, J. Mahillon, S. Silver, and R. Van Houdt, "Antimicrobial silver: uses, toxicity and potential for resistance," *Biometals*, vol. 26, no. 4, pp. 609–621, 2013.

[78] L. Hall-Stoodley, J. W. Costerton, and P. Stoodley, "Bacterial biofilms: from the natural environment to infectious diseases," *Nature reviews microbiology*, vol. 2, no. 2, pp. 95–108, 2004.

[79] J. W. Costerton, Z. Lewandowski, D. E. Caldwell, D. R. Korber, and H. M. Lappin-Scott, "Microbial biofilms," *Annual Reviews in Microbiology*, vol. 49, no. 1, pp. 711–745, 1995.

[80] T. J. Beveridge, S. A. Makin, J. L. Kadurugamuwa, and Z. Li, "Interactions between biofilms and the environment," *FEMS Microbiology Reviews*, vol. 20, no. 3-4, pp. 291–303, 1997.

[81] G. O'Toole, H. B. Kaplan, and R. Kolter, "Biofilm formation as microbial development," *Annual Reviews in Microbiology*, vol. 54, no. 1, pp. 49–79, 2000.

[82] J. M. ten Cate, "Biofilms, a new approach to the microbiology of dental plaque," *Odontology*, vol. 94, no. 1, pp. 1–9, 2006.

[83] A. G. Gristina, P. T. Naylor, and Q. N. Myrvik, "Biomaterial-centered infections: microbial adhesion versus tissue integration," in *Pathogenesis of Wound and Biomaterial-Associated Infections*, pp. 193–216, Springer, 1990.

[84] J. N. Anderl, J. Zahller, F. Roe, and P. S. Stewart, "Role of nutrient limitation and stationary-phase existence in klebsiella pneumoniae biofilm resistance to ampicillin and ciprofloxacin," *Antimicrobial agents and chemotherapy*, vol. 47, no. 4, pp. 1251–1256, 2003.

[85] J. J. Harrison, H. Ceri, and R. J. Turner, "Multimetal resistance and tolerance in microbial biofilms," *Nature Reviews Microbiology*, vol. 5, no. 12, pp. 928–938, 2007.

[86] T. M. Benn and P. Westerhoff, "Nanoparticle silver released into water from commercially available sock fabrics," *Environmental science & technology*, vol. 42, no. 11, pp. 4133–4139, 2008.

[87] S. Silver, L. T. Phung, and G. Silver, "Silver as biocides in burn and wound dressings and bacterial resistance to silver compounds," *Journal of Industrial Microbiology and Biotechnology*, vol. 33, no. 7, pp. 627–634, 2006.

[88] P. Jain and T. Pradeep, "Potential of silver nanoparticle-coated polyurethane foam as an antibacterial water filter," *Biotechnology and bioengineering*, vol. 90, no. 1, pp. 59–63, 2005.

[89] P. T. Nicholson and I. Shaw, *Ancient Egyptian materials and technology*. Cambridge University Press, 2000.

[90] J. P. Ruparelia, A. K. Chatterjee, S. P. Duttagupta, and S. Mukherji, "Strain specificity in antimicrobial activity of silver and copper nanoparticles," *Acta biomaterialia*, vol. 4, no. 3, pp. 707–716, 2008.

[91] S. Pal, Y. K. Tak, and J. M. Song, "Does the antibacterial activity of silver nanoparticles depend on the shape of the nanoparticle? a study of the gram-negative bacterium escherichia coli," *Applied and environmental microbiology*, vol. 73, no. 6, pp. 1712–1720, 2007.

[92] R. Brayner, R. Ferrari-Iliou, N. Brivois, S. Djediat, M. F. Benedetti, and F. Fiévet, "Toxicological impact studies based on escherichia coli bacteria in ultrafine zno nanoparticles colloidal medium," *Nano Letters*, vol. 6, no. 4, pp. 866–870, 2006.

[93] Y. Xie, Y. He, P. L. Irwin, T. Jin, and X. Shi, "Antibacterial activity and mechanism of action of zinc oxide nanoparticles against campylobacter jejuni," *Applied and environmental microbiology*, vol. 77, no. 7, pp. 2325–2331, 2011.

[94] M.-C. Daniel and D. Astruc, "Gold nanoparticles: assembly, supramolecular chemistry, quantum-size-related properties, and applications toward biology, catalysis, and nanotechnology," *Chemical reviews*, vol. 104, no. 1, pp. 293–346, 2004.

[95] K. R. Raghupathi, R. T. Koodali, and A. C. Manna, "Size-dependent bacterial growth inhibition and mechanism of antibacterial activity of zinc oxide nanoparticles," *Langmuir*, vol. 27, no. 7, pp. 4020–4028, 2011.

[96] A. K. Chatterjee, R. Chakraborty, and T. Basu, "Mechanism of antibacterial activity of copper nanoparticles," *Nanotechnology*, vol. 25, no. 13, p. 135101, 2014.

[97] J. S. Kim, A. Adamcakova-Dodd, P. T O'Shaughnessy, V. H. Grassian, and P. S. Thorne, "Effects of copper nanoparticle exposure on host defense in a murine pulmonary infection model," *Particle and fibre toxicology*, vol. 8, no. 1, p. 29, 2011.

[98] H. L. Karlsson, P. Cronholm, J. Gustafsson, and L. Moller, "Copper oxide nanoparticles are highly toxic: a comparison between metal oxide nanoparticles and carbon nanotubes," *Chemical research in toxicology*, vol. 21, no. 9, pp. 1726–1732, 2008.

[99] J. P. Mason, S. K. Sebree, and T. L. Quinn, *Monitoring-well network and sampling design for ground-water quality, Wind River Indian Reservation, Wyoming*. US Department of the Interior, US Geological Survey, 2005.

[100] O. Bondarenko, K. Juganson, A. Ivask, K. Kasemets, M. Mortimer, and A. Kahru, "Toxicity of ag, cuo and zno nanoparticles to selected environmentally relevant test organisms and mammalian cells in vitro: a critical review," *Archives of toxicology*, vol. 87, no. 7, pp. 1181–1200, 2013.

[101] R. Bhardwaj, X. Fang, and D. Attinger, "Pattern formation during the evaporation of a colloidal nanoliter drop: a numerical and experimental study," *New Journal of Physics*, vol. 11, no. 7, p. 075020, 2009.

[102] A. P. Sommer, "Limits of the impact of gravity on self-organizing nanospheres," *The Journal of Physical Chemistry B*, vol. 108, no. 24, pp. 8096–8098, 2004.

[103] H. Wei, Z. Wang, J. Zhang, S. House, Y.-G. Gao, L. Yang, H. Robinson, L. H. Tan, H. Xing, C. Hou, *et al.*, "Time-dependent, protein-directed growth of gold nanoparticles within a single crystal of lysozyme," *Nature nanotechnology*, vol. 6, no. 2, pp. 93–97, 2011.

[104] L. Huang, X. Cui, G. Dukovic, and S. P. OBrien, "Self-organizing high-density single-walled carbon nanotube arrays from surfactant suspensions," *Nanotechnology*, vol. 15, no. 11, p. 1450, 2004.

[105] I. I. Smalyukh, O. V. Zribi, J. C. Butler, O. D. Lavrentovich, and G. C. Wong, "Structure and dynamics of liquid crystalline pattern formation in drying droplets of dna," *Physical review letters*, vol. 96, no. 17, p. 177801, 2006.

[106] P. G. De Gennes, "Solvent evaporation of spin cast films:crust effects," *The European Physical Journal E*, vol. 7, no. 1, pp. 31–34, 2002.

[107] D. Brutin, B. Sobac, B. Loquet, and J. Sampol, "Pattern formation in drying drops of blood," *Journal of fluid mechanics*, vol. 667, pp. 85–95, 2011.

[108] H. Hu and R. G. Larson, "Marangoni effect reverses coffee-ring depositions," *The Journal of Physical Chemistry B*, vol. 110, no. 14, pp. 7090–7094, 2006.

[109] H. Hu and R. G. Larson, "Analysis of the effects of marangoni stresses on the microflow in an evaporating sessile droplet," *Langmuir*, vol. 21, no. 9, pp. 3972–3980, 2005.

[110] N. Kumar, K. Varanasi, R. D. Tilton, and S. Garoff, "Surfactant self-assembly ahead of the contact line on a hydrophobic surface and its implications for wetting," *Langmuir*, vol. 19, no. 13, pp. 5366–5373, 2003.

[111] M. A. Aegerter and M. Mennig, *Sol-gel technologies for glass producers and users*. Springer Science & Business Media, 2013.

[112] S.-W. Hwang, H. Tao, D.-H. Kim, H. Cheng, J.-K. Song, E. Rill, M. A. Brenckle, B. Panilaitis, S. M. Won, Y.-S. Kim, *et al.*, "A physically transient form of silicon electronics," *Science*, vol. 337, no. 6102, pp. 1640–1644, 2012.

[113] F. C. Krebs, "Fabrication and processing of polymer solar cells: a review of printing and coating techniques," *Solar energy materials and solar cells*, vol. 93, no. 4, pp. 394–412, 2009.

[114] X. Cui and T. Boland, "Human microvasculature fabrication using thermal inkjet printing technology," *Biomaterials*, vol. 30, no. 31, pp. 6221–6227, 2009.

[115] Y. Lee, J.-r. Choi, K. J. Lee, N. E. Stott, and D. Kim, "Large-scale synthesis of copper nanoparticles by chemically controlled reduction for applications of inkjet-printed electronics," *Nanotechnology*, vol. 19, no. 41, p. 415604, 2008.

[116] J. Liu and R. H. Hurt, "Ion release kinetics and particle persistence in aqueous nano-silver colloids," *Environmental science & technology*, vol. 44, no. 6, pp. 2169–2175, 2010.

[117] C. E. Albers, W. Hofstetter, K. A. Siebenrock, R. Landmann, and F. M. Klenke, "In vitro cytotoxicity of silver nanoparticles on osteoblasts and osteoclasts at antibacterial concentrations," *Nanotoxicology*, vol. 7, no. 1, pp. 30–36, 2013.

[118] Z. Wang, N. Li, J. Zhao, J. C. White, P. Qu, and B. Xing, "Cuo nanoparticle interaction with human epithelial cells: cellular uptake, location, export, and genotoxicity," *Chemical research in toxicology*, vol. 25, no. 7, pp. 1512–1521, 2012.

[119] R. J. Kavlock, G. P. Daston, C. DeRosa, P. Fenner-Crisp, L. E. Gray, S. Kaattari, G. Lucier, M. Luster, M. J. Mac, C. Maczka, *et al.*, "Research needs for the risk

assessment of health and environmental effects of endocrine disruptors: a report of the us epa-sponsored workshop.," *Environmental health perspectives*, vol. 104, no. Suppl 4, p. 715, 1996.

[120] W. Zhang, Y. Yao, N. Sullivan, and Y. Chen, "Modeling the primary size effects of citrate-coated silver nanoparticles on their ion release kinetics," *Environmental science & technology*, vol. 45, no. 10, pp. 4422–4428, 2011.

[121] O. V. Zakharova, A. Y. Godymchuk, A. A. Gusev, S. I. Gulchenko, I. A. Vasyukova, and D. V. Kuznetsov, "Considerable variation of antibacterial activity of cu nanoparticles suspensions depending on the storage time, dispersive medium, and particle sizes," *BioMed research international*, vol. 2015, 2015.

[122] J. R. Conway, A. S. Adeleye, J. Gardea-Torresdey, and A. A. Keller, "Aggregation, dissolution, and transformation of copper nanoparticles in natural waters," *Environmental science & technology*, vol. 49, no. 5, pp. 2749–2756, 2015.

[123] L. Li, M. L. Fernández-Cruz, M. Connolly, M. Schuster, and J. M. Navas, "Dissolution and aggregation of cu nanoparticles in culture media: effects of incubation temperature and particles size," *Journal of Nanoparticle Research*, vol. 17, no. 1, p. 38, 2015.

[124] L.-F. Wang, N. Habibul, D.-Q. He, W.-W. Li, X. Zhang, H. Jiang, and H.-Q. Yu, "Copper release from copper nanoparticles in the presence of natural organic matter," *Water research*, vol. 68, pp. 12–23, 2015.

[125] S. Kittler, C. Greulich, J. Diendorf, M. Koller, and M. Epple, "Toxicity of silver nanoparticles increases during storage because of slow dissolution under release of silver ions," *Chemistry of Materials*, vol. 22, no. 16, pp. 4548–4554, 2010.

[126] J. Fabrega, S. N. Luoma, C. R. Tyler, T. S. Galloway, and J. R. Lead, "Silver nanoparticles: behaviour and effects in the aquatic environment," *Environment international*, vol. 37, no. 2, pp. 517–531, 2011.

[127] M. Taner, N. Sayar, I. G. Yulug, and S. Suzer, "Synthesis, characterization and antibacterial investigation of silver–copper nanoalloys," *Journal of Materials Chemistry*, vol. 21, no. 35, pp. 13150–13154, 2011.

[128] H. Cao, X. Liu, F. Meng, and P. K. Chu, "Biological actions of silver nanoparticles embedded in titanium controlled by micro-galvanic effects," *Biomaterials*, vol. 32, no. 3, pp. 693–705, 2011.

[129] P. Vanysek, "Ionic conductivity and diffusion at infinite dilution," *CRC handbook of chemistry and physics*, vol. 83, 2000.

[130] K. Hu, M. Brust, and A. J. Bard, "Characterization and surface charge measurement of self-assembled cds nanoparticle films," *Chemistry of materials*, vol. 10, no. 4, pp. 1160–1165, 1998.

[131] K.-S. Moon, H. Dong, R. Maric, S. Pothukuchi, A. Hunt, Y. Li, and C. Wong, "Thermal behavior of silver nanoparticles for low-temperature interconnect applications," *Journal of Electronic Materials*, vol. 34, no. 2, pp. 168–175, 2005.

[132] S.-J. L. Kang, *Sintering: densification, grain growth and microstructure*. Butterworth-Heinemann, 2004.

[133] J. Glazer, "Metallurgy of low temperature pb-free solders for electronic assembly," *International Materials Reviews*, vol. 40, no. 2, pp. 65–93, 1995.

[134] T. Wang, X. Chen, G.-Q. Lu, and G.-Y. Lei, "Low-temperature sintering with nano-silver paste in die-attached interconnection," *journal of electronic materials*, vol. 36, no. 10, pp. 1333–1340, 2007.

[135] S. Gamerith, A. Klug, H. Scheiber, U. Scherf, E. Moderegger, and E. J. List, "Direct ink-jet printing of ag–cu nanoparticle and ag-precursor based electrodes for ofet applications," *Advanced Functional Materials*, vol. 17, no. 16, pp. 3111–3118, 2007.

[136] D. Frear, J. Jang, J. Lin, and C. Zhang, "Pb-free solders for flip-chip interconnects," *Jom*, vol. 53, no. 6, pp. 28–33, 2001.

[137] J. R. Greer and R. A. Street, "Thermal cure effects on electrical performance of nanoparticle silver inks," *Acta Materialia*, vol. 55, no. 18, pp. 6345–6349, 2007.

[138] R. K. Bordia and A. Jagota, "Crack growth and damage in constrained sintering films," *Journal of the American Ceramic Society*, vol. 76, no. 10, pp. 2475–2485, 1993.

[139] L. Freund and E. Chason, "Model for stress generated upon contact of neighboring islands on the surface of a substrate," *Journal of Applied Physics*, vol. 89, no. 9, pp. 4866–4873, 2001.

[140] W. Lee, R. Eadie, G. Weatherly, and K. Aust, "A study of the sintering of spherical silver powderii. the initial stage," *Acta Metallurgica*, vol. 26, no. 12, pp. 1837–1843, 1978.

[141] W. W. Kwan, V. Kripesh, M. K. Iyer, M. Gupta, A. Tay, and R. Tummala, "Low temperature sintering process for deposition of nano-structured metal for nano ic packaging," in *Electronics Packaging Technology, 2003 5th Conference (EPTC 2003)*, pp. 551–556, IEEE, 2003.

[142] S. Jang, Y. Seo, J. Choi, T. Kim, J. Cho, S. Kim, and D. Kim, "Sintering of inkjet printed copper nanoparticles for flexible electronics," *Scripta Materialia*, vol. 62, no. 5, pp. 258–261, 2010.

[143] B. Oregan and M. Grfitzeli, "A low-cost, high-efficiency solar cell based on dye-sensitized," *nature*, vol. 353, no. 6346, pp. 737–740, 1991.

[144] F. Thümmler and W. Thomma, "The sintering process," *Metallurgical Reviews*, vol. 12, no. 1, pp. 69–108, 1967.

[145] R. R. Arvizo, S. Bhattacharyya, R. A. Kudgus, K. Giri, R. Bhattacharya, and P. Mukherjee, "Intrinsic therapeutic applications of noble metal nanoparticles: past, present and future," *Chemical Society Reviews*, vol. 41, no. 7, pp. 2943–2970, 2012.

[146] D. Deng, Y. Jin, Y. Cheng, T. Qi, and F. Xiao, "Copper nanoparticles: aqueous phase synthesis and conductive films fabrication at low sintering temperature," *ACS applied materials & interfaces*, vol. 5, no. 9, pp. 3839–3846, 2013.

[147] I. Jung, K. Shin, N. R. Kim, and H. M. Lee, "Synthesis of low-temperature-processable and highly conductive ag ink by a simple ligand modification: the role of adsorption energy," *Journal of Materials Chemistry C*, vol. 1, no. 9, pp. 1855–1862, 2013.

[148] P. Pulkkinen, J. Shan, K. Leppanen, A. Kansakoski, A. Laiho, M. Jarn, and H. Tenhu, "Poly (ethylene imine) and tetraethylenepentamine as protecting agents for metallic copper nanoparticles," *ACS applied materials & interfaces*, vol. 1, no. 2, pp. 519–525, 2009.

[149] K. Ankireddy, S. Vunnam, J. Kellar, and W. Cross, "Highly conductive short chain carboxylic acid encapsulated silver nanoparticle based inks for direct write technology applications," *Journal of Materials Chemistry C*, vol. 1, no. 3, pp. 572–579, 2013.

[150] J. Li, J. Mayer, and E. Colgan, "Oxidation and protection in copper and copper alloy thin films," *Journal of applied physics*, vol. 70, no. 5, pp. 2820–2827, 1991.

[151] C. Lee, N. R. Kim, J. Koo, Y. J. Lee, and H. M. Lee, "Cu-ag core–shell nanoparticles with enhanced oxidation stability for printed electronics," *Nanotechnology*, vol. 26, no. 45, p. 455601, 2015.

[152] K.-S. Chou and Y.-S. Lai, "Effect of polyvinyl pyrrolidone molecular weights on the formation of nanosized silver colloids," *Materials Chemistry and Physics*, vol. 83, no. 1, pp. 82–88, 2004.

[153] B. J. Berne and R. Pecora, *Dynamic light scattering: with applications to chemistry, biology, and physics*. Courier Corporation, 2000.

[154] G. A. Wistreich, *Microbiology laboratory*. Prentice Hall, 2003.

[155] C. Scientific, "Instruction manual," *CS615 Water Content Reflectometer. Campbell Scientific, Logan, UT*, 1996.

[156] E. A. Atekwana, E. A. Atekwana, R. S. Rowe, D. D. Werkema, and F. D. Legall, "The relationship of total dissolved solids measurements to bulk electrical conductivity in an aquifer contaminated with hydrocarbon," *Journal of Applied Geophysics*, vol. 56, no. 4, pp. 281–294, 2004.

[157] F. Smits, "Measurement of sheet resistivities with the four-point probe," *Bell Labs Technical Journal*, vol. 37, no. 3, pp. 711–718, 1958.

[158] J. S. Kim, E. Kuk, K. N. Yu, J.-H. Kim, S. J. Park, H. J. Lee, S. H. Kim, Y. K. Park, Y. H. Park, C.-Y. Hwang, *et al.*, "Antimicrobial effects of silver nanoparticles," *Nanomedicine: Nanotechnology, Biology and Medicine*, vol. 3, no. 1, pp. 95–101, 2007.

[159] N. Savage and M. S. Diallo, "Nanomaterials and water purification: opportunities and challenges," *Journal of Nanoparticle research*, vol. 7, no. 4, pp. 331–342, 2005.

[160] J. Farkas, H. Peter, P. Christian, J. A. G. Urrea, M. Hassellöv, J. Tuoriniemi, S. Gustafsson, E. Olsson, K. Hylland, and K. V. Thomas, "Characterization of the effluent from a nanosilver producing washing machine," *Environment International*, vol. 37, no. 6, pp. 1057–1062, 2011.

[161] C. D. Salgado, K. A. Sepkowitz, J. F. John, J. R. Cantey, H. H. Attaway, K. D. Freeman, P. A. Sharpe, H. T. Michels, and M. G. Schmidt, "Copper surfaces reduce the rate of healthcare-acquired infections in the intensive care unit," *Infection Control & Hospital Epidemiology*, vol. 34, no. 05, pp. 479–486, 2013.

[162] D. Manikandan, S. Mohan, and K. Nair, "Annealing-induced metallic core–shell clusterization in soda-lime glass: an optical absorption studyexperiment and theory," *Physica B: Condensed Matter*, vol. 337, no. 1, pp. 64–68, 2003.

[163] T. Anderson, R. Magruder Iii, J. Wittig, D. Kinser, and R. Zuhr, "Fabrication of cu-coated ag nanocrystals in silica by sequential ion implantation," *Nuclear Instruments and Methods in Physics Research Section B: Beam Interactions with Materials and Atoms*, vol. 171, no. 3, pp. 401–405, 2000.

[164] T. X. Phuoc and M. K. Chyu, "Synthesis and characterization of nanocomposites using the nanoscale laser soldering in liquid technique," *Journal of Nanoscience and Nanotechnology*, vol. 1, p. 101, 2013.

[165] Y. Kim, R. C. Johnson, J. Li, J. T. Hupp, and G. C. Schatz, "Synthesis, linear extinction, and preliminary resonant hyper-rayleigh scattering studies of gold-core/silver-shell nanoparticles: comparisons of theory and experiment," *Chemical physics letters*, vol. 352, no. 5, pp. 421–428, 2002.

[166] M. Miyakawa, N. Hiyoshi, M. Nishioka, H. Koda, K. Sato, A. Miyazawa, and T. M. Suzuki, "Continuous syntheses of pd@ pt and cu@ ag core–shell nanoparticles using microwave-assisted core particle formation coupled with galvanic metal displacement," *Nanoscale*, vol. 6, no. 15, pp. 8720–8725, 2014.

[167] J. A. Gerbec, D. Magana, A. Washington, and G. F. Strouse, "Microwave-enhanced reaction rates for nanoparticle synthesis," *Journal of the American Chemical Society*, vol. 127, no. 45, pp. 15791–15800, 2005.

[168] A. M. R. Galletti, C. Antonetti, M. Marracci, F. Piccinelli, and B. Tellini, "Novel microwave-synthesis of cu nanoparticles in the absence of any stabilizing agent and their antibacterial and antistatic applications," *Applied Surface Science*, vol. 280, pp. 610–618, 2013.

[169] S. Berciaud, L. Cognet, P. Tamarat, and B. Lounis, "Observation of intrinsic size effects in the optical response of individual gold nanoparticles," *Nano letters*, vol. 5, no. 3, pp. 515–518, 2005.

[170] K. L. Kelly, E. Coronado, L. L. Zhao, G. C. Schatz, *et al.*, "The optical properties of metal nanoparticles: the influence of size, shape, and dielectric environment," *Journal of Physical Chemistry B-Condensed Phase*, vol. 107, no. 3, pp. 668–677, 2003.

[171] M. E. Samberg, E. G. Loboa, S. J. Oldenburg, and N. A. Monteiro-Riviere, "Silver nanoparticles do not influence stem cell differentiation but cause minimal toxicity," *Nanomedicine*, vol. 7, no. 8, pp. 1197–1209, 2012.

[172] N. Motl, A. Smith, C. DeSantis, and S. Skrabalak, "Engineering plasmonic metal colloids through composition and structural design," *Chemical Society Reviews*, vol. 43, no. 11, pp. 3823–3834, 2014.

[173] E. Prodan and P. Nordlander, "Plasmon hybridization in spherical nanoparticles," *The Journal of chemical physics*, vol. 120, no. 11, pp. 5444–5454, 2004.

[174] J. Manson, D. Kumar, B. J. Meenan, and D. Dixon, "Polyethylene glycol functionalized gold nanoparticles: the influence of capping density on stability in various media," *Gold bulletin*, vol. 44, no. 2, pp. 99–105, 2011.

[175] H. Freiser, *Ion-selective electrodes in analytical chemistry*. Springer Science & Business Media, 2012.

[176] K. Bunzl, W. Schmidt, and B. Sansoni, "Kinetics of ion exchange in soil organic matter. iv. adsorption and desorption of pb2+, cu2+, cd2+, zn2+ and ca2+ by peat," *Journal of Soil Science*, vol. 27, no. 1, pp. 32–41, 1976.

[177] V. K. Sharma, K. M. Siskova, R. Zboril, and J. L. Gardea-Torresdey, "Organic-coated silver nanoparticles in biological and environmental conditions: fate, stability and toxicity," *Advances in colloid and interface science*, vol. 204, pp. 15–34, 2014.

[178] Y.-J. Lee, J. Kim, J. Oh, S. Bae, S. Lee, I. S. Hong, and S.-H. Kim, "Ion-release kinetics and ecotoxicity effects of silver nanoparticles," *Environmental toxicology and chemistry*, vol. 31, no. 1, pp. 155–159, 2012.

[179] A. Hahn, G. Brandes, P. Wagener, and S. Barcikowski, "Metal ion release kinetics from nanoparticle silicone composites," *Journal of controlled release*, vol. 154, no. 2, pp. 164–170, 2011.

[180] W. Stumm, J. J. Morgan, and J. I. Drever, "Aquatic chemistry," *Journal of Environmental Quality*, vol. 25, no. 5, p. 1162, 1996.

[181] L. Song, M. Connolly, M. L. Fernández-Cruz, M. G. Vijver, M. Fernández, E. Conde, G. R. de Snoo, W. J. Peijnenburg, and J. M. Navas, "Species-specific toxicity of copper nanoparticles among mammalian and piscine cell lines," *Nanotoxicology*, vol. 8, no. 4, pp. 383–393, 2014.

[182] L. Zhang, Y. Jiang, Y. Ding, M. Povey, and D. York, "Investigation into the antibacterial behaviour of suspensions of zno nanoparticles (zno nanofluids)," *Journal of Nanoparticle Research*, vol. 9, no. 3, pp. 479–489, 2007.

[183] A. Henglein, "Colloidal silver nanoparticles: photochemical preparation and interaction with o2, ccl4, and some metal ions," *Chemistry of Materials*, vol. 10, no. 1, pp. 444–450, 1998.

[184] A. W. Bauer, D. M. PERRY, and W. M. KIRBY, "Single-disk antibiotic-sensitivity testing of staphylococci: An analysis of technique and results," *AMA archives of internal medicine*, vol. 104, no. 2, pp. 208–216, 1959.

[185] A. R. Shahverdi, A. Fakhimi, H. R. Shahverdi, and S. Minaian, "Synthesis and effect of silver nanoparticles on the antibacterial activity of different antibiotics against staphylococcus aureus and escherichia coli," *Nanomedicine: Nanotechnology, Biology and Medicine*, vol. 3, no. 2, pp. 168–171, 2007.

[186] P. Pourali, B. Yahyaei, H. Ajoudanifar, R. Taheri, H. Alavi, and A. Hoseini, "Impregnation of the bacterial cellulose membrane with biologically produced silver nanoparticles," *Current microbiology*, vol. 69, no. 6, pp. 785–793, 2014.

[187] C. Baker, A. Pradhan, L. Pakstis, D. J. Pochan, and S. I. Shah, "Synthesis and antibacterial properties of silver nanoparticles," *Journal of nanoscience and nanotechnology*, vol. 5, no. 2, pp. 244–249, 2005.

[188] K. Hirota, M. Sugimoto, M. Kato, K. Tsukagoshi, T. Tanigawa, and H. Sugimoto, "Preparation of zinc oxide ceramics with a sustainable antibacterial activity under dark conditions," *Ceramics International*, vol. 36, no. 2, pp. 497–506, 2010.

[189] C. Furnas, "Grading aggregates: I," *Ind. Eng. Chem*, vol. 23, no. 9, pp. 1052–58, 1931.

[190] S. J. Kim, E. A. Stach, and C. A. Handwerker, "Fabrication of conductive interconnects by ag migration in cu–ag core-shell nanoparticles," *Applied Physics Letters*, vol. 96, no. 14, p. 144101, 2010.